

The origin of preferential flow and non-equilibrium transport in unsaturated heterogeneous porous systems

Baviskar, Shirishkumar

DOI

[10.4233/uuid:faedef77-b7dc-47c7-a6d5-891e95baab70](https://doi.org/10.4233/uuid:faedef77-b7dc-47c7-a6d5-891e95baab70)

Publication date

2016

Document Version

Final published version

Citation (APA)

Baviskar, S. (2016). *The origin of preferential flow and non-equilibrium transport in unsaturated heterogeneous porous systems*. [Dissertation (TU Delft), Delft University of Technology].
<https://doi.org/10.4233/uuid:faedef77-b7dc-47c7-a6d5-891e95baab70>

Important note

To cite this publication, please use the final published version (if applicable).
Please check the document version above.

Copyright

Other than for strictly personal use, it is not permitted to download, forward or distribute the text or part of it, without the consent of the author(s) and/or copyright holder(s), unless the work is under an open content license such as Creative Commons.

Takedown policy

Please contact us and provide details if you believe this document breaches copyrights.
We will remove access to the work immediately and investigate your claim.

The origin of preferential flow and non-equilibrium
transport in unsaturated heterogeneous porous
systems

The origin of preferential flow and non-equilibrium transport in unsaturated heterogeneous porous systems

Proefschrift

ter verkrijging van de graad van doctor

aan de Technische Universiteit Delft,

op gezag van de Rector Magnificus prof. ir. K. C. A. M. Luyben;

voorzitter van het College voor Promoties,

in het openbaar te verdedigen op donderdag 8 december om 12.30 uur

door

Shirishkumar Madhukar BAVISKAR

Master of Technology in Environmental Engineering,

Indian Institute of Technology Guwahati, India.

geboren te Nasik, India

This dissertation has been approved by the
promotor: Prof. dr. ir. T. J. Heimovaara

Composition of the doctoral committee:

Rector Magnificus	chairman
Prof.dr. ir. T. J. Heimovaara	Delft University of Technology

Independent members:

Prof. dr. H. Bruining	Delft University of Technology
Prof. dr. C. Jommi	Delft University of Technology
Prof. dr. ir. M. Bakker	Delft University of Technology
Prof. dr. J. McDougall	Napier Univeristy, Edingburgh, Scotland, UK

This research was funded by the Eur-India, Lot-13 PhD scholarship program by
Eurasmus Mundus and partly by the Delft University of Technology.



Printed by: Ipskamp Printing

Publisher: TU Delft Library

Cover by: Shirishkumar Madhukar BAVISKAR

Copyright ©2016 by Shirishkumar Madhukar BAVISKAR

Email: s.m.baviskar85@gmail.com

ISBN: 978-94-6186-758-2

An electronic version of this dissertation is available at

<http://repository.tudelft.nl/>.

All rights reserved. No parts of this publication may be reproduced, stored in a retrieval system, or transmitted, in any form by any means, electronic, mechanical, photocopying, recording, or otherwise, without the prior written permission of author.

Dedicated to my parents

Contents

1	Introduction	1
1.1	Current state of waste management: Landfilling	1
1.2	Emission potential and aftercare of MSW landfill	2
1.3	Preferential flow in MSW landfill	4
1.4	Measurement of soil water retention properties	6
1.5	Aims and objectives	7
1.6	Outline of the Thesis	8
2	Numerical modelling of unsaturated flow and solute transport in waste bodies with steep concentration gradients	11
2.1	Introduction	12
2.2	Theory	15
2.2.1	Water Flow	15
2.2.2	Solute Transport	17
2.3	Materials and Methods	20
2.3.1	Numerical implementations	20
2.3.2	Evaluation Criteria	24
2.4	Results and Discussion	25
2.4.1	Numerical Scenario 1 - Drainage Problems	25
2.4.2	Numerical Scenario 2 - Application Problem 1	32
2.4.3	Numerical Scenario 3 - Application Problem 2	40
2.5	Conclusions	43
3	Numerical study investigating origin of preferential flow and controlling factors of non-equilibrium in transport for small scale systems	45
3.1	Introduction	46
3.2	Theory	48
3.2.1	Water Flow	48
3.2.2	Solute Transport	51

3.3	Materials and Methods	53
3.3.1	VarSatFT simulator	53
3.3.2	Description of small scale systems	53
3.4	Results and Discussion	54
3.4.1	Distributions of flow and transport observed in spatial distributions	59
3.4.2	Average total drainage relationships	65
3.4.2.1	Effect of heterogeneity on flow and transport	65
3.4.2.2	Effect of infiltration pattern on flow and transport	65
3.4.2.3	Effect of infiltration rates on flow and transport	68
3.4.2.4	Factors controlling emission potential	68
3.4.3	Feasibility of single continuum modelling method for MSW landfill	71
3.4.4	Suitable modelling methods for MSW landfill	71
3.5	Conclusions	72
4	Controlling factors of non-equilibrium in transport: Lab scale experiments with numerical simulations	75
4.1	Introduction	76
4.2	Materials and Methods	77
4.2.1	Lab setup of 2D sand frame	77
4.2.1.1	Correction for lab scale measurement	79
4.2.2	Material properties for numerical simulations	82
4.3	Results and Discussion	85
4.3.1	EC calibration for lab scale experiments	85
4.3.2	Lab scale experiments: flow and transport in 2D sand frame	85
4.3.2.1	Effect of heterogeneity	85
4.3.2.2	Effect of infiltration pattern and infiltration rates	89
4.3.3	Numerical simulations for lab scale experiments	90
4.4	Conclusions	93
5	Quantification of soil water retention parameters using multi-section TDR-waveform analysis	97
5.1	Introduction	98
5.2	Theory	99
5.3	Methods and Materials	103
5.3.1	Modelling the TDR wave form	103
5.3.2	Parameter estimation by DREAM _{ZS}	103
5.3.3	Experiment	104
5.3.3.1	Setup	104
5.3.3.2	Calibration of the parameters in the MSSF-TDR method	105

5.3.3.3	Multi-step drainage experiment	109
5.3.4	Numerical modelling of the multi-step drainage experiment . . .	109
5.4	Results and Discussion	110
5.4.1	Calibration Step1: The input waveform	110
5.4.2	Calibration Step2: Complete TDR system using Air and Water waveforms	111
5.4.3	Multi-step drainage experiment	111
5.4.4	Model validation of multi-step drainage experiment.	119
5.5	Conclusions	122
6	Conclusions	123
6.1	Overall summary and conclusions	123
AppendixA		127
A.1	FEM discretization of water transport model	127
A.1.1	Solution technique for water transport model	130
A.1.2	Time discretization for water transport model	133
A.2	FEM discretization of solute transport model	137
A.2.1	Solution technique for solute transport model	139
A.2.2	Time discretization for solute transport model	141
AppendixB		145
B.1	Finite difference approximation of Water Flow	145
B.1.1	Surface ponding	147
B.2	Eulerian-Lagrangian formulation for Solute Transport	148
AppendixC		153
C.1	DREAM _{ZS} algorithm settings	153
AppendixD		155
D.1	Multi-Section Scatter Function Model	155
D.2	Characteristic Impedance	155
D.3	DREAM _{ZS} algorithm settings	158
Bibliography		159
Summary		175
Samenvatting		179
Acknowledgments		183

Curriculum Vitae	185
List of Publications	187

Chapter 1

Introduction

1.1 Current state of waste management: Landfilling

Currently about 2 billion tonnes of municipal solid waste (MSW) and 7 to 10 billion tonnes of urban waste are being produced yearly (Wilson et al. 2015a). Due to the expected economic growth of developing countries the amount of waste produced is expected to double by 2025 (Hoornweg and Bhada-Tata 2012; Stromberg 2013). The environmental stress due to MSW will therefore increase (See Table 1.1).

Developing countries face an enormous challenge to improve the waste management. Currently the average waste collection coverage is about 50% (Wilson et al. 2015b) and most of the waste is dumped in an uncontrolled fashion (Hoornweg and Bhada-Tata 2012; Kaushal 2012 and data in Table 1.1). The first priority these countries face, is to increase the waste collection coverage and stop the uncontrolled dumping of waste in favour other controlled options of waste management. Moving to the ultimate waste management goal of a circular economy is currently far too costly for the developing countries and therefore not a realistic option (Ali et al. 2005). As space is not a scarce commodity, many of the developing countries choose to landfill MSW in engineered sanitary landfills over other alternatives (Ayub and Khan 2011; Lincoln 2011; Neto et al. 2011; Robinson et al. 2011).

A decreasing trend in landfilling is observed for most of the developed nations (EC 2010), mainly because of a reduction in waste production but also because of the development of methods to reuse, recycle and incinerate MSW (EEA 2009; EC 2010; IGEL 2014). This has reduced emissions to the environment (Bendz et al. 1998; Baba et al. 2004; Barlaz et al. 2010; Bareither et al. 2010; Watson 2013; OECD UTC(GMT)). However, the relatively low cost of landfilling in comparison with alternative approaches,

Table 1.1: MSW data for selected countries. Data extracted on 10/11/2015, 18.03 UTC (GMT) from atlas.d-waste.

Countries	China	India	Netherlands	South Africa	UK	USA
MSW generation [$t/year$]	300×10^6	226×10^6	8.8×10^6	12.9×10^6	30.4×10^6	228.6×10^6
Environmental stress (MSW) [t/km^2]	32.2	76.2	261.5	10.6	126.0	25.0
Generation per capita [$kg/year$]	229.4	182.5	526.0	255.5	482.0	733.7
Collection coverage [%]	49.3	51.1	100	96	100	95
Recycling rate [%]	-	-	24	-	28.0	23.8

causes landfilling to remain the preferred waste management option also for many developed countries, especially those where space is not a scarce commodity (Hoornweg and Bhada-Tata, 2012).

All landfills and waste dumps, the old ones already closed, the ones currently in use and the future ones still to be developed, form a legacy for future generations which needs to be managed in order to protect human health and the environment from potential (toxic) emissions from the waste bodies. The current Dutch legislation requires eternal after care of landfills (Netherlands 2016) whereas the European Landfill Directive requires member states to have provisions for landfill aftercare for a period of at least 30 years (EC 1999). Because more and more countries are realizing that the current approaches to long-term after-care of landfills is not really sustainable and becoming more and more a costly challenge it has become an topic of research (Barlaz et al. 2002; Heimovaara et al. 2007; Scharff 2007; Woelders et al. 2007).

1.2 Emission potential and aftercare of MSW landfill

Concentration of waste materials in landfills poses a threat to the environment because the potential emission of toxic compounds. The emission potential of a MSW landfill can be defined as the fraction of pollutants present inside a waste body that eventually can emit to

the environment during the life time of the landfill (Bun et al. 2013). Landfill stabilization aims to reduce the emission potential by degrading pollutants to non-toxic compounds, by reducing the mobility of the pollutants by changing the chemical speciation and by methods aiming to reduce emissions by influencing the transport water and gas through the waste body (Heimovaara et al. 2007, 2010; Heimovaara 2011). In the Netherlands the regulations require the installation of watertight cover liners in order to prevent the infiltration of water and the simultaneous extraction of landfill gas. However, treating landfills as a large scale bioreactor by irrigation of water and subsequent recirculation of leachate possibly combined with aeration leads to an enhanced biological degradation of organic compounds. The consequence is a significant reduction in emission potential of nearly all pollutants (Pohland and Alyousfi 1994; Augenstein et al. 1998; Reinhart and AlYousfi 1996; Benson et al. 2007; Calabro et al. 2010; Schiappacasse et al. 2010). Increasing water content by irrigation and recirculation of leachate stimulates the hydrolysis of solid waste, increasing biodegradation rates of organic matter (See Figure 1.1). The stabilized organic material has a larger absorption capacity for inorganic contaminants (Reinhart 1996; El-Fadel 1999; Erses and Onay 2003; Sanphoti et al. 2006; Jiang et al. 2008; Zhu et al. 2009). Aeration of the waste body stimulates aerobic biodegradation of the waste (Agdag and Sponza 2004; Prantl et al. 2005; Ritzkowski et al. 2007). The current developments in landfill aftercare are based on the active stimulation of anaerobic and aerobic biodegradation in waste bodies during a relatively short period after closure of the landfill which leads to a significant reduction in emission potential which therefore leads to stabilized waste bodies which require much less aftercare (Barlaz et al. 2002; Inoue et al. 2005; Heimovaara et al. 2007; Rich et al. 2008; See Figure 1.2).

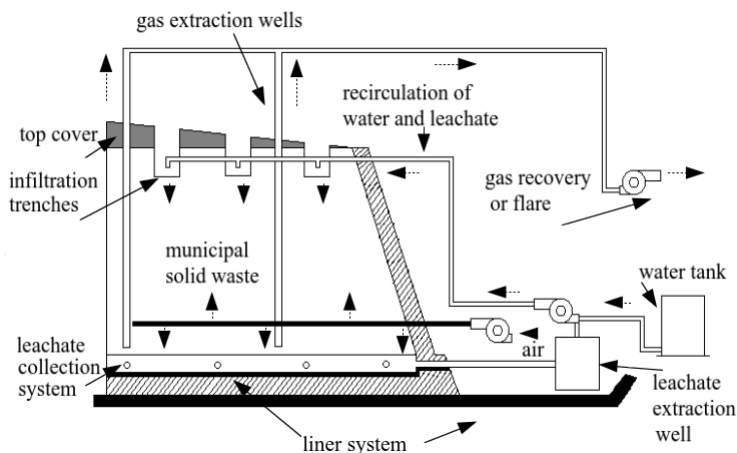


Figure 1.1: Conceptual landfill bioreactor.

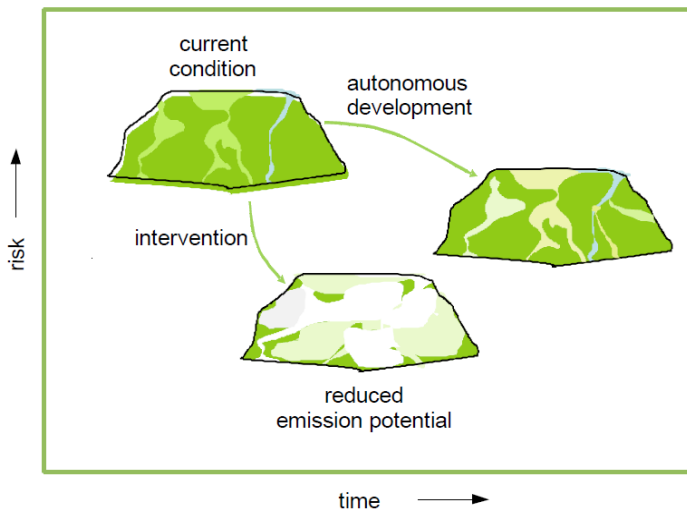


Figure 1.2: Conceptual model for reducing emission potential of a landfill (Figure from Heimovaara et al. (2010)).

In order for the regulators and landfill operators to agree on a required level of after care, a quantitative estimation of remaining long-term emission potential is required. Many projects have been carried out claiming effectiveness of landfill stabilization technology (Pohland and Alyousfi 1994; Davis-Hoover et al. 2001; Agdag and Sponza 2004; Borglin et al. 2004; Demir et al. 2004; Heyer et al. 2005; Al-Ghazawi and Abdulla 2008; Cho E. et al. 2009; Han and Kim 2010) as a method to stimulate landfill gas production, however no projects up to date have attempted to reduce emissions with the leachate. Currently three landfill stabilization demonstration projects are in preparation in Netherlands. These projects has led to a research program aimed towards quantifying the long-term emission potential of landfills (Heimovaara et al. 2010; Kattenberg and Heimovaara 2011; Scharff 2014).

1.3 Preferential flow in MSW landfill

MSW landfill waste bodies are very heterogeneous, unsaturated porous media (Rosqvist et al. 2005b; Kindlein et al. 2006). Figure 1.3(a) shows a picture of the face of the waste body in the Landgraaf bioreactor photographed during the excavation of the test cell and is a good illustration of this heterogeneity. The conceptual idea of the waste body is illustrated in Figure 1.3(b). Field measurements show a large spatial variation of water content inside waste bodies, ranging from fully saturated conditions to complete dry-

ness (Blight et al. 1992; Sormunen et al. 2008a,b) caused by varying hydraulic properties ranging from highly water absorbent to water repellent and from impermeable to readily permeable (Powrie and Beaven 1999; Kazimoglu et al. 2006). The presence of impermeable plastic bags, gas wells, daily cover layers, areas of low and high compaction lead to stratification in landfills (Fellner et al. 2009). As a result, the permeability in horizontal direction is larger than in vertical direction. Consequently, rainfall infiltration leads to local ponding within the waste body, leading to horizontal flow (Baviskar and Heimovaara 2014). The existing vertical channels and fissures resulting from uneven landfill settlements (Bareither et al. 2010) are connected by horizontal flow forming a complex flow pattern consisting of a network of preferential pathways (Rosqvist et al. 2005b).

Preferential flow in landfill leads to rapid movement of water through a small fraction of the pore space by passing most of the volume of the bulk waste matrix (Guyonnet et al. 1998; Mikac et al. 1998; Oman and Rosqvist 1999; Rosqvist and Destouni 2000; Rosqvist et al. 2005b; Lu and Luan 2009; Fellner and Brunner 2010) (See Figure 1.3). Preferential flow has a large impact on solute transport. Preferential flow paths are flushed by clean rain water, leading to development of solute concentration gradients in the waste body between water present in the stagnant bulk and the flow paths. These gradients cause slow diffusion from the bulk to the mobile water (Skopp 1981; Jarvis 1998; Rosqvist et al. 2005b). The slow diffusion induces non-equilibrium solute transport in the waste body which has a major impact on the microbial degradation of organic matter in the landfill. A number of papers in the literature have focused on the quantification of preferential flow in landfills and the impact of the flow on the solute transport (Blight et al. 1992; El-Fadel et al. 1997a; Rosqvist and Destouni 2000; Rosqvist et al. 2005b; Fellner et al. 2009; Fellner and Brunner 2010). Little information is available on the impact of preferential flow on microbial degradation. Water plays a vital role in biochemical metabolism and also acts as a transport route for the substrates and micro-organisms.

Mathematical models have been used in past for studying leachate quantity and quality (El-Fadel et al. 1997a). The models can be broadly classified into two major categories, continuum based models and upscaled models. In continuum based models, the modelling approach of flow and transport in the landfills has assumed that waste is homogeneous (McDougall 2007; Gholamifard et al. 2008) so averaged values for waste properties can be used in these continuum models. However, comparison of model results with measured discharges of solutes show that in many cases predictions from such continuum models are not in agreement with field observations (Ugoccioni and Zeiss 1997; Rosqvist and Destouni 2000; Rosqvist et al. 2005b). It is hypothesized that continuum based models do not take the preferential pathways and the resulting non-equilibrium in transport in landfills into account. Better results are obtained with models using a transfer function approach (Rosqvist and Destouni 2000; Rosqvist et al. 2005b; Jury and Stolzy

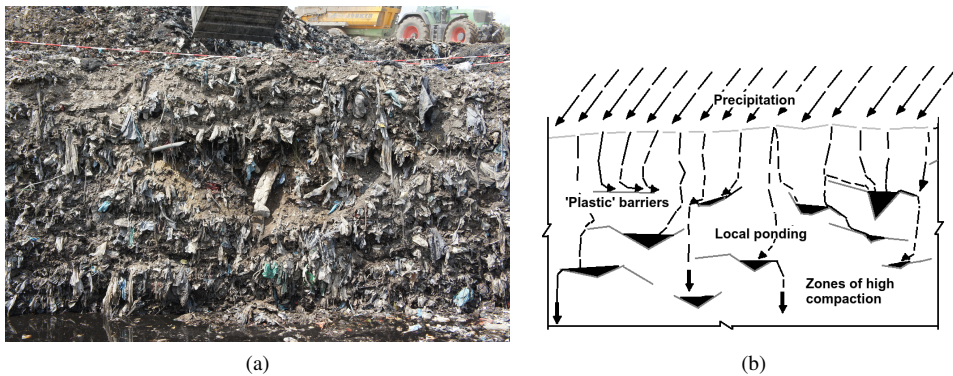


Figure 1.3: Sectional view showing heterogeneous nature of excavated pilot scale landfill located at Landgraaf, Netherlands (a) and simplified overview of flow inside a landfill (Figures from Baviskar and Heimovaara (2011))(b).

1982; Jury 1982; Zacharof and Butler 2004b,a), dual porosity, dual permeability concepts (Bendz et al. 1998; Šimunek et al. 2003) or stream tubes models (Matanga 1996). In these concepts, non-equilibrium transport is empirically taken into account and as a result model results can describe field observations. However the origin of preferential flow and the controlling factors of non-equilibrium in solute transport in waste bodies is still not very well understood.

1.4 Measurement of soil water retention properties

In order to simulate unsaturated water flow with the Richards' equation it is essential to have quantitative information of the soil water retention properties of the porous medium which is being investigated. The soil water retention curve is used to relate the volumetric water content and the soil water potential (Buckingham 1907). In addition the volumetric water content is an important parameter for calculating the relative hydraulic conductivity of unsaturated soils (Mualem 1976; van Genuchten 1980). The water retention properties of porous materials can be determined using pressure plates (Betteli and Flury 2009; Solone et al. 2012), tensiometers (Lourenco et al. 2007; HYPROP-S UMS), tension disk infiltrometers (Šimunek 1999), cone permeameters (Gribb 1996; Homma et al. 2004), and techniques like evaporation methods (Šimunek et al. 1998) or multi-step outflow (Peters and Durner 2006) methods.

Most of these classic approaches consider average water content along the height of the sample. This leads to an error in the estimation of the unsaturated parameters which increases when length of sample increases (Betteli and Flury 2009; Solone et al. 2012). There is also an error in parameter estimation when measurements are performed close

to air entry, making measurements under wet conditions problematic (Peters and Durner 2006). Recent advances in interpreting Time Domain Reflectometry (TDR) wave forms have led to approaches which enable the estimation of the distribution of the water content along the probe (Heimovaara et al. 2004; Laloy et al. 2014).

We developed a method for determining the water retention parameters of well sorted granular porous materials near saturation. In this approach, a multi-step drainage experiment is performed where cumulative discharge is measured and TDR measurements are carried out on a vertically installed TDR probe. Inverse modelling of TDR measurements under hydrostatic conditions with the method of Heimovaara et al. 2004 is used to obtain the van Genuchten parameters of the water retention curve (van Genuchten 1980; Ledieu et al. 1986).

1.5 Aims and objectives

The primary aim of this thesis is to investigate the origin of preferential flow and determine the controlling factors affecting non-equilibrium in transport, using numerical analysis and lab scale experiments for small scale systems. The hypothesis is that, material heterogeneity combined with dynamical boundary conditions is the origin of preferential flow controlling the solute transport in waste bodies. In order to investigate this hypothesis, a flow and transport simulator is required which can present steep concentration gradients. Three different implementations of such a simulator were developed and compared with each other. All three implementations are based on simulating unsaturated flow of water with the Richards' equation and the Mualem-van Genuchten approach for water retention and relative permeability. Solute transport is simulated with the Advection Dispersion Equation (ADE).

The unsaturated water flow and solute transport problem was implemented in a the commercial available COMSOL multi-physics simulator using the available model interfaces. In addition two other implementations were made in MATLAB, one based on finite elements with the open source package FAESOR and on based on finite differences and a Lagrangian particle method which we named Variably Saturated Flow and Transport (VarSatFT). Numerical simulations performed with the three different implementations are compared with measurements obtained from a series of simple laboratory experiments.

The objectives of the research are as follows:

- to develop simulator which can handle steep concentration gradients in porous systems preferably as an open source toolbox;
- to run different numerical scenarios with the different simulators to compare them

with each other and to understand the origin of preferential flow;

- to perform a lab scale study in order to investigate controlling factors affecting non-equilibrium in transport and compare the results with numerical simulations;

A secondary aim of the research was to develop a methodology for accurate measurement of the parameters in the water retention curve of well sorted granular materials near saturation. The available techniques in our laboratory gave results with a large uncertainty. The objective for this research was to develop an multi-step drainage experiment where the water content along a vertically installed TDR-probe is used to inversely modelled in order to obtain the parameters in the water retention curve.

1.6 Outline of the Thesis

This thesis consists of 6 Chapters

1. Chapter 2 - *"Numerical modelling of unsaturated flow and solute transport in waste bodies with steep concentration gradients"*. In this chapter three different numerical approximation methods are compared for modelling flow and transport in two dimensional porous media. The performance criteria used for comparison was mass-balance, the capacity to cope with steep gradients, time required for running the simulations and ease of implementation. This chapter helps to choose the simulator for research applications described in following chapters.
2. Chapter 3 - *"Numerical study investigating origin of preferential flow and controlling factors of non-equilibrium in transport for small scale systems"*. In this chapter a two dimensional coupled flow and transport model is used to investigate origin of preferential flow and controlling factors of non-equilibrium in transport. Numerical scenarios consisting of different spatial heterogeneities applied with different infiltration patterns and rates of inflow are performed. This chapter discusses, how infiltration patterns and rates can be utilized to reduce emission potential for full scale landfill. It also suggest suitable models to be used for a full scale landfill to determine its emission potential. It also discusses the feasibility of single continuum modelling method for full scale landfill.
3. Chapter 4 - *"Controlling factors of non-equilibrium in transport: Lab scale experiments with numerical simulations"*. This chapter discusses the lab scale experiments conducted to determine the factors responsible for non-equilibrium in an unsaturated two-dimensional setup. Numerical simulations of some lab scale scenarios were also carried out. The findings from the experiments and the numerical solutions helps to understand the non-equilibrium in transport taking place inside

the sand frame that could be similar to that occurring inside full scale waste bodies. The chapter helps to understand how heterogeneity, inflow rates and patterns affect the non-equilibrium in transport.

4. Chapter 5 - "*Quantification of soil water retention parameters using multi-section TDR-waveform analysis*". In this chapter the unsaturated properties of a sample are determined by analysing different TDR waveforms obtained at hydrostatic conditions subjected to the sample. Vertical distribution of water content along the TDR probe is considered by using unsaturated parametric relation. By reverse modelling of TDR waveforms and the cumulative discharge obtained during the multi-step drainage experiment, unsaturated water retention parameters are optimized. This approach can be used for longer height samples and samples which have uniform particle size distribution. The unsaturated water retention parameters obtained by this approach are verified by those obtained by evaporation method. The multi-step drainage discharge outflow is validated using numerical simulation of flow model.
5. Chapter 6 - "*Conclusions*". This chapter contains a brief conclusions of the thesis.

Note from the author

The chapters of this thesis are stand-alone journal publications and therefore can be read separately. Hence, some explanations and paragraphs may appear more than once.

Chapter 2

Numerical modelling of unsaturated flow and solute transport in waste bodies with steep concentration gradients

Abstract

Leachate from municipal solid waste landfills can be a significant contributor to ground-water pollution. Understanding the long term behaviour of leachate is therefore of crucial importance for the optimal management of landfills, especially when considering options to stabilize the waste body to reduce long term after care efforts. Numerical simulators are commonly used to interpret leachate dynamics inside waste bodies. This study provides a comparison of implementation of flow and solute transport for waste bodies in three simulators, namely (1) COMSOL (tm), a commercial multi-physics package (2) FAESOR, an open-source finite element toolbox implemented in MATLAB and (3) VarSatFT, our own finite difference implementation in MATLAB. Unsaturated water flow is described with Richards' equation and transport of a non sorbing, single component solute with the advection dispersion equation. The three implementations differ from each other in several aspects. In the built-in COMSOL implementations, no specific efforts were made to cope with the non-linearity due to the soil retention curve and relative permeability functions, the other two implemented a Picard iteration to cope with this non-linearity.

For solute transport, both the COMSOL and the FAESOR implementation used a relative straightforward upstream solution of the advection dispersion equation. The VarSatFT implementation implements a variant of the Lagrangian Marker-in-Cell method to handle sharp gradients in order to reduce the impact of numerical diffusion. The results from the different implementations are compared for different scenarios in small scale porous systems with different levels of heterogeneity and under varying flow regimes. As waste bodies are highly complex heterogeneous porous media with a large variation in saturation, steep concentration gradients tend to develop in the system. Therefore, accurate mass balances and minimum of numerical dispersion are important criteria for selecting an simulator to investigate flow and transport through waste. The results for the numerical scenario shows that VarSatFT simulator meets the criteria which can serve the purpose of interpreting accurate steep concentration gradients studying leachate dynamics involved in waste bodies.

Keywords: coupled modelling in porous media; finite element method; finite difference method; Eulerian-Lagrangian method

2.1 Introduction

Contamination of groundwater through leachate is potentially a major emission pathway from landfills (Koerner and Soong 2000; Barlaz et al. 2002; Kjeldsen et al. 2002; Baba et al. 2004; Yenigula et al. 2004; van Zomeren et al. 2006; Butt et al. 2008). Modern sanitary landfills in the Netherlands are built with a bottom liner which is above groundwater level and are equipped with controlled drainage systems (Heimovaara et al. 2010). Consequently, waste bodies are unsaturated porous media which given the nature of waste are highly heterogeneous in physical and chemical properties (Sormunen et al. 2008a; Ziyang et al. 2009; Baviskar and Heimovaara 2011). In order to understand the long-term development of leachate quality and possible options to reduce the potential for emissions via leachate, detailed understanding of water flow and solute transport dynamics is necessary (El-Fadel et al. 1997a,b; McDougall 2007; Gholamifard et al. 2008; Fellner and Brunner 2010).

The water flow in variably saturated porous media is commonly described using the Richards' equation (RE) (Richards 1931). Celia et al. (1990a) presented a method using Picard iteration to reduce mass balance errors occurring due to the extreme non-linearity in the soil retention and relative permeability properties at the cost of an increased simulation time.

Solute transport is described with the well known advection dispersion equation (ADE) (Fetter 1993; Bear 1988). There are several well known issues related to the numerical implementation of the ADE such as spurious oscillations for finite difference or finite element implementations with variable time steps (Radu et al. 2011) and the numerical dispersion is a serious draw back, especially when sharp gradients need to be considered (Gerya and Yuen 2003; Radu et al. 2011; Al-Lawatia 2012). Several solutions to these problems have been proposed, such as random walk methods (LaBolle and Zhang 2006), particle tracking methods (Aref 1983; Celia et al. 1990b; Srivastava and Yeh 1991; Sun 1999; Young et al. 2000; Younes and Ackerer 2005; Zyvoloski et al. 2008; El-Amrani and Seaid 2012), of which the Marker-in-Cell (MIC) method is a special form (Gerya and Yuen 2003; Gerya 2010).

Leachate dynamics of landfills require the simulation of water flow and solute transport through waste (El-Fadel et al. 1997a,b; McDougall 2007; Gholamifard et al. 2008; Fellner and Brunner 2010). Waste is highly heterogeneous material with large variations in physical properties at short distances, such as a random mixture of plastic sheets, parcels of news paper and easily degradable organic matter such as food waste (Bandara et al. 2007). This heterogeneity leads to a large local variation in flow velocities and as a result very steep gradients in solute concentrations (Cvetkovic et al. 1992; Cvetkovic and Dagan 1994; Cvetkovic et al. 1998; Wildenschild and Jensen 1999; Zadeh 2011). Interpretation of the leachate dynamics from such systems requires simulators which have very stringent mass balance criteria and which can cope with steep concentration gradients (Neuman 1984). A wide range of numerical simulation tools are available for such problems (Feyen et al. 1998; Kumar 2015).

The choice of simulation tool with respect to mass conservation and numerical diffusions depends mainly on the flexibility for modifying the governing equations. For example the choice of implementing mixed-form of RE over head-form RE in a simulation software or a programming code improves mass lumping error associated with head-form RE (Pinder and Celia, 2006). The choice of implementing Picard iteration method over Newton iteration method for solving non-linearity of RE improves the mass conservation of flow (Celia et al. 1990a). The surface ponding conditions occurring in variably saturated porous media are approximated by using the infiltration capacity formula (Green and Ampt 1911). There is a ease for implementing infiltration capacity formulas (Freyberg et al. 1980; Hsu et al. 2002; Dussaillant et al. 2004; Aravena and Dussaillant 2009; Ma et al. 2010) in a programming code compared to commercial simulation softwares with less freedom for modifications (COMSOL 4.3b). The choice for discretization of flow and transport equations is usually between the finite element method (FEM) and the finite difference method (FDM) (Simpson and Clement 2003). The FDM could serve a preference over FEM because it has a relative ease in implementing or modifying gen-

eral equations (Frehner et al. 2008). On the other hand FEM is preferred for simulations involving complex geometries (Peiro and Sherwin 2005).

In addition, numerical artifacts arising from solving the ADE are easily visible as non-physical oscillations in breakthrough curves of concentrations in time and space (Malcolm 1999). These numerical artifacts are caused by the advection term in the ADE (Malcolm 1999; Ewing and Wang 2001; Al-Lawatia 2012). The choice of an Eulerian-Lagrangian finite difference or finite element approach over upstream FDM or FEM for simulating ADE is always preferable as this prevents such problems from occurring (Malcolm 1999; Al-Lawatia 2012; Kumar 2015). Further more, Eulerian-Lagrangian approaches can significantly reduce the impact of numerical dispersion and as such it is possible to handle steeper concentration gradients (Neuman 1984). Finally, time required for running the simulations could also be an important criteria for choosing a particular simulator (Hamil and Bel 1986).

In this chapter we compare three simulators¹ based on their performance for different flow and transport scenarios in different two dimensional (2D) small scale porous systems. The first simulator was implemented in COMSOL (COMSOL 4.3b), a commercially available multi-physics finite element software package. The second simulator was implemented with the FEM open source toolbox FAESOR in MATLAB (Krysl 2010; MATLAB 2014b). The third simulator is our own 2D open-source implementation in MATLAB, named Variably Saturated Flow and Transport (VarSatFT). In VarSatFT we model water flow using the finite difference method (FDM) and solute transport using an Eulerian-Lagrangian approach. In this approach, the dispersion term is solved on Euler nodes and the advection term is solved on Lagrangian markers using modified marker-in-cell (MIC) method, inspired by the one presented by Gerya (2010). Three numerical scenarios were considered which gave us an insight of the leachate dynamics in landfills. In first scenario, we considered analysis of flow and transport for different water levels as drainage problems in homogeneous porous medium. In second scenario, we analyse flow and transport in heterogeneous unsaturated porous media which mimic waste bodies found in landfills. And in third scenario, we analysed the surface ponding with the implementation of infiltration capacity formula in heterogeneous unsaturated porous media. The performance criteria we used were mass-balance, the capacity to cope with steep gradients, time required for running the simulations and ease of implementation.

¹Note: The abbreviations used in this chapter are shown in Table2.1

Table 2.1: Abbreviations used in this chapter.

Abbreviation	Lengthen
ADE	Advection Dispersion equation
FDM	Finite Difference Method
FEM	Finite Element Method
MIC	Marker-in-Cell
RE	Richards' equation
VarSatFT	Variably Saturated Flow and Transport

2.2 Theory

2.2.1 Water Flow

The mass balance of fluid flow through porous media as shown in equation (2.1) is the starting point for each implementation.

$$\frac{\partial \rho_w \epsilon S_{eff}}{\partial t} + \nabla \cdot \rho_w \mathbf{q} = \rho_w Q_w \quad (2.1)$$

where extended form of Darcy's law, \mathbf{q} , is given as

$$\mathbf{q} = -k_r(\psi) \mathbf{K}_{sat} [\nabla(\psi + z)] \quad (2.2)$$

In which ρ_w is the density of the fluid $[M/L^3]$, ϵ is the porosity of the medium $[L^3/L^3]$, S_{eff} is the effective saturation of the medium, \mathbf{q} is the Darcy velocity $[M/L]$, Q_w is the flow source/sink term $[L^3/L^3T]$, t is the time $[T]$, ψ is the pressure head $[L]$. k_r is relative hydraulic permeability function. \mathbf{K}_{sat} is the saturated hydraulic conductivity tensor $[L/T]$, for 2D written as $\begin{bmatrix} K_{xx} & K_{xz} \\ K_{zx} & K_{zz} \end{bmatrix}$, where x is horizontal direction and z is the vertical direction assumed positive upwards.

For unsteady flow of water in slightly compressible variably saturated porous media with no source or sink term, the highly non-linear RE can be derived from equation (2.1) which expressed in its head-form (ψ -form) is written as (Pinder and Celia 2006) (See equation (2.3)).

$$(C_m(\psi) + S_w S_s) \frac{\partial \psi}{\partial t} + \nabla \cdot \mathbf{q} = 0 \quad (2.3)$$

where C_m is the differential water capacity ($\frac{d\theta}{d\psi}$) [$1/L$] in which θ is the water content which varies as a function of ψ , S_w is the water saturation, expressed as $S_w = \frac{\theta}{\theta_s}$, S_s is the specific storage coefficient, which can be presented as $S_s = \rho_w g(\theta_s \beta + C_v)$, in which, g is acceleration due to gravity [L/T^2], β is the compressibility of water [LT^2/M], C_v is the coefficient of consolidation of the soil [LT^2/M] and θ_s is the saturated water content of the medium [L^3/L^3].

The water content as a function of suction head, $\theta(\psi)$ is calculated using the van Genuchten equation (van Genuchten 1980) for the effective saturation S_{eff} ,

$$S_{eff} = [1 + (\alpha|\psi|)^n]^{-m} \quad (2.4)$$

and

$$\theta(\psi) = \theta_r + S_{eff}(\theta_s - \theta_r) \quad (2.5)$$

where θ_r is the residual water content [L^3/L^3], α is air entry value [$1/L$], n and $m = 1 - 1/n$ are van Genuchten parameters for unsaturated flow. The relative permeability was obtained using Mualems model (Mualem 1976).

$$k_r = S_{eff}^{\frac{1}{2}} \left[1 - \left(1 - S_{eff}^{\frac{1}{m}} \right)^m \right]^2 \quad (2.6)$$

so that the hydraulic conductivity can be calculated as

$$K(\psi) = k_r K_{sat} \quad (2.7)$$

The differential water capacity $\frac{d\theta}{d\psi}$ can then be written as

$$C_m = \frac{\alpha m}{1 - m} (\theta_s - \theta_r) S_{eff}^{\frac{1}{m}} \left(1 - S_{eff}^{\frac{1}{m}} \right)^m \quad (2.8)$$

In order to solve equation (2.3) we require the initial condition and a set of boundary

conditions. Hydrostatic equilibrium is chosen for the initial condition:

$$\psi(x, z, 0) = (z_{ref} - z) \quad (2.9)$$

where z_{ref} is water level in the domain $[L]$

The boundary conditions are a Neumann condition on $S1$ (See equation (2.10)) and a Robbins condition on $S2$ (See equation (2.11)). Where $S1 + S2 = S$ is the total boundary region.

$$\mathbf{q}(x, z, t) = q_{top} \quad (2.10)$$

$$\mathbf{q}(x, z, t) = K_{surf}(\psi_{amb} - \psi) \quad (2.11)$$

where q_{top} is the infiltration inflow rate $[L/T]$, K_{surf} is the surface permeability $[1/T]$ and ψ_{amb} is ambient pressure head $[L]$.

Surface ponding can occur when the infiltration is more than infiltration capacity i.e. $q_{top} > \mathbf{K}(\psi)$. The ponding can be approximated using infiltration formula (Green and Ampt 1911) of surface water balance as shown in equation (2.12).

$$\frac{d\psi_{pond}}{dt} = q_{top} - q_{IC} \quad (2.12)$$

where ψ_{pond} is ponding head at the infiltrating surface, q_{top} is the infiltration inflow rate occurring at the surface and $q_{IC} = \mathbf{K}(\psi)$ is the infiltration capacity of the infiltrating surface. During ponding conditions, the top boundary is switches to a Dirichlet boundary condition with $\psi(x, z, t) = \psi_{pond}$ on $S1$, by solving equation (2.12).

2.2.2 Solute Transport

The mass balance of solute transport through a porous medium can be written as equation (2.13) (Fetter 1993)

$$\frac{\partial \rho_w \epsilon S_w m_i}{\partial t} + \nabla \cdot \rho_w \mathbf{u}_i = \rho_w \epsilon S_w Q_{s_i} \quad (2.13)$$

where

$$\mathbf{u} = -\epsilon S_w \mathbf{D}_i \nabla m_i + \mathbf{q} m_i \quad (2.14)$$

In these equations, Q_s is the solute source/sink term [L^3/L^3T], subscript i is the number of species, m is the mass fraction [M/M], t is the time [T], \mathbf{u} is concentration flux, \mathbf{q} is the advective velocity [L/T], \mathbf{D} is hydrodynamic dispersion tensor coefficient [L^2/T], for 2D it can be written as $\begin{bmatrix} D_{xx} & D_{xz} \\ D_{zx} & D_{zz} \end{bmatrix}$. The matrix elements of \mathbf{D} can be obtained using equation (2.15) (Pinder and Celia 2006) as

$$D_{\alpha\gamma} = \alpha_T |v| \delta_{\alpha\gamma} + (\alpha_L - \alpha_T) v_\alpha v_\gamma / |v| + D_m \delta_{\alpha\gamma} \quad (2.15)$$

where

$$v = \frac{\mathbf{q}}{\theta} \quad (2.16)$$

where $D_{\alpha\gamma}$ is the dispersion coefficient in respective directions, D_m is the molecular diffusion [L^2/T], v is the linear pore water velocity [L/T]. α_L and α_T are the longitudinal and transverse dispersivities [L], respectively. The subscripts α and γ represent the x and z coordinate directions. Substitution of x and z for α and γ yields four values for the dispersion tensor. $\delta_{\alpha\gamma}$ is the Dirac delta function.

The approach for describing solute transport of a non sorbing, single component through a porous media with no source or sink term can be written as the ADE shown in equation (2.17).

$$\frac{\partial \theta c}{\partial t} - \nabla \cdot \mathbf{D} \theta \nabla c + \nabla \cdot \mathbf{q} c = 0 \quad (2.17)$$

where $c = \rho_w \cdot m$, c is concentration [M/L^3] and $\theta = \epsilon \cdot S_w$.

On further simplification we get equation (2.18).

$$\theta \frac{\partial c}{\partial t} + c \frac{\partial \theta}{\partial t} - \nabla \cdot \mathbf{D} \theta \nabla c + \mathbf{q} \nabla \cdot c + c \nabla \cdot \mathbf{q} = 0 \quad (2.18)$$

As we have coupled transport equation with the flow equation, $c \frac{\partial \theta}{\partial t} = -c \nabla \cdot \mathbf{q}$. Thus, we

can write equation (2.18) as equation (2.19).

$$\theta \frac{\partial c}{\partial t} - \nabla \cdot \mathbf{D} \theta \nabla c + \mathbf{q} \nabla \cdot c = 0 \quad (2.19)$$

where \mathbf{q} and θ are the coupling variables, mathematically presented in equation (2.2) and equation (2.5).

The initial condition for the ADE can be expressed as

$$c(x, z, 0) = c_{ini} \quad (2.20)$$

where c_{ini} is initial concentration [M/L^3]

The boundary conditions can be expressed as a Dirichlet boundary condition on $S1$ (See equation (2.21)) and a Robbins boundary condition on $S2$ (See equation (2.22)). Where $S1 + S2 = S$ is the total boundary region.

$$c(x, z, t) = c_{top} \quad (2.21)$$

$$\mathbf{u}(x, z, t) = \mathbf{q} \nabla \cdot c \quad (2.22)$$

where c_{top} is concentration at the boundary condition [M/L^3].

In the Eulerian-Lagrangian approach, the Eulerian ($\frac{\partial c}{\partial t}$) and Lagrangian ($\frac{Dc}{Dt}$) time derivatives of concentration are related to each other through an advective transport term ($\mathbf{q} \nabla \cdot c$) (See equation (2.23)) (Ewing and Wang (2001)).

$$\frac{Dc}{Dt} = \theta \frac{\partial c}{\partial t} + \mathbf{q} \nabla \cdot c \quad (2.23)$$

The Lagrangian ($\frac{Dc}{Dt}$) time derivative is related to the dispersion term as shown in equation (2.19). The dispersion term ($\nabla \cdot \mathbf{D} \theta \nabla c$) is solved on the Eulerian grid. Whereas the advective term ($\mathbf{q} \nabla \cdot c$) from the right hand side of equation (2.23) is solved with a Lagrangian method (MIC method).

In this Lagrangian method, the concentration c , and the x and z components of linear velocities \mathbf{v} are initially distributed on a large number of dimensionless markers (See equation(2.16) for \mathbf{v})(Gerya and Yuen 2003). These Lagrangian markers are advected

using equation (2.24).

$$\begin{aligned} x_{mrk}^{t+\Delta t} &= x_{mrk}^t + v_{x_{mrk}} \cdot \Delta t \\ z_{mrk}^{t+\Delta t} &= z_{mrk}^t + v_{z_{mrk}} \cdot \Delta t \end{aligned} \quad (2.24)$$

where x_{mrk}^t and z_{mrk}^t are the location of the markers in x and z direction at time t , and $x_{mrk}^{t+\Delta t}$ and $z_{mrk}^{t+\Delta t}$ are the location of the markers in x and z direction at time $t + \Delta t$. The $v_{x_{mrk}}$ and $v_{z_{mrk}}$ are the linear velocities of the markers. After advecting the markers nodal concentrations are obtained by interpolating the concentration from the markers to the surrounding nodes, while taking the boundary conditions into account. This interpolation of concentration from nodes to markers and vice-versa is carried out at every time step making this approach computational intensive.

2.3 Materials and Methods

2.3.1 Numerical implementations

In COMSOL we used the inbuilt finite element mesh generator using quadratic triangular elements with a minimum size of 0.01 m and a maximum size of 0.05 m. The Richards' equation module for water flow and Species Transport in Porous Media module were used. In COMSOL the non-linearity of head-form of RE (See equation (2.3)) was solved using Newton iteration method ² and an automatic time-stepping process. The ADE was simulated in a fully coupled mode along with the RE, with identical output time steps.

For FAESOR, we used the finite element mesh with quadratic triangular elements generated using automatic mesh generation open-source tool, NETGEN (Schöberl 2003). The mesh had a minimum element size of 0.01 m and a maximum size of 0.05 m. In FAESOR, the mixed form of RE was solved using Picard iteration (2.25) (Celia et al. 1990a).

$$\text{mixed-form } \frac{\theta^{a+1} - \theta^a}{dt} + \frac{C_m(\psi^{a+1,b}) + S_w S_s}{dt} \delta^{b+1} + \nabla \cdot \mathbf{q} = 0 \quad (2.25)$$

where a is the time level and b is the iteration stage and dt is time step and δ was obtained

²Note: Newton iteration process used in COMSOL is visible in following path. COMSOL/Study1/Solver Configurations/Solver1/Time Dependent Solver1/Fully Coupled/Automatic(Newton)

using equation (2.26).

$$\psi^{a+1,b+1} = \delta^{b+1} + \psi^{a+1,b} \quad (2.26)$$

For solving the mixed-form RE we used an automatic time stepping process constrained with number of iterations as similar to that described by Shahraiyini and Ashtiani (2012). The ADE was solved after solving the RE, where the coupling was carried out using time step averaged parameters \mathbf{q} and θ (Zhang and Kang 2004; Zhang et al. 2008). The time steps used for solving the ADE were set to the output time steps as those given by the RE. The finite element formulation and temporal discretization of water flow and solute transport equations formulated in FAESOR are given in more detail in Appendix A.

For VarSatFT, we used a staggered grid finite difference mesh (Figure 2.2). Usually a fixed size of 0.05 m for the element was used. We implemented mixed-form RE with Picard iteration for water flow (See equation (2.25) and equation (2.26)) and the ADE was solved using the Eulerian-Lagrangian approach with MIC method (Gerya 2010). The states (pressure head ψ , water content θ and concentration c) were defined on the nodes, and flux related terms (hydraulic conductivity, flow velocities, dispersion and solute flux in x and z directions) were assigned on the inter-nodes (Hayhoe 1978).

In order to be able to cope with surface ponding conditions, we implemented the infiltration capacity formula in VarSatFT. In our implementation surface ponding occurs when pressure head at the top nodes is greater than zero. Thus simplifying equation (2.12), we get

$$\frac{d\psi_{pond}}{dt} = q_{top} - q_{IC} \approx \frac{d\psi(x,0,t)}{\Delta z IN_{top} dt} \quad (2.27)$$

where, zIN_{top} is the inter-node situated at the top edge. The term $\frac{d\psi(x,0,t)}{\Delta z IN_{top}}$ is equivalent to term $d\theta(x,0,t)$, which is the ponding water accumulated on the surface. At $\psi(x,0,t) > 0$, equation (2.27) can be substituted in θ -form of RE as shown in equation (2.28). Equation (2.28) can be simplified to formulate the mixed-form of RE as shown in equation 2.25 (See Appendix B, section B.1.1).

$$\frac{\partial \theta}{\partial t} + \frac{\partial \psi(x,0,t)}{\Delta z IN_{top} \partial t} + \nabla \cdot \mathbf{q} = 0 \quad (2.28)$$

The temporal discretization of the RE in VarSatFT was implemented using an implicit backward Euler's method (Butcher 2003) and it was constrained with number of iterations as described by Shahraiyini and Ashtiani (2012). After completely solving the RE we

solved the ADE. Because in this case, solute transport has no influence on the water flow. We coupled water flow to the solute transport, using time averaged values for q and θ for each time step from the RE.

The steps for our implementation of the Eulerian-Lagrangian approach are shown as the flow chart in Figure 2.1. In this, the MIC method is initialized by distributing a predefined number markers across the model domain using a Latin Hypercube sampling algorithm (McKay et al. 1978) in order to assign a spatial coordinate to each marker. We initialized 50 markers in every element. Using the bilinear interpolation method of Gerya (2010), states like θ and c are calculated for each marker. A similar approach is used for the obtaining the local flux v . The time step used for the temporal scale is the minimum value of the time step calculated from the nodal velocities and the initially assigned fixed value.

The dispersion and advection terms are then solved for each discrete time step using a mixed Eulerian-Lagrangian approach. The idea is to solve the macroscopic diffusion and reaction equation on the Eulerian grid using a finite difference approach, followed by solving the advection part of the equation using the MIC-method. In order to achieve this, we interpolated the concentrations of the markers to the Eulerian nodes. The built-in ode15s solver of MATLAB which uses an implicit backward Euler's method (Butcher 2003) was used for simulating the dispersion and reaction terms on the Eulerian nodes. The change in concentration due to diffusion (and possible reactions) is then interpolated back to the markers followed by the sub-grid diffusion approach of Gerya (2010) in order to reduce spurious oscillations. The markers are then advected according to the computed velocity field as shown in equation (2.24) in the advection step.

In our MIC implementation in VarSatFT, we included some modifications to the MIC method presented by Gerya (2010). For every time step, all markers leaving the domain are recycled to a randomly selected point on the input boundary of the domain and allowed to flow into the domain using the assigned boundary flux and boundary concentration conditions. In order to prevent errors due to extrapolation near the edges of the domain, we included all boundary conditions to constrain the interpolation, both from nodes to markers and vice-versa. We used marker values of θ as the weighted mass for interpolating the concentrations from the advected markers to the surrounding nodes (See equation (B.16), in Appendix B). The time step for solving the MIC was the minimum of output time step obtained from RE solution, $\frac{\Delta x}{2v_x}$ or $\frac{\Delta z}{2v_z}$. This ensured that markers would only cross a single nodal boundary per time step. Appendix B gives the full discretization of the RE and the ADE based on the modified MIC-method.

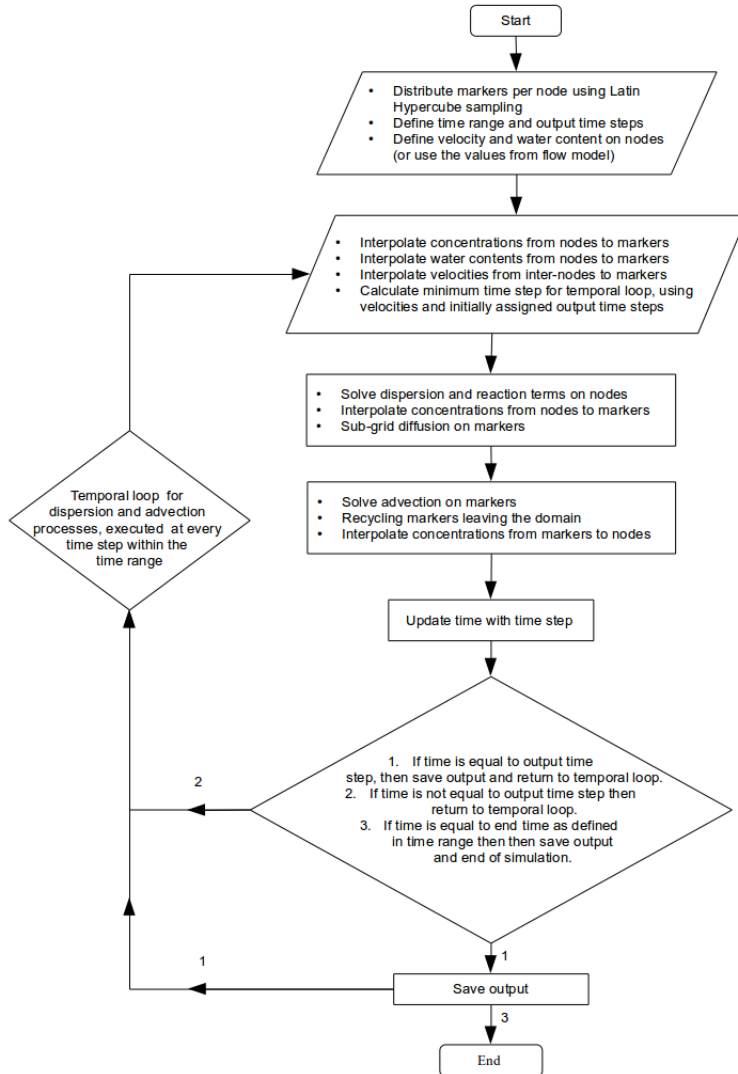


Figure 2.1: Flow chart for Eulerian-Lagrangian approach implemented in VarSatFT.

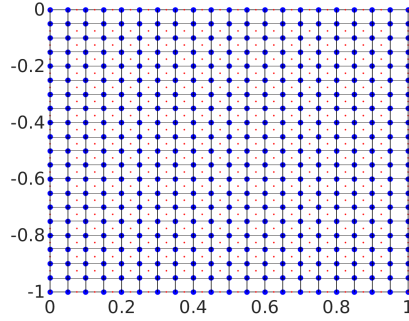


Figure 2.2: 2D grid used in VarSatFT for spatial discretization. \cdot are nodes and \bullet are inter-nodes.

2.3.2 Evaluation Criteria

In order to compare the performance of the three different implementations, we evaluate the mass balance error of the different simulators. The discrete form for the total mass balance for the water flow and solute transport model are given in equations (2.29) and (2.30) respectively.

The mass balance for the water flow model is given as

$$MB_w(t^a) = \left[\begin{array}{c} \sum(\theta^{a+1} - \theta^a)\Delta V - \\ \sum[-q_{X_{in}}^{a+\frac{1}{2}}\Delta z_{in} - q_{X_{out}}^{a+\frac{1}{2}}\Delta z_{out}] + \\ \sum[-q_{Z_{in}}^{a+\frac{1}{2}}\Delta x_{in} - q_{Z_{out}}^{a+\frac{1}{2}}\Delta x_{out}] \end{array} \right] \Delta t \quad (2.29)$$

where θ^a and θ^{a+1} are the water contents at the beginning and end of each time step, $q_{X_{in}}^{a+\frac{1}{2}}$, $q_{X_{out}}^{a+\frac{1}{2}}$, $q_{Z_{in}}^{a+1}$ and $q_{Z_{out}}^{a+1}$ are the Darcy velocities flowing in and out of the domain in x and z direction averaged over the time step t^a to t^{a+1} . The volume of the elements in the domain are ΔV . The Δx_{in} , Δz_{in} , Δx_{out} and Δz_{out} are the areas of the elements of the input and output boundaries.

The mass balance for the solute transport model is given as

$$MB_s(t^a) = \left[\begin{array}{c} \sum(\theta^{a+1}c^{a+1} - \theta^ac^a)\Delta V - \\ \sum[-u_{X_{in}}^{a+\frac{1}{2}}\Delta z_{in} - u_{X_{out}}^{a+\frac{1}{2}}\Delta z_{out}] + \\ \sum[-u_{Z_{in}}^{a+\frac{1}{2}}\Delta x_{in} - u_{Z_{out}}^{a+\frac{1}{2}}\Delta x_{out}] \end{array} \right] \Delta t \quad (2.30)$$

where the c^a and c^{a+1} are the solute concentrations at the beginning and end of each time step. $u_{X_{in}}^{a+\frac{1}{2}}$, $u_{X_{out}}^{a+\frac{1}{2}}$, $u_{Z_{in}}^{a+\frac{1}{2}}$ and $u_{Z_{out}}^{a+\frac{1}{2}}$ are the solute fluxes flowing in and out of the domain in x and z direction averaged over the time step t^a to t^{a+1} . For ideal conditions

the $MB_w(t)$ and $MB_s(t)$ should always be 0 m^3 and 0 kg respectively.

In COMSOL and FAESOR the solute flux was the addition of dispersion and advection flux terms. Whereas in VarSatFT the solute flux, was calculated from the markers crossing the nodal boundaries during each time step (See equation (B.27), in Appendix B). The water and solute mass balance for COMSOL was calculated using its inbuilt Global ODEs and DAEs module.

2.4 Results and Discussion

We considered three numerical scenarios. For the first scenario, we analysed three drainage problems (D1, D2 and D3) for three different initial saturations for the same homogeneous system. The second scenario, is an applied problem (AP1) where we analysed a complex spatial heterogeneity under unsaturated conditions where an intermittent infiltration pattern was applied as the inflow boundary condition. The third scenario is an applied problem (AP2) where we analysed the effect of surface ponding for a complex spatial heterogeneity under unsaturated conditions where an intermittent infiltration pattern was applied as the inflow boundary condition.

2.4.1 Numerical Scenario 1 - Drainage Problems

The first scenario aims to test the performance of the three simulators for drainage problems. These illustrative drainage problems have different initial water levels, with zero infiltration at the top edge and drainage against fixed suction head at the bottom edge. The change from a fully saturated domain to an unsaturated domain is challenging for the numerical solvers of Richards' equation due to the very non-linear nature and stiffness of the partial differential equation caused by the $C_m(\psi) + S_w S$ term in equation 2.3.

All the drainage problems were carried out on a 2D homogeneous square domain of $1.0 \text{ m} \times 1.0 \text{ m}$ consisting of coarse sand. The simulation was carried out for 365 s. We choose a homogeneous geometry to minimize dispersion. The material properties of the coarse sand and the required parameters for initial and boundary conditions are listed in Table 2.2 and Table 2.3.

When starting from an initially fully saturated domain at hydrostatic conditions, the drainage process due to step change in the bottom boundary occurs in four main stages. In stage 1, the hydrostatic pressure head distribution must change to a zero gradient pressure head distribution along the vertical axis before flow can occur from the top of the column. During this stage, the pressure head is positive everywhere in the column and the profile is fully saturated. No change in water content can occur. As soon as the zero gradient condition is achieved at the top of the profile, stage 2 commences and water starts to drain by

Table 2.2: Assumed material properties for coarse sand and fine clay.

Material parameters	Coarse Sand	Fine Clay
α [m^{-1}]	2.00	1.00
n	1.50	2.5
θ_r [$\text{m}^3 \text{m}^{-3}$]	0.04	0.08
θ_s [$\text{m}^3 \text{m}^{-3}$]	0.40	0.45
\mathbf{K}_{sat} [m s^{-1}] in xx and zz direction	5.00×10^{-2}	5.00×10^{-5}

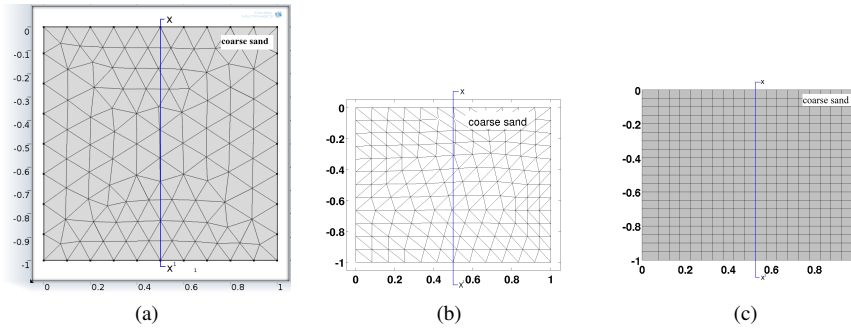


Figure 2.3: Mesh used in COMSOL (a), FAESOR (b) and VarSatFT (c) for D1, D2 and D3.

gravity and the system becomes unsaturated from the top as the water table drops leading to stage 3, suction controlled drainage. The zero gradient profile will be maintained until the column becomes unsaturated at the bottom. At this moment the pressure head at the bottom of the column will quickly move towards the applied bottom boundary condition will be reached. The drainage rate decreases as the column dries out due to a decreasing relative permeability. This continues until stage 4, when finally a hydrostatic condition is achieved, in equilibrium with the applied bottom boundary condition.

Figure 2.4 shows the pressure head and water content distributions at different times along section $x-x^1$ through the coarse sand material. As the considered meshes in the different simulators were not exactly same, we discretized section $x-x^1$ into 100 intervals of 0.02 m size and obtained the values along this discrete mesh through linear interpolation.

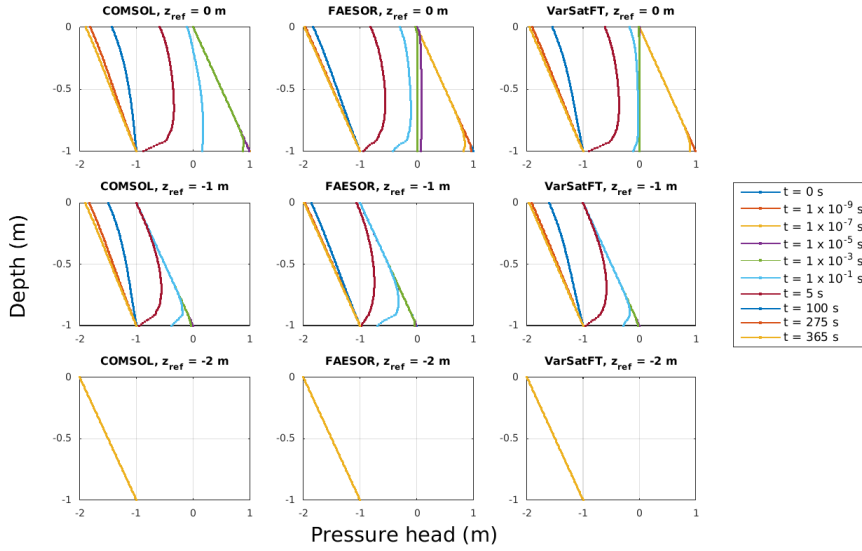
All three implementation show the expected four stages in the drainage, although there are significant differences in the early stages of drainage, when the column is still (fully) saturated. The results from the COMSOL implementation show no real change in pressure head along the profile until $1 \times 10^{-5}\text{s}$, where the profile is still fully saturated. Both the FAESOR and VarSatFT implementation show a stepwise decrease in the

Table 2.3: Coupled model parameters.

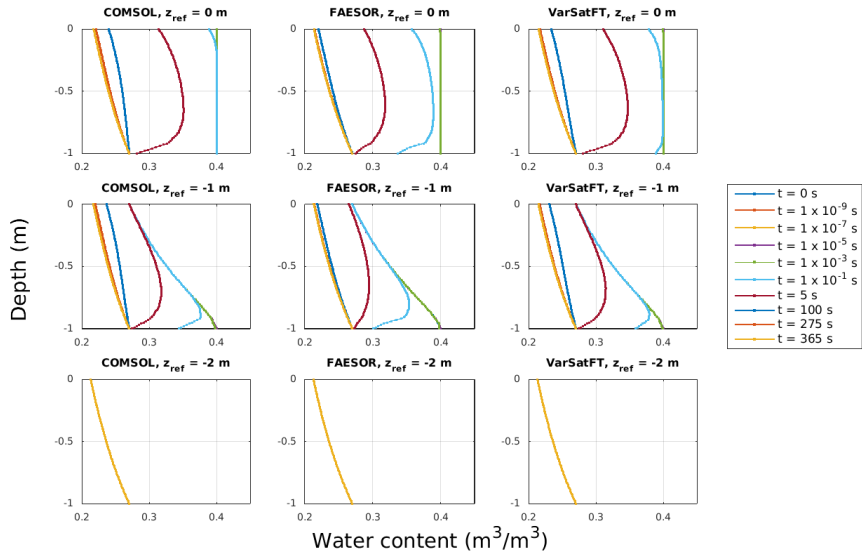
Assumed material properties and values for initial and boundary conditions	Assumed values for verification problem		
	D1	D2	D3
z_{ref} [m]	0	-1.00	-2.00
q_{top} [m s^{-1}]	0	0	0
K_{surf} [s^{-1}]	5.00×10^{-2}	5.00×10^{-2}	5.00×10^{-2}
ψ_{amb} [m]	-1.00	-1.00	-1.00
c_{ini} [kg m^{-3}]	1.00	1.00	1.00
c_{top} [kg m^{-3}]	0	0	0
α [m^{-1}]	2.00	2.00	2.00
n	1.50	1.50	1.50
θ_r [$\text{m}^3 \text{m}^{-3}$]	0.04	0.04	0.04
θ_s [$\text{m}^3 \text{m}^{-3}$]	0.40	0.40	0.40
\mathbf{K}_{sat} [m s^{-1}] in xx and zz direction	5.00×10^{-2}	5.00×10^{-2}	5.00×10^{-2}
β [$\text{m s}^2 \text{kg}^{-1}$]	4.00×10^{-10}	4.00×10^{-10}	4.00×10^{-10}
C_v [$\text{m s}^2 \text{kg}^{-1}$]	0	0	0
D_m [$\text{m}^2 \text{s}^{-1}$]	1.00×10^{-10}	1.00×10^{-10}	1.00×10^{-10}
α_L [m]	0.10	0.10	0.10
α_T [m]	0.01	0.01	0.01

Table 2.4: Cumulative mass balances in D1, D2 and D3.

Drainage Problems	<u>COMSOL</u>		<u>FAESOR</u>		<u>VarSatFT</u>	
	z_{ref} [m]	Water[m ³]	Solute [kg]	Water [m ³]	Solute [kg]	Water [m ³]
0	1.76	2.03	0.24	0.27	4.55×10^{-6}	0.02
-1	1.55	1.67	0.12	0.13	6.43×10^{-7}	0.01
-2	1.18	1.14	1.45×10^{-15}	1.27×10^{-7}	4.92×10^{-16}	2.77×10^{-16}



(a)



(b)

Figure 2.4: Pressure head (a) and water content (b) along x - x^1 section along the depth at time 0, 1×10^{-9} , 1×10^{-7} , 1×10^{-5} , 1×10^{-3} , 1×10^{-1} , 5, 100, 275, 365 s in COMSOL, FAESOR and VarSatFT in D1, D2 and D3.

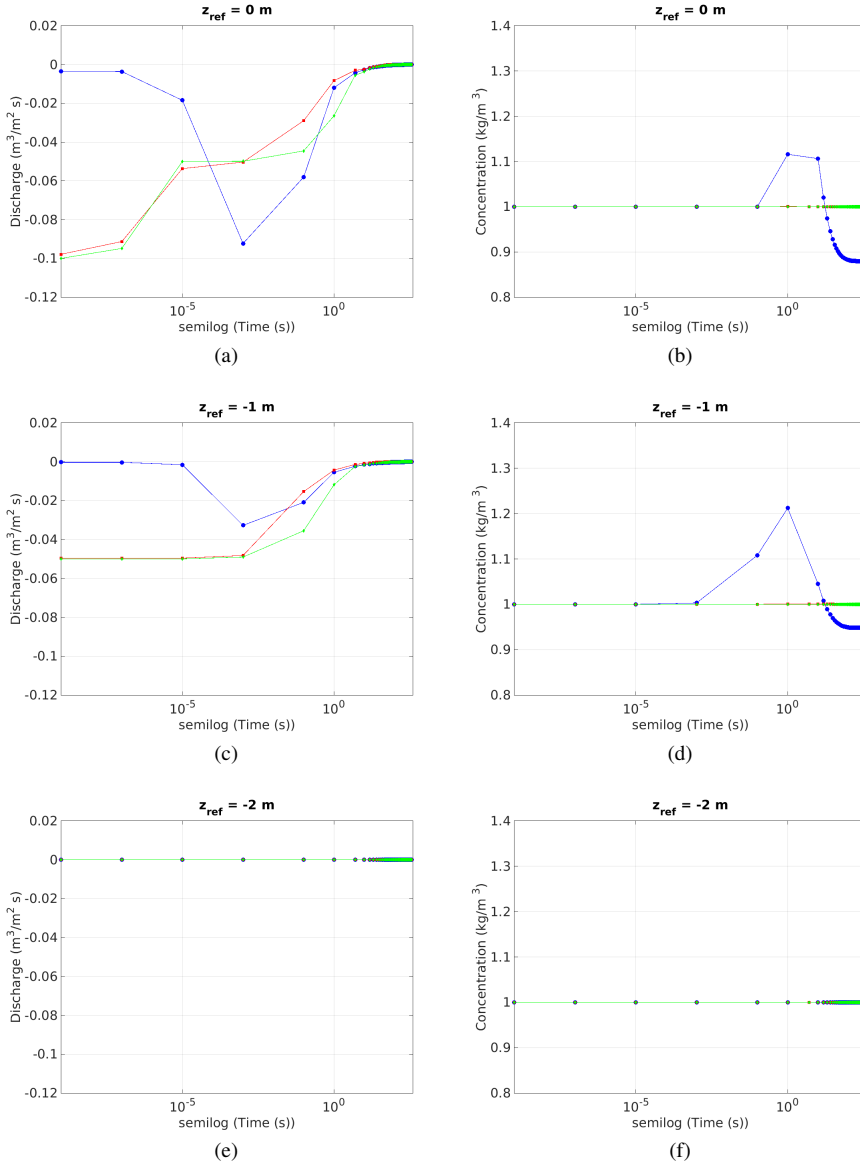


Figure 2.5: Average total discharge and solute concentration obtained from drainage in time for D1, D2 and D3 where ● COMSOL, ■ FAESOR, ▲ VarSatFT.

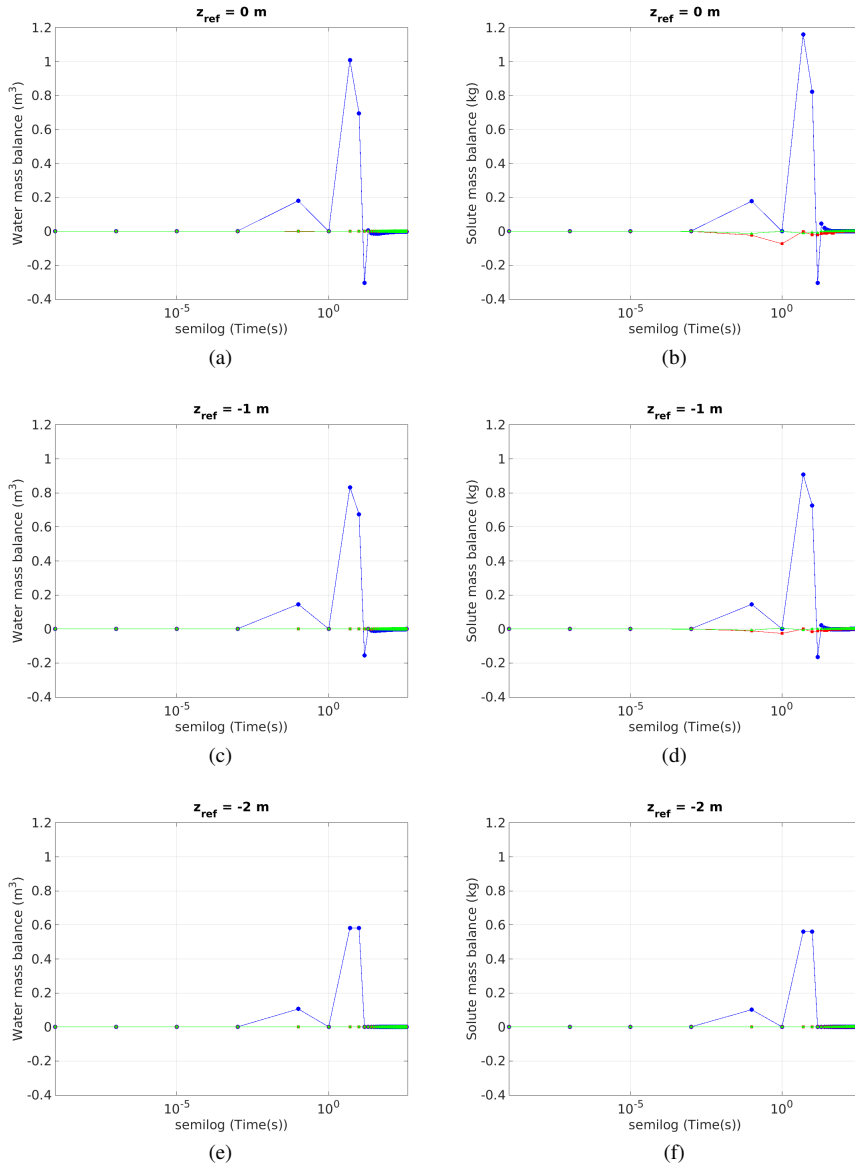


Figure 2.6: Mass balance for water and solute in time for D1, D2 and D3, where ● COMSOL, ■ FAESOR, ▲ VarSatFT.

pressure head towards the expected zero gradient profile. However, at 1×10^{-5} s, the column is fully unsaturated, contrary to the result from the COMSOL implementation. The COMSOL has a built-in approach to handle stiff (initial) problems which is different from the other two implementations where the main approach was to force the simulation to continue when a minimum time step has been reached at the cost of some error. The consequence of this difference is clearly shown in Figure 2.5 where the initial discharge rate estimated in the COMSOL implementation is correctly close to zero, whereas both other implementations calculate a high discharge rate. The consequence of the error in the FAESOR and VarSatFT implementation is, however, relatively small because of the very small time steps at the beginning of the simulation. When the system becomes unsaturated the differences in simulated pressure heads, water contents and discharge rates between the different implementations becomes very small.

The expected concentration in the drained water should be constant with time and equal to the initial concentration in the column. This condition is achieved for both the FAESOR and the VarSatFT implementations, however the COMSOL implementation differs significantly from the initial concentration ($1\text{kg}/\text{m}^3$). This is due to the way the solution for the advective solute transport problem is implemented. In COMSOL we used the default solver and did not apply any of the more advanced solutions available to limit numerical oscillations that occur when solving the advection problem on a variable grid. In FAESOR, the solver is based on calculating the upwind gradients, whereas in VarSatFT, the advection is solved with the MIC method.

The errors in the mass balances of water and solute in the different implementations are shown in Figure 2.6. Clearly the error water mass balance of the COMSOL implementation is unacceptably high, where the errors in the FAESOR and VarSatFT implementation are very small. This is due to the implementation of the Picard iteration method in the last two. An error in the water balance leads to a significant error in the solute mass balance because advective solute transport is highly related to water flow. The cumulative mass balance errors are given in Table 2.4 and clearly the VarSatFT implementation, based on the Picard iteration and the MIC methods has the smallest mass balance errors.

From this result we conclude that the default COMSOL implementation gives the most correct results for the initial stages of drainage in a fully saturated condition, however, the error in the mass balance and the numerical errors occurring during the solution of the advection problem are very large. Both the FAESOR and VarSatFT implementation have a small error in the initial stages of for the saturated drainage problem, but have much smaller mass balance errors and are less hampered by the errors in the solution of the advection equation.

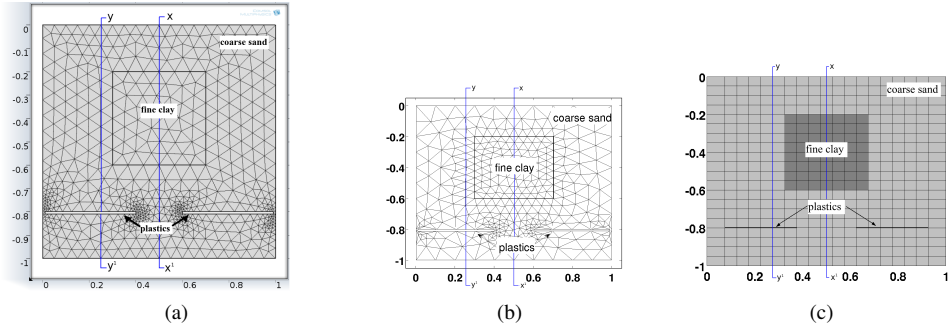


Figure 2.7: Mesh used in COMSOL (a), FAESOR (b) and VarSatFT (c) for API.

2.4.2 Numerical Scenario 2 - Application Problem 1

The second scenario aims to test the performance of the three simulators for a domain containing a heterogeneous distribution of high and low permeability materials combined with plastic sheets, mimicking a situation that can occur in the waste body of a landfill. The domain is initially unsaturated and subjected to an intermittent inflow boundary condition at the top. The bottom boundary is a Robbins conditions with a fixed boundary head.

The meshes generated for the domains used for this problem for the three simulators are shown in Figure 2.7, while the material properties are listed in Table 2.2. In VarSatFT, the effect the impermeable plastic layers are obtained by assigning $K = 0 \text{ m s}^{-1}$ at the required inter-nodes (See Figure 2.7 (c)). In COMSOL and FAESOR (NETGEN used for FAESOR) the plastics were implemented as cut out sections of $0.39 \text{ m} \times 0.01 \text{ m}$ size in the meshes with a no-flow boundary to provide the effect of an impermeable plastic (See Figure 2.7 (a) and (b)). Introduction of these cut out sections increased the number of elements in the meshes used in COMSOL and FAESOR in comparison with the mesh used for VarSatFT.

For this problem we used the same initial condition and bottom boundary condition as used for drainage problem D3 (See Table 2.3). We use a sine wave pattern infiltration where the infiltration rate varies between $-5.00 \times 10^{-3} \text{ m s}^{-1}$ and 0 m s^{-1} as the top boundary condition (See Figure 2.8). The analysis of flow and transport was carried out for a duration of 365 s for all simulators.

The expected pattern in variation in pressure heads and water contents in this 2D domain will be determined by the domains where flow occurs. The variation in the flow domain will be large, variation in the no-flow domain will be limited. The numerical implementations are expected to give different results due the differences in mesh type and size. In addition the solution of the solute transport problem will strongly influenced by mass balance errors, and the type of solution of the ADE equation. In the scenario

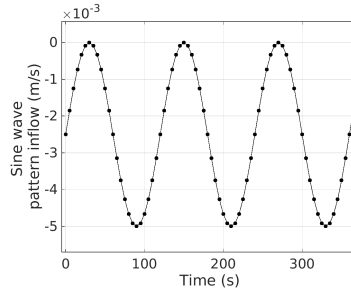
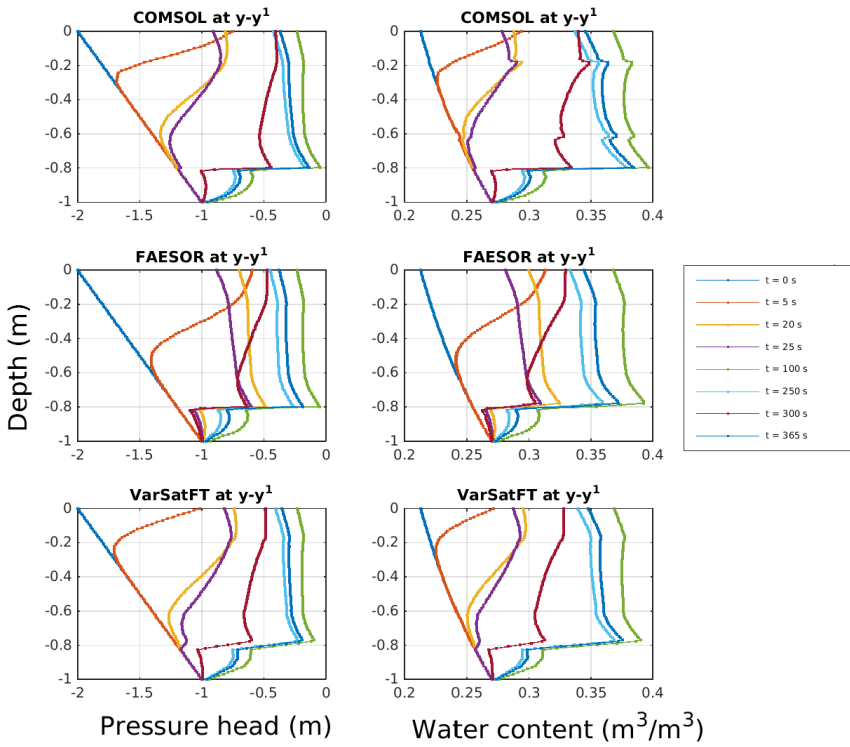


Figure 2.8: Infiltration boundary in AP1.

Figure 2.9: Pressure head and water content along $y-y^1$ section along the depth at time 0, 5, 20, 25, 100, 250, 300, 365 s in COMSOL, FAESOR and VarSatFT in AP1.

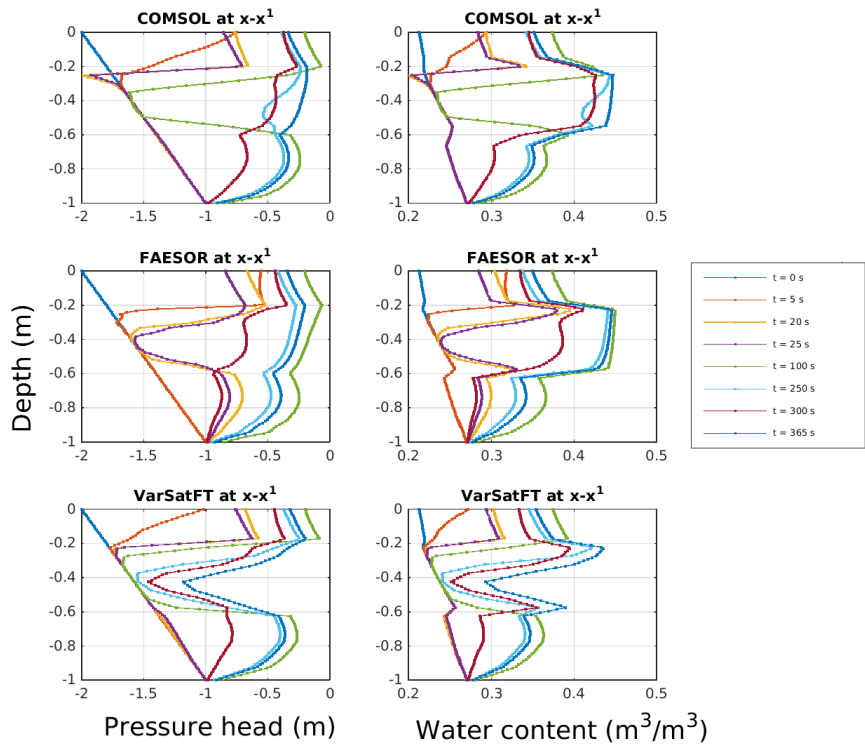
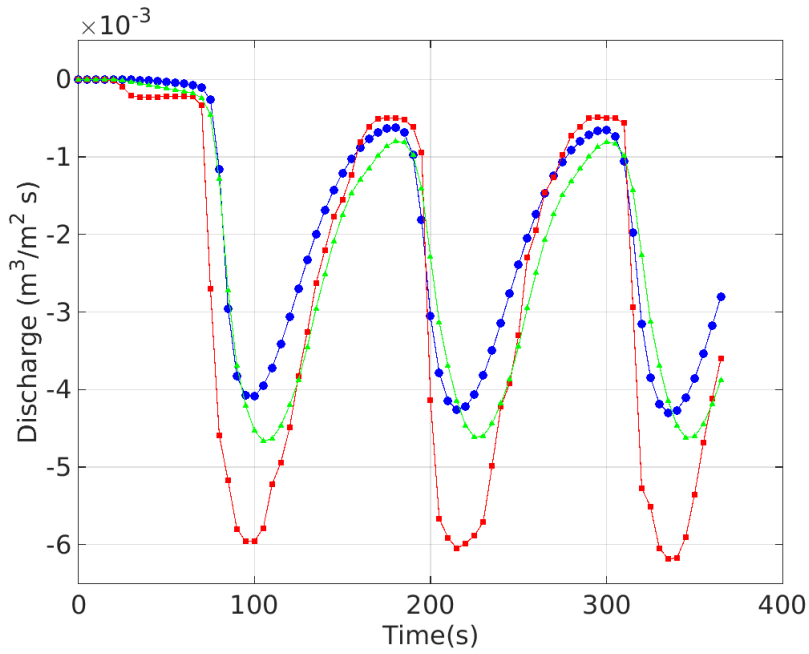


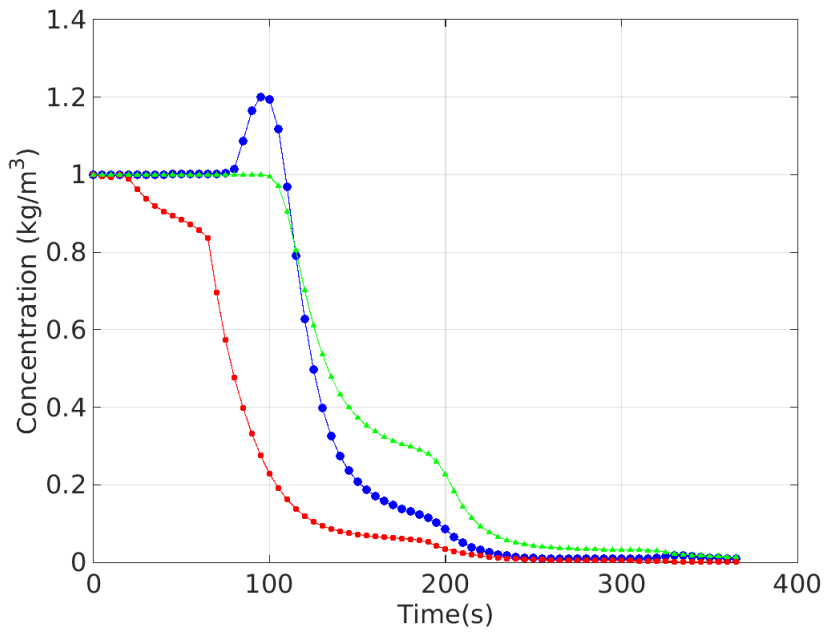
Figure 2.10: Pressure head and water content along $x-x^1$ section along the depth at time 0, 5, 20, 25, 100, 250, 300, 365 s in COMSOL, FAESOR and VarSatFT in AP1

Table 2.5: Cumulative mass balances in AP1.

<u>COMSOL</u>		<u>FAESOR</u>		<u>VarSatFT</u>	
Water [m ³]	Solute [kg]	Water [m ³]	Solute [kg]	Water [m ³]	Solute [kg]
1.92	1.14	0.17	0.14	1.82×10^{-6}	0.04



(a)



(b)

Figure 2.11: Discharge in time (a), solute concentration of the discharge in time (b) in API, where (● COMSOL, ■ FAESOR, ▲ VarSatFT).

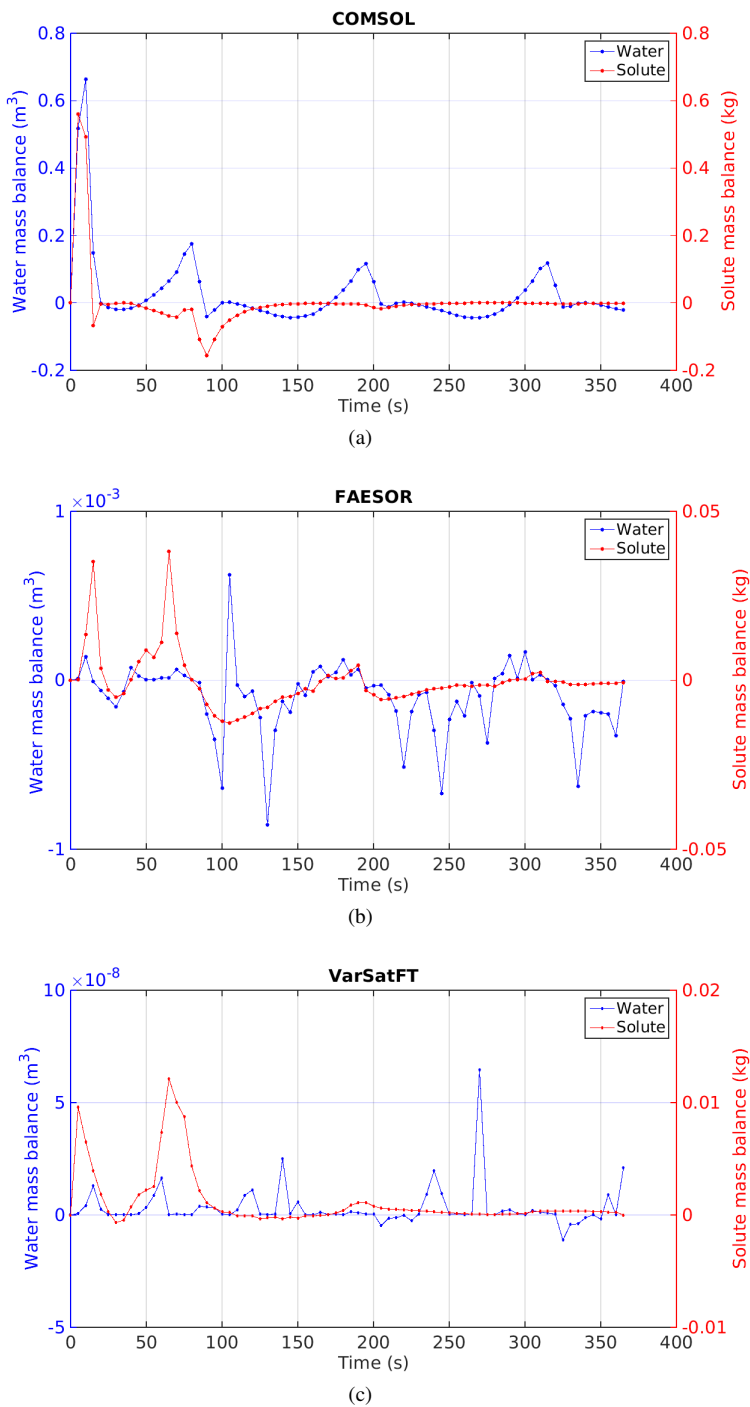


Figure 2.12: Mass balances in time duration in COMSOL (a), FAESOR (b), and VarSatFT (c) in API.

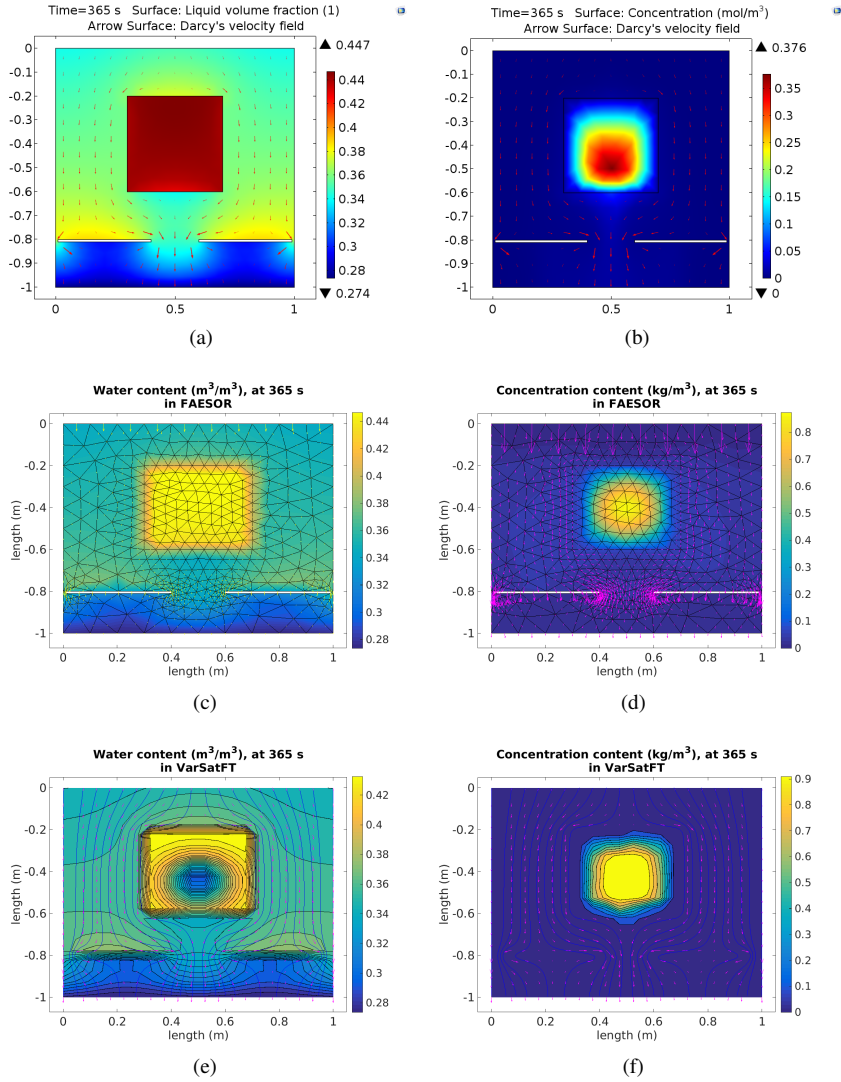


Figure 2.13: Spatial distribution of water and concentration in COMSOL (a),(b) and FAESOR (c),(d) and VarSatFT (e),(f) for AP1.

Table 2.6: Computation time required for API.

Numerical Simulator	Computation time [s]
COMSOL	1080
FAESOR	248750
VarSatFT	351

API, we expect the flow to spread horizontally on top of the plastics and fine clay block due to difference in vertical permeability the resulting build-up of a horizontal gradient in pressure head. In addition, solute quickly flushes from the zones where water flow occurs due to advection whereas it will slowly leach from the zones with no flow by mainly diffusion (driven by the concentration gradient between the no-flow and flow domains).

Figures 2.9 and 2.10 show the pressure head and water content distributions along the depth at different times at sections $y-y^1$ and $x-x^1$ through domain across the plastic and clay material. In order to facilitate a direct comparison of the different implementations, sections $y-y^1$ and section $x-x^1$ are discretized into 100 intervals of 0.02 m size and state values are linearly interpolated to these meshes. The results show that all three implementations give very similar results, the major differences can attributed to the differences in the mesh resolution used and the interpolation applied during the post-processing. In Figure 2.9 the effect of the plastic barrier is clearly shown in the graphs at -0.8 m. Here the larger mesh in the VarSatFT and the consequence of the interpolation in post-processing is clearly seen. In order to have a better comparison of the results the mesh sizes should have been comparable, however, for the FAESOR implementation that would have resulted in unacceptably high computation times (see Table 2.6), however for VarSatFT, the mesh can easily be refined.

The effect of the block of low permeability material is shown in Figure 2.10. Here the three implementations differ considerably from each other. Both the COMSOL and FAESOR implementation calculate a very large amplitude in water in the centre of the low permeable block ranging from saturated during the peak of infiltration and in equilibrium with the bottom boundary condition at the lowest value of infiltration, whereas the amplitude in the VarSatFT implementation is much smaller. In the VarSatFT result, the centre of the fine clay remains relatively dry throughout the simulation. Given the large difference in permeability between the surrounding coarse sand and the fine clay, the results from the VarSatFT implementation are more realistic. This difference is caused by the difference in how permeability is averaged across the mesh in the different simulators.

The patterns in discharge rate and concentration in the discharged water as a function

of time are shown in Figure 2.11. Because the simulation starts with a relatively dry hydrostatic condition, the saturation in the domain has to increase before discharge starts to occur, then a the discharge will follow the input cycle, but with a phase delay due to local storage in the domain. The concentration in the discharged water is initially at initial condition and then decreases when dilution and flushing with fresh water has reached the bottom. The results clearly show that the three implementations give very different results. The amplitude in the discharge rate for the COMSOL implementation largest followed by the VarSatFT implementation and then finally the FAESOR. This corresponds to the amplitude in the water content of the fine clay, during the cycle, the fine clay varies between fully saturated and the water content in equilibrium with the applied lower boundary condition. In the VarSatFT this variation is much smaller. For the FAESOR implementation, the initial discharge occurs one cycle earlier than the other two. This could be due the courser mesh.

The three implementation also show a very different solute breakthrough curve. The FAESOR implementation has the earliest breakthrough, due to a combination of the early discharge and a severe numerical dispersion in the implementation of the ADE. The COMSOL implementation has much less numerical dispersion, however it is hampered by a significant numerical oscillation near initial break through. The MIC solution to the ADE in the VarSatFT implementation has neither of these problems. The evolution of the mass balance errors in time for all three implementations is shown in Figure 2.12. Clearly the VarSatFT implementation has the smallest mass balance error, although the solute mass balance is still rather high, especially when compared with the Drainage scenario earlier. This is most likely to the averaging of the water flow over time before solving the ADE. Over the time step, water content will change non-linearly, and for the solute transport this change is not approximated linearly.

The numerical scenarios described in this chapter were simulated in a computer system of 4 x intel (R) Core(TM) i3 CPU, 16 GB memory configuration. In Table 2.6 the computation time required for simulating the AP1 scenario shows a decrease in computation time from FAESOR > COMSOL > VarSatFT. In the AP1 scenario, the intersecting edges for different soil materials and the cut out sections for implementing the presence of impermeable plastics increases the number of elements in COMSOL and FAESOR. In VarSatFT including the plastic impermeability is simply implemented by assigning hydraulic conductivities as zero leading to a much smaller number of elements.

Figure 2.13 shows the spatial distribution of the water content and solute concentration at the end of the simulation. The low permeability of the fine clay and the plastics give rise to a local ponding of water, however, the horizontal permeability in the domain is so large that the course sand is unsaturated at this time. Clearly the stream lines are strongly affected by the presence of the low permeable materials. The remaining solute

concentration in the different implementations is quite different. The results from COM-SOL implementation indicate that a significant amount of leachate has already leached, whereas the VarSatFT results indicate a significant amount of solute remaining in the fine clay. This difference is caused by the much smaller advective flow through the fine-clay and the smaller numerical diffusion in the VarSatFT implementation. This result clearly shows how important it is to accurately model the solute transport in such systems, especially when the aim is to understand leaching of solutes from heterogeneous domains such as waste bodies. Preferential flow through highly permeable materials leads to strong gradients in pressure head and concentrations. Too much averaging and too much numerical dispersion will lead to a non-realistic large leaching of solutes, eventually leading to an underestimation in remaining solute content in the waste body.

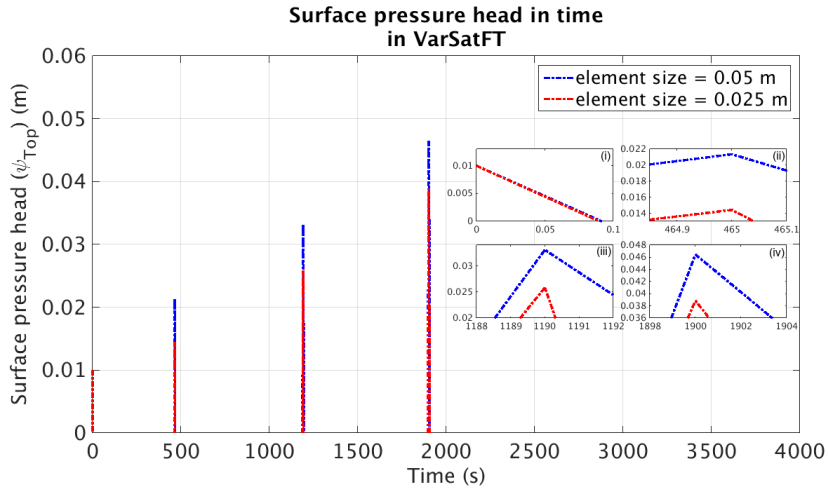
2.4.3 Numerical Scenario 3 - Application Problem 2

The previous two numerical scenarios indicate that the VarSatFT simulator can handle variably saturated conditions and steep concentration gradients caused by heterogeneities and intermittent infiltration patterns. VarSatFT also has a good mass balance performance, small numerical dispersion and a relatively small simulation time. In addition, being open source and implemented in MATLAB it is easy to implement add-ons. To further test VarSatFT we implement the infiltration capacity formula to allow for surface ponding conditions as seen on landfill surfaces during heavy rains or irrigation processes (Zhu et al. 2009; Heimovaara et al. 2010). In this scenario, we test the effect of surface ponding on an unsaturated profile to which an intermittent infiltration is applied as a top boundary condition for the same heterogeneous domain as used for scenario AP1.

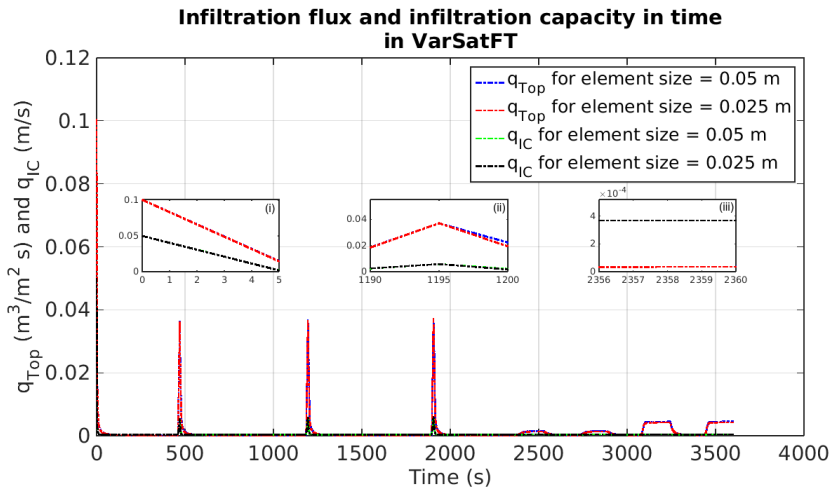
For the initial condition we assumed that the water level is at $z_{ref} = 0.01$ m. A time variant intermittent boundary condition was applied at top edge consisting of intermediate spiking infiltration rates increasing from $-4.00 \times 10^{-2} \text{ m s}^{-1}$ for 458-468 s, $-4.30 \times 10^{-2} \text{ s}$ for 1183-1193 s to $-4.60 \times 10^{-2} \text{ m s}^{-1}$ for 1893-1903 s followed by square pattern infiltration of rates $-1.00 \times 10^{-3} \text{ m s}^{-1}$ for 2160-2880 s and $-3.00 \times 10^{-3} \text{ m s}^{-1}$ for 2881-3600 s. The lower boundary condition was same as that used in AP1.

The simulation was carried out for two different meshes with element size 0.025 m and 0.05 m in order to show the effect of element size of mesh on the flow and solute transport results. The duration of simulation was 3600 s.

When the infiltration rate is larger than the infiltration capacity a ponding head should develop. In Figure 2.14(a), surface ponding is seen as positive pressure head at initial time ($t = 0$ s) and during spiking infiltrations at times 470 s, 1195 s and 1905 s. Enlarged plot (iv) shows the maximum of the ponding heights observed during the whole simulation. Clearly mesh size has a significant effect on the result, in order to accurately simulate ponding a finer grid is required. This is due to the linearisation of the steep gradient



(a)



(b)

Figure 2.14: Surface pressure head in time duration (a), Infiltration flux and infiltration capacity in time (b) for mesh with element size 0.05 m and 0.025 m in AP2.

Table 2.7: Cumulative mass balances in AP2.

Element size	VarSatFT	
[m]	Water [m ³]	Solute [kg]
0.05	0.06	0.05
0.025	0.03	0.05

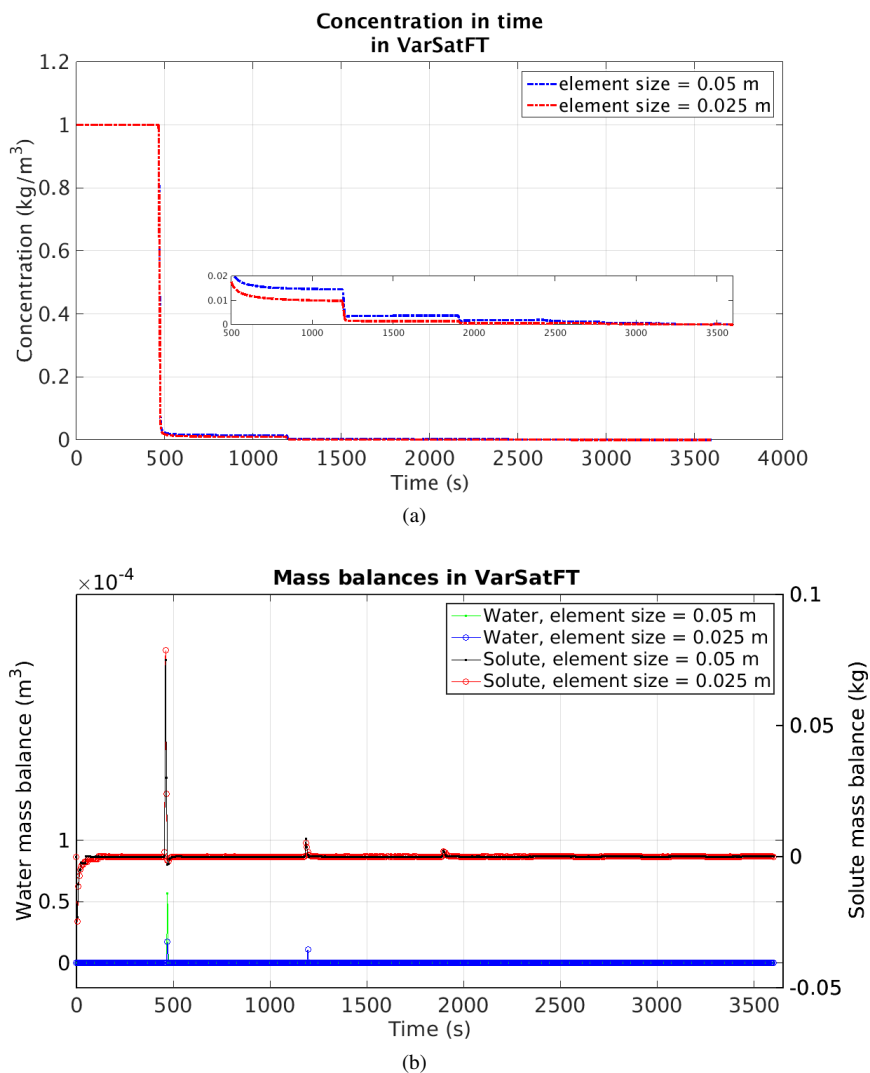


Figure 2.15: Outlet concentration in time (a), mass balances (b) for mesh with element size 0.05 m and 0.025 m in AP2.

between the top nodes of the domain (Berinnger et al. 2011; Arnold 2015).

Figure 2.14(b) shows the infiltration flux and infiltration capacity along the time duration. The sign of infiltration flux is changed into positive value so as to compare its magnitude with infiltration capacity. The enlarged plots (i) and (ii), clearly show that surface ponding arises when the infiltration rate is larger than the infiltration capacity.

Figure 2.15(a) shows the solute concentration in the discharged water as a function of time. The finer mesh shows the steepest breakthrough curve (indicated in the enlarged plot) because less spatial averaging occurs.

Figure 2.15 (b) shows the mass balances for both water and solute as a function of time. Table 2.7 summarizes the cumulative mass balances. The mass balance for water flow is better for mesh with finer element size. Whereas the mass balance for solute transport is same irrespective of element size in mesh.

The results in this scenario indicates that the finer element size provides better convergence and has better mass balances. From these results, finer elements sized mesh can be recommended to attain more accurate results. This numerical scenario also shows VarSatFT can handle surface ponding during dynamic inflow conditions.

2.5 Conclusions

In this chapter, we compared three implementations of the unsaturated water flow and solute transport problem in order to analyse leachate dynamics for steep concentration gradients inside domains that are similar to a waste bodies found in landfills. The simulators were implemented in COMSOL (tm) and FAESOR, an open source MATLAB toolbox and in MATLAB directly (our own implementation named VarSatFT, as a MATLAB toolbox). A detailed description of the flow and transport model implemented in FAESOR and VarSatFT is presented. Solute transport is implemented in VarSatFT, with the modified MIC method in order to overcome the problems related to numerical artefacts which occur when solving the advection problem.

The simulators were tested using different scenarios in order to obtain insight in to their performance under different conditions. The aim is to select the best simulator for studying leachate dynamics in waste bodies. The simulator built in COMSOL, is based on the inbuilt module of head-form RE for water flow however COMSOL has large mass balance errors due to a poor linearisation of the non-linear mass matrix term in the mixed form Richards' equation. The default solver for the ADE suffered from oscillations in the solution of the advection term in the solute transport equation. The implementation of the Picard iteration method in the FAESOR and VarSatFT simulators improved the water mass balance significantly compared with the COMSOL solver. The implementation of the solute transport solver in FAESOR was seriously influence by numerical dispersion.

The combination of the Picard iteration method for solving the Richards' equation with the MIC method for the solute transport lead to the lowest mass balance errors of all three implementations with still acceptable computational times. The different scenario results showed that VarSatFT can produce physically realistic solute break through curves while still being able to simulate steep concentration gradients caused by dynamic inflow boundary conditions and heterogeneities in the model domain.

The FDM implementation of VarSatFT is easier than the FEM implementation in FAE-SOR. However, the advanced user-interface of COMSOL, makes this the most easy interface to start with, however we have not been able to implement the Picard iteration method in COMSOL. The scenarios also showed that it is much easier to implement zero permeability boundaries within the model domain with the FDM method of VarSatFT than with the FEM methods of both FAE-SOR and COMSOL. Therefore we conclude that the VarSatFT toolbox is a very useful tool to investigate leaching from heterogeneous porous media such as waste bodies in landfills. The simple scenarios applied for the comparison indicate that solute leaching is very easily overestimated if simulators cannot accurately handle mass balances and steep gradients.

Chapter 3

Numerical study investigating origin of preferential flow and controlling factors of non-equilibrium in transport for small scale systems

Abstract

Leachate emission from municipal solid waste landfills is one of the largest long term impacts on groundwater environment. Landfills are heterogeneous and in many cases unsaturated porous systems. We believe this leads to the emergence of preferential pathways for water moving through the landfill. In this research, we explore the origin of preferential flow in small scale porous systems which we consider to be analogues for a landfill, using a two dimensional deterministic model. In the model, water flow is described with Richards' equation and non-sorbing, single component, solute transport with the advection dispersion equation. We implemented a number of scenarios consisting of dry soil domains with known heterogeneity and known material properties to which water is added from the top with varying infiltration patterns and rates. The flow and transport through heterogeneous systems are compared with a homogeneous soil domain system undergo-

ing a similar infiltration regime. The results clearly show that material heterogeneity, infiltration patterns and rates are responsible for the occurrence of preferential pathways and macro-scopic non-equilibrium in the transport of solutes. Using these numerical results we discuss (i) how preferential flow can affect emission potential of landfill; (ii) why single continuum modelling methods are infeasible for full scale landfill; and (iii) the suitability of different modelling methods for modelling a full scale landfill.

Keywords: flow and transport, preferential flow; non-equilibrium; landfill emission potential.

3.1 Introduction

Landfilling is considered as a final storage solution for removing unwanted materials from our society. Modern landfills are advanced technological installations aimed to separate the waste body from the environment. They provide means for capturing and handling adverse emissions such as landfill gas and leachate. Research on landfills carried out in the last couple of decades, has shown that landfilled waste is subjected to a range of natural processes which reduces the emission potential of the waste (Heimovaara 2011). Emission potential can be defined as a remaining amount of quantities of pollutants present inside landfill (Bun et al. 2013). This inspired the development of engineered approaches based on recirculation of leachate and aeration (Pohland and Alyousfi 1994; El-Fadel 1999; McCreanor and Reinhart 1999; Read et al. 2001; Hudgins et al. 2000; Warith and Takata 2004; Haydar and Khire 2005; Haydar et al. 2006; Haydar and Khire 2007; Rich et al. 2008; Charles et al. 2009) in order to reduce the emission potential within a relatively short period of time. Recirculation of leachate and aeration leads to an enhanced degradation of organic matter and increased fixation of inorganic contaminants. A landfill with less emission potential requires less aftercare (Heimovaara et al. 2007, 2010; Heimovaara 2011). In order for regulators and landfill operators to agree on the required level of after care, a quantitative estimation of remaining long-term emission potential is required (Barlaz et al. 2002; Cossu et al. 2003; Cossu 2005, 2007; Vehlow et al. 2007; Butt et al. 2008; Heimovaara 2011).

Various mathematical models have been used in order to determine leachate quantity and quality during landfill operations or during the aftercare period (El-Fadel et al. 1997a). Based on landfill hydrology these models can be broadly classified into two major categories (1) continuum based models and (2) upscaled models. The continuum based models usually use lab determined or empirical material properties of waste material (Powrie and Beaven 1999; Kazimoglu et al. 2006) investigating spatial and temporal

characteristics of leachate (McDougall 2007; Gholamifard et al. 2008). The upscaled type of mathematical models are generally based on an input-output approach (Rosqvist and Destouni 2000; Rosqvist et al. 2005b), a stochastic transfer function approach (Zacharof and Butler 2004a,b), a dual porosity, a dual permeability (Bendz et al. 1998; Šimunek et al. 2003) or a stream tubes model approach (Matanga 1996).

Field measurements have shown a large variation in water content inside the waste bodies ranging from fully saturated conditions to complete dryness (Blight et al. 1992; Sormunen et al. 2008b). This is caused by the material properties of the refuse which can be highly water absorbent (e.g. sponge) or water repellent (e.g. oil, metal, plastic, glass) and range from impermeable to highly permeable (Powrie and Beaven 1999; Kazimoglu et al. 2006; Sormunen et al. 2008a). Daily cover layers, gas wells and areas with low and high mechanical compaction add additional heterogeneities and make flow in landfills non-uniform. This flow follows a complex pattern which can be explained as preferential pathways as shown in figure 3.1. Preferential flow in porous media is defined as an uneven movement of water through the porous media, characterized by enhanced flux regions participating in most of the flow through fraction of the channels (Hendrickx and Flury 2001; Nimmo 2005). In the case of landfills, preferential flow is considered to be the flow of water through a fraction of the total pore volume. Physical non-equilibrium in flow in an unsaturated heterogeneous porous medium is an important characteristic of preferential flow (Jarvis 1998). During non-equilibrium the water through the preferential pathways does not equilibrate with slowly moving resident water in bulk matrix (Jarvis 1998; Skopp 1981).

In this research, we explore the origin of preferential flow in small scale porous systems using a two dimensional (2D) coupled flow and transport deterministic model. In this numerical model, flow is represented by Richards' equation (RE) (Celia et al. 1990a) and transport by advection dispersion equation (ADE) (Bear 1988; Fetter 1993). This flow and transport coupled model is formulated in MATLAB (MATLAB 2014b) as Variably Saturated Flow and Transport (VarSatFT) toolbox. Using VarSatFT, we simulate three different spatially heterogeneous systems and compare their results with a homogeneous one. We consider different types of soils with known van Genuchten properties (van Genuchten 1980), located systematically in domains of small scale porous systems. These domains are applied with water infiltration in continuous and intermittent patterns of varying rates. The hypothesis is that heterogeneity, infiltration patterns and infiltration rates acts as factors responsible for the origin of preferential flow and non-equilibrium in transport.

The theory for flow and transport in porous media is given section 3.2. Section 3.3 contains model description, material parameters and describes different conditions applied on small scale systems. Section 3.4 reports and explains the effect of material het-

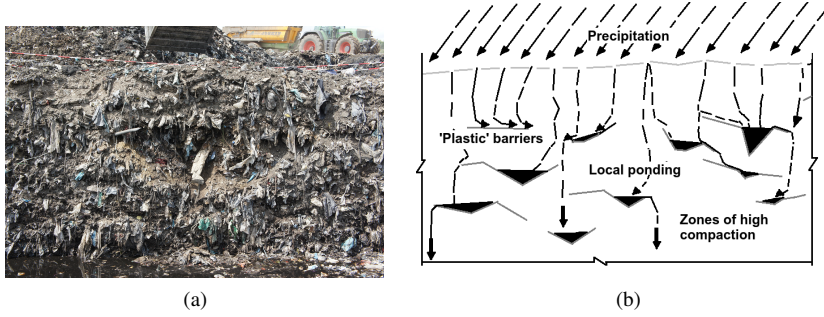


Figure 3.1: Sectional view showing heterogeneous nature of excavated pilot scale landfill located at Landgraaf, Netherlands (a) and simplified overview of flow inside a landfill (Inspired from figures shown in Baviskar and Heimovaara 2011; Mesu 1982)(b).

erogeneity, infiltration patterns and rates in small scale systems. This section also explains controlling factors affecting emission potential, feasibility of single continuum modelling method and suitable models for full scale landfill. Section 3.5 contains concluding remarks.

3.2 Theory

3.2.1 Water Flow

The mass balance equation of fluid flow through porous media can be written as in equation (3.1)(Pinder and Celia 2006).

$$\frac{\partial \rho_w \epsilon S_{eff}}{\partial t} + \nabla \cdot \rho_w \mathbf{q} = \rho_w Q_w \quad (3.1)$$

where

$$\mathbf{q} = -k_r(\psi) \mathbf{K}_{sat} [\nabla(\psi + z)] \quad (3.2)$$

In which ρ_w is the density of the fluid $[M/L^3]$, ϵ is the porosity of the medium $[L^3/L^3]$, S_{eff} is the effective saturation of the medium, \mathbf{q} is the Darcy velocity $[M/L]$, Q_w is the flow source/sink term $[L^3/L^3T]$, t is the time $[T]$, ψ is the pressure head $[L]$. k_r is relative hydraulic permeability function and \mathbf{K}_{sat} is the saturated hydraulic conductivity tensor $[L/T]$, for 2D written as $\begin{bmatrix} K_{xx} & K_{xz} \\ K_{zx} & K_{zz} \end{bmatrix}$, where x is horizontal direction and z is the vertical dimension assumed negatively downwards (by assigning $z = 0$ at top boundary).

An unsteady flow of water in incompressible variably saturated porous medium with no source or sink term can be derived from equation (3.1) and represented with the mixed-form of RE with Picard iteration process (Celia et al. 1990a) as

$$\frac{\theta^{a+1} - \theta^a}{dt} + \frac{C_m(\psi^{a+1,b}) + S_w S_s}{dt} \delta^{b+1} + \nabla \cdot \mathbf{q} = 0 \quad (3.3)$$

with

$$\psi^{a+1,b+1} = \delta^{b+1} + \psi^{a+1,b} \quad (3.4)$$

Equation (3.4) shows the Picard iteration process with a as the time level and b as the iteration stage and dt as time step. C_m is the $(\frac{d\theta}{d\psi})$ is differential water capacity $[1/L]$ in which θ is the water content as a function of ψ . S_w is the water saturation, expressed as $S_w = \frac{\theta}{\theta_s}$. S_s is the specific storage, which can be presented as $S_s = \rho_w g(\epsilon\beta + C_v)$, in which, g is acceleration due to gravity $[L/T^2]$, β is compressibility of water $[LT^2/M]$, C_v is coefficient of consolidation $[LT^2/M]$ and $\epsilon = \theta_s$ is porosity of the medium $[L^3/L^3]$.

The van Genuchten equation (van Genuchten 1980) for the effective saturation S_{eff} , which is needed to solve RE is

$$S_{eff} = [1 + (\alpha|\psi|)^n]^{-m} \quad (3.5)$$

where

$$S_{eff} = \frac{\theta(\psi) - \theta_r}{\theta_s - \theta_r} \quad (3.6)$$

where θ_r is residual water content $[L^3/L^3]$, θ_s is saturated water content $[L^3/L^3]$, S_{eff} is effective saturation [no dimensions], α is air entry value $[1/L]$, n and $m = 1 - 1/n$ are van Genuchten parameters for unsaturated flow. van Genuchten's equation (equation (3.5)) was used to obtain the relative permeability using Mualem's model (Mualem 1976).

$$k_r = S_{eff}^{\frac{1}{2}} \left[1 - \left(1 - S_{eff}^{\frac{1}{m}} \right)^m \right]^2 \quad (3.7)$$

so that the hydraulic conductivity can be calculated as

$$\mathbf{K}(\psi) = k_r \mathbf{K}_{sat} \quad (3.8)$$

The initial condition for RE can be expressed as

$$\psi(x, z, 0) = (z_{ref} - z) \quad (3.9)$$

where z_{ref} is water level in the domain $[L]$

The boundary conditions for RE can be expressed as a Neumann boundary condition on $S1$ (See equation (3.10)) and a Robbins boundary condition on $S2$ (See equation (3.11)). Where $S1 + S2 = S$ is the total boundary region.

$$\mathbf{q}(x, z, t) = q_{top} \quad (3.10)$$

$$\mathbf{q}(x, z, t) = K_{surf}(\psi_{amb} - \psi) \quad (3.11)$$

where q_{top} is the infiltration inflow rate $[L/T]$, K_{surf} is the surface permeability $[1/T]$ and ψ_{amb} is ambient pressure head $[L]$.

Surface ponding can occur when the infiltration is more than infiltration capacity i.e. $q_{top} > \mathbf{K}(\psi)$. The ponding can be approximated using infiltration formula (Green and Ampt 1911) of surface water balance as shown in equation (3.12).

$$\frac{d\psi_{pond}}{dt} = q_{top} - q_{IC} \quad (3.12)$$

where ψ_{pond} is ponding head at the infiltrating surface, q_{top} is the infiltration inflow rate occurring at the surface and $q_{IC} = \mathbf{K}(\psi)$ is the infiltration capacity of the infiltrating surface. During ponding conditions, the top Neumann boundary is switched into Dirichlet boundary condition with $\psi(x, z, t) = \psi_{pond}$ on $S1$, by solving equation (3.12).

3.2.2 Solute Transport

The mass balance of solute transport through a porous medium can be written as equation (3.13)(Bear 1988; Fetter 1993)

$$\frac{\partial \rho_w \epsilon S_w m_i}{\partial t} + \nabla \cdot \rho_w \mathbf{u}_i = \rho_w \epsilon S_w Q_{s_i} \quad (3.13)$$

where

$$\mathbf{u} = -\epsilon S_w \mathbf{D}_i \nabla m_i + \mathbf{q} m_i \quad (3.14)$$

In which Q_s is the solute source/sink term [L^3/L^3T], subscript i is the number of species, m is the mass fraction [M/M], t is the time [T], \mathbf{u} is concentration flux, \mathbf{q} is the advective velocity [L/T], \mathbf{D} is hydrodynamic dispersion tensor coefficient [L^2/T], for 2D it can be written as $\begin{bmatrix} D_{xx} & D_{xz} \\ D_{zx} & D_{zz} \end{bmatrix}$. The matrix elements of \mathbf{D} can be obtained using equation (3.15) (Pinder and Celia 2006) as

$$D_{\alpha\gamma} = \alpha_T |v| \delta_{\alpha\gamma} + (\alpha_L - \alpha_T) v_\alpha v_\gamma / |v| + D_m \delta_{\alpha\gamma} \quad (3.15)$$

where

$$v = \frac{\mathbf{q}}{\theta} \quad (3.16)$$

where $D_{\alpha\gamma}$ is the dispersion coefficient in respective directions, D_m is the molecular diffusion [L^2/T], v is the linear pore water velocity [L/T], α_L and α_T are the longitudinal and transverse dispersivities [L], respectively. The subscripts α and γ represent the x and z coordinate directions. Substitution of x and z for α and γ yields four values for the dispersion tensor. $\delta_{\alpha\gamma}$ is the Dirac delta function.

The approach for describing solute transport of a non sorbing, single component through a porous media with no source or sink term can be written as the ADE shown in equation (3.17).

$$\frac{\partial \theta c}{\partial t} - \nabla \cdot \mathbf{D} \theta \nabla c + \nabla \cdot \mathbf{q} c = 0 \quad (3.17)$$

where $c = \rho_w \cdot m$ and $\theta = \epsilon \cdot S_w$. c is concentration [M/L^3].

On further simplification we get equation (3.18).

$$\theta \frac{\partial c}{\partial t} + c \frac{\partial \theta}{\partial t} - \nabla \cdot \mathbf{D} \theta \nabla c + \mathbf{q} \nabla \cdot c + c \nabla \cdot \mathbf{q} = 0 \quad (3.18)$$

As we have coupled the transport equation with the flow equation, $c \frac{\partial \theta}{\partial t} = -c \nabla \cdot \mathbf{q}$. Thus, we can write equation (3.18) as equation (3.19).

$$\theta \frac{\partial c}{\partial t} - \nabla \cdot \mathbf{D} \theta \nabla c + \mathbf{q} \nabla \cdot c = 0 \quad (3.19)$$

where \mathbf{q} and θ are variables coupling the transport equation with the water flow equation, mathematically presented in equation (3.2) and equation (3.6).

The initial condition for the ADE can be expressed as

$$c(x, z, 0) = c_{ini} \quad (3.20)$$

where c_{ini} is initial concentration $[M/L^3]$

The boundary conditions can be expressed as a Dirichlet boundary condition on $S1$ (See equation 3.21) and a Robbins boundary condition on $S2$ (See equation 3.22). Where $S1 + S2 = S$ is the total boundary region.

$$c(x, z, t) = c_{top} \quad (3.21)$$

$$\mathbf{u}(x, z, t) = \mathbf{q} \nabla \cdot c \quad (3.22)$$

where c_{top} is concentration at the boundary condition $[M/L^3]$.

In the Eulerian-Lagrangian method, the Eulerian $\left(\frac{\partial c}{\partial t}\right)$ and Lagrangian $\left(\frac{Dc}{Dt}\right)$ time derivatives of concentration are related to each other through an advective transport term $(\mathbf{q} \nabla \cdot c)$ (See equation (3.23)) (Ewing and Wang 2001).

$$\frac{Dc}{Dt} = \theta \frac{\partial c}{\partial t} + \mathbf{q} \nabla \cdot c \quad (3.23)$$

The Lagrangian $\left(\frac{Dc}{Dt}\right)$ time derivative can be equated to the dispersion term as shown in equation (3.19). The dispersion term $(\nabla \cdot \mathbf{D} \theta \nabla c)$ is solved on Euler grid. Whereas the

advective term ($q\nabla \cdot c$) from the right hand side of equation (3.23) is solved by Lagrangian method (MIC method).

In Lagrangian method, the concentration c , and the x and z components of linear velocities \mathbf{v} are initially distributed on the dimensionless markers (Refer equation (3.16) for \mathbf{v})(Gerya and Yuen 2003). These Lagrangian markers are advected using equation (3.24).

$$\begin{aligned} x_{mrk}^{t+\Delta t} &= x_{mrk}^t + v_{x_{mrk}} \cdot \Delta t \\ z_{mrk}^{t+\Delta t} &= z_{mrk}^t + v_{z_{mrk}} \cdot \Delta t \end{aligned} \quad (3.24)$$

where x_{mrk}^t and z_{mrk}^t are the location of the markers in x and z direction at time t , and $x_{mrk}^{t+\Delta t}$ and $z_{mrk}^{t+\Delta t}$ are the location of the markers in x and z direction at time $t + \Delta t$. The $v_{x_{mrk}}$ and $v_{z_{mrk}}$ are the linear velocities of the markers. The change in distribution of the markers due to advection is utilized for interpolating the concentration from the markers to the surrounding nodes. This interpolation of concentration from nodes to markers and vice-versa is carried out at every time step.

3.3 Materials and Methods

3.3.1 VarSatFT simulator

The water flow was modelled using mixed-form of RE. The non-linearity of RE was solved using Picard iteration process (Celia et al. 1990a). The ADE for solute transport consisted of a non-sorbing single component species, which was solved using Eulerian - Lagrangian approach. In this approach the dispersion was solved on Euler nodes and the advection was solved on Lagrangian markers using modified marker-in-cell method (MIC) inspired by Gerya's (Gerya and Yuen 2003) MIC method (See Chapter 2 for modified MIC). The discretized form of flow and transport equations were implemented using finite difference method in VarSatFT toolbox, formulated in MATLAB. The VarSatFT simulator has been verified by simulating variety of flow and transport problems as described in Chapter 2. Its detailed formulation is also described in Chapter 2 and Appendix B.

3.3.2 Description of small scale systems

In this section we describe the spatial scenarios, the boundary conditions and the simulation procedure applied on the small scale systems. These small scale systems were build

of domain size $1.0\text{ m} \times 1.0\text{ m}$ dimensions. The domains were discretized into elements of size 0.05 m .

We have considered different spatial scenarios in small scale systems. We have named them as Gravelly sand and Plastic (GP); Gravelly sand Loam and Plastic (GLP); Five Materials (FM) ¹. Their simulation results were compared with a Homogeneous (H) scenario domain system. Detailed diagrams of these different spatial scenarios are shown in figure 3.2. The material properties considered for different soil profiles are indicated in Table 3.1. These properties were referred from Schafer 2001 and Thoma et al. 2013.

The initial and boundary conditions applied on the small scale systems for flow and transport related to our study is listed in Table 3.3. For water flow, the initial condition was a highly unsaturated. The Neumann boundary condition was implemented at the top edge, where q_{top} is infiltration applied with different rates in continuous (CI), square wave (SI) and rectangular wave patterns (R1I and R2I) (See figure 3.3 (a) and Table 3.2). The infiltration in rectangular wave pattern was of two types with different no-flow pulse width for its time period. The Robbins boundary condition was applied at the bottom edge, where K_{surf} is the surface permeability and ψ_{amb} is the ambient pressure head. For impermeable plastics in some of the spatial scenarios, we assume that $K = 0\text{ m s}^{-1}$ at the required inter-nodes.

For solute transport, the initial concentration was considered to be uniformly distributed throughout the domain of system. A Dirichlet boundary condition was applied to the top edge, and a Robbins boundary condition of zero concentration gradient was applied at the bottom edge. The left and right edges were defined to be impermeable for the flow and transport. The values for the initial, boundary conditions and other parameters are listed in Table 3.4.

In this study, we generated results for 48 different scenarios (4 spatial scenarios; each spatial scenario applied with 4 different types of infiltration patterns; each pattern has 3 different types of infiltration rates). The cumulative of infiltrations are shown in figure 3.3(b). All these systems were simulated for a time range of 5 days with the temporal discretization of 100 s . The implications of heterogeneities, infiltration rates and patterns on spatial distributions of flow and transport are investigated through these small scale systems.

3.4 Results and Discussion

In this section we analyse how heterogeneity and infiltration patterns and rates affect the flow and transport in small scale systems. We only consider a few of the spatial scenarios and generic boundary conditions as described in section 3.3.2.

¹Note: The abbreviations used in this chapter are shown in Table 3.2

Table 3.1: Material properties for soil profiles used in different small scale systems were considered from Schafer 2001 and Thoma et al. 2013.

Material pa- rameters	Gravelly sand	Loam	Sandy clay loam	Sandy loam	Sandy clay
α [m^{-1}]	8.5	1.1117	2.1086	2.6669	3.342
n	2.567	1.4723	1.3305	1.4488	1.2078
θ_r [$\text{m}^3 \text{m}^{-3}$]	0.04	0.061	0.063	0.039	0.1721
θ_s [$\text{m}^3 \text{m}^{-3}$]	0.349	0.399	0.384	0.387	0.385
\mathbf{K}_{sat} [m s^{-1}] in xx and zz direction	1.33×10^{-3}	1.3947×10^{-6}	1.5258×10^{-6}	4.4308×10^{-6}	1.3137×10^{-6}

Table 3.2: Abbreviations for different spatial and infiltration scenarios used in this chapter.

Abbreviation	Lengthen
H	Homogeneous
GP	Gravelly sand and plastic
GLP	Gravel sand, loam and plastic
FM	Five materials
CI	Continuous infiltration
SI	Square wave pattern infiltration of equal offset and inset flow condition of 300 s in its time period
R1I	Rectangular wave pattern infiltration with offset flow condition (600 s) two times the inset flow condition (300 s) in its time period
R2I	Rectangular wave pattern infiltration with offset flow condition (1200 s) four times the inset flow condition (300 second) in its time period

Table 3.3: Initial and Boundary conditions used in simulations.

Flow and Solute model	Initial Conditions	Boundary Conditions	
		Top edge	Bottom edge
Water flow	$\psi(x, z, 0) = (z_{ref} - z)$	$\mathbf{q}(x, 0, t) = q_{top}$	$\mathbf{q}(x, -1, t) = K_{surf}(\psi_{amb} - \psi)$
Solute transport	$c(x, z, 0) = c_{ini}$	$c(x, 0, t) = c_{top}$	$\mathbf{u}(x, -1, t) = \mathbf{q}c$

Table 3.4: Assumed parameters used in simulations.

Parameters	Assumed values
z_{ref} [m]	-2.00
q_{top} [m s ⁻¹]	$-1.00 \times 10^{-4}, -1.20 \times 10^{-4}, -1.4 \times 10^{-4}$
K_{surf} [s ⁻¹]	1.33×10^{-3}
ψ_{amb} [m]	-1.00
β [m s ² kg ⁻¹]	4.00×10^{-10}
C_v [m s ² kg ⁻¹]	0
c_{ini} [kg m ⁻³]	1.00
c_{top} [kg m ⁻³]	0
D_m [m ² s ⁻¹]	1.00×10^{-10}
α_L [m]	0.10
α_T [m]	0.01

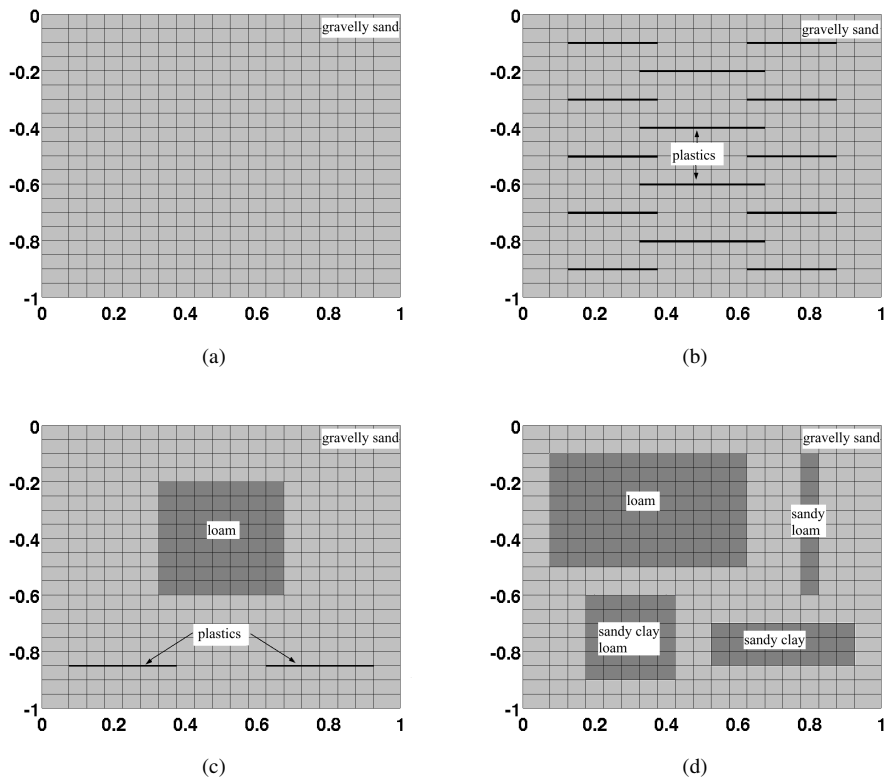
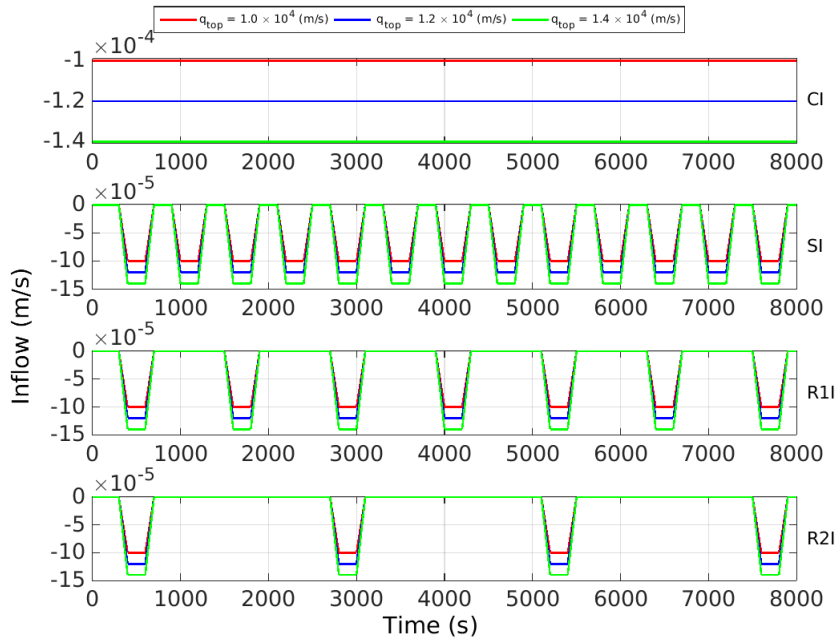
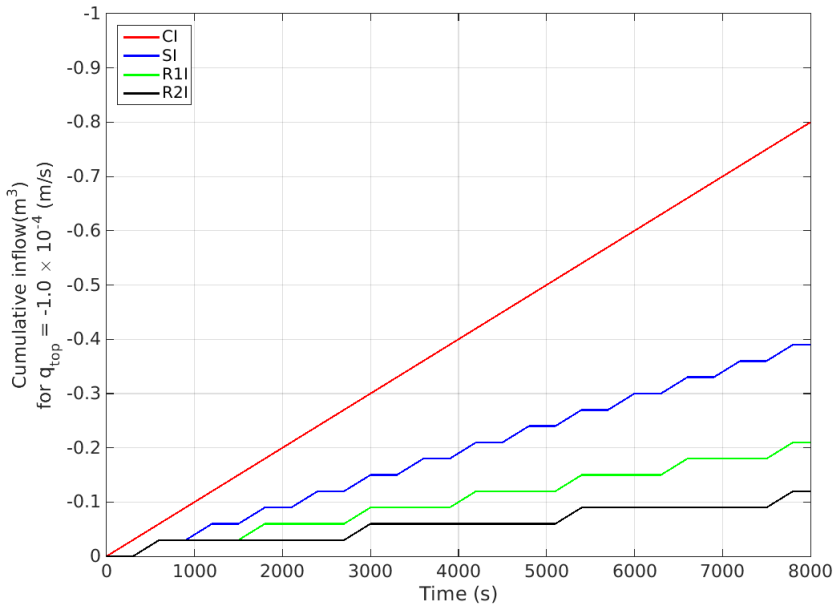


Figure 3.2: Spatial scenarios: H(a); GP (b); GLP (c) and FM (d).



(a)



(b)

Figure 3.3: Infiltration scenarios: Infiltration patterns and rates applied (a). Cumulative of infiltrations for $1.0 \times 10^{-4} \text{ m s}^{-1}$ rate of all infiltration patterns (b).

3.4.1 Distributions of flow and transport observed in spatial distributions

The results of spatial distribution of the pressure head, water content and solute concentration are illustrated in this section. The flow and transport in the homogeneous system (H) are only in vertically downward directions. Flow and transport in the gravel-plastic system (GP) flow along longer flow paths following the orientation of the plastics. In the other systems with a mixture of more materials (GLP and FM), the presence of plastics and soils with low and high permeabilities cause horizontal flow along the plastics and low permeable fine soil materials. In addition the solute will only slowly leach from the fine soil materials with lower permeabilities due to a significantly reduce advective transport component. This contributes to a lower rate of decrease in solute concentration levels (Das et al. 2004).

We show simulation results for all spatial scenarios (FM, GPL, GP and H) with a infiltration rate of $-1.00 \times 10^{-4} \text{ m s}^{-1}$ and a pattern R2I. They were observed at the end of 12 h of total simulation time where 0.54 m^3 was the cumulative amount of water infiltrated.

The results for the H spatial scenario are shown in figure 3.4. The pressure head contours are horizontal and have decreasing values along the depth of domain. This indicates that the flow is only due to vertical pressure gradients (figure 3.4(a),(b),(c)). The solute concentrations are completely flushed at 2.95 pore volumes at the observed time (figure 3.4(c)).

In figure 3.5 the results for the GP spatial scenario show a significant variation in pressure head and water contents near the plastic layers. Increased water content above, and lower values below (figure 3.5(a),(b)). Vertical flow is inhibited at the position of the plastic leading to the development of perched water table. These local perched water tables induce horizontal pressure gradients causing horizontal flow along the periphery of plastics (figure 3.5(a),(b),(c)). Three main types of streamlines can be discerned in the GP scenario. The first is in the middle of the model domain and are the longest streamlines flowing along the plastic sheets in an oscillatory fashion. The second can be found near the left and right edges of the domain and are the shortest in length as they are not influenced by the presence of the plastic. Finally the third type are streamlines which fall between these two extremes. The figure with solute concentrations clearly indicates the shadow effect caused by the diversion of water by the presence of plastics (figure 3.5(c)). Even after flushing 2.36 number of pore volumes some salt remains present at the bottom of the domain.

The contours and streamlines in the GLP scenario shown in figure 3.6 illustrated the presence of perched water tables on top of the fine loam block and plastics caused by the lower hydraulic conductivities compared to the background gravelly sand material (figure

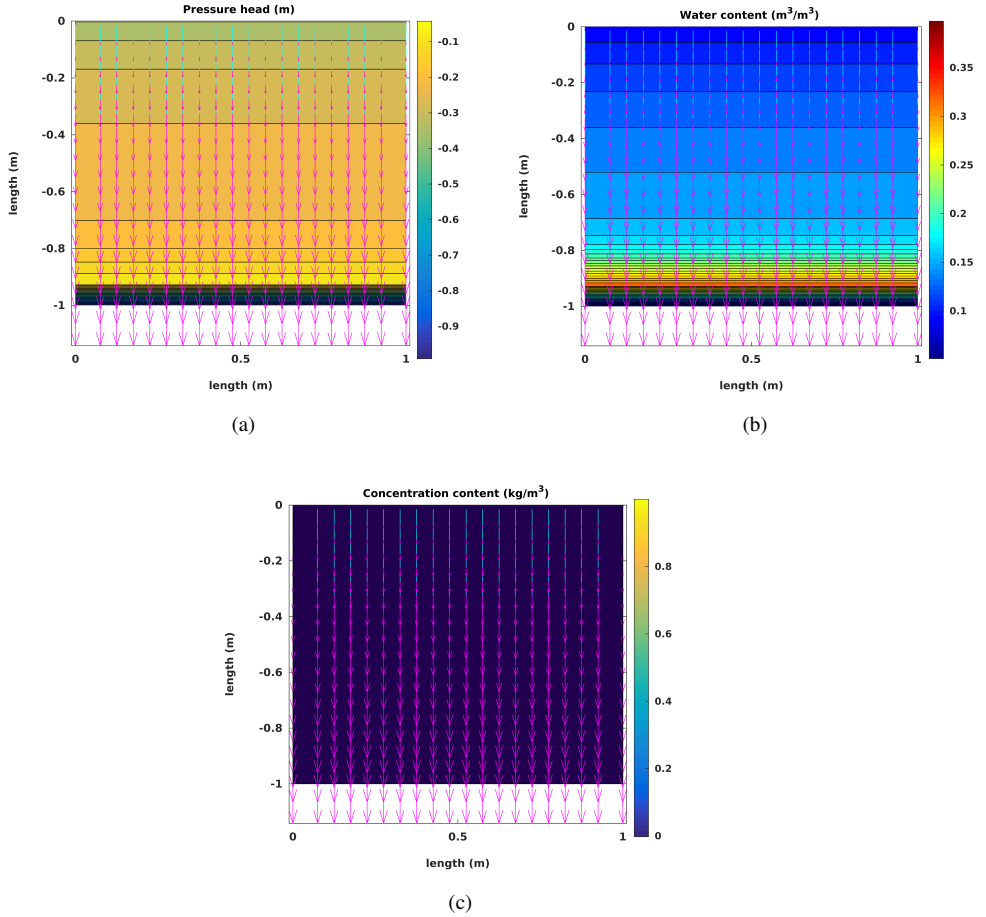


Figure 3.4: Distribution of pressure head (a) water content (b) and solute concentration (c) for the H spatial scenario subjected to an infiltration rate of $-1.00 \times 10^{-4} \text{ m s}^{-1}$ with the R2I inflow pattern. Results are shown after 12 h of the total simulation time.

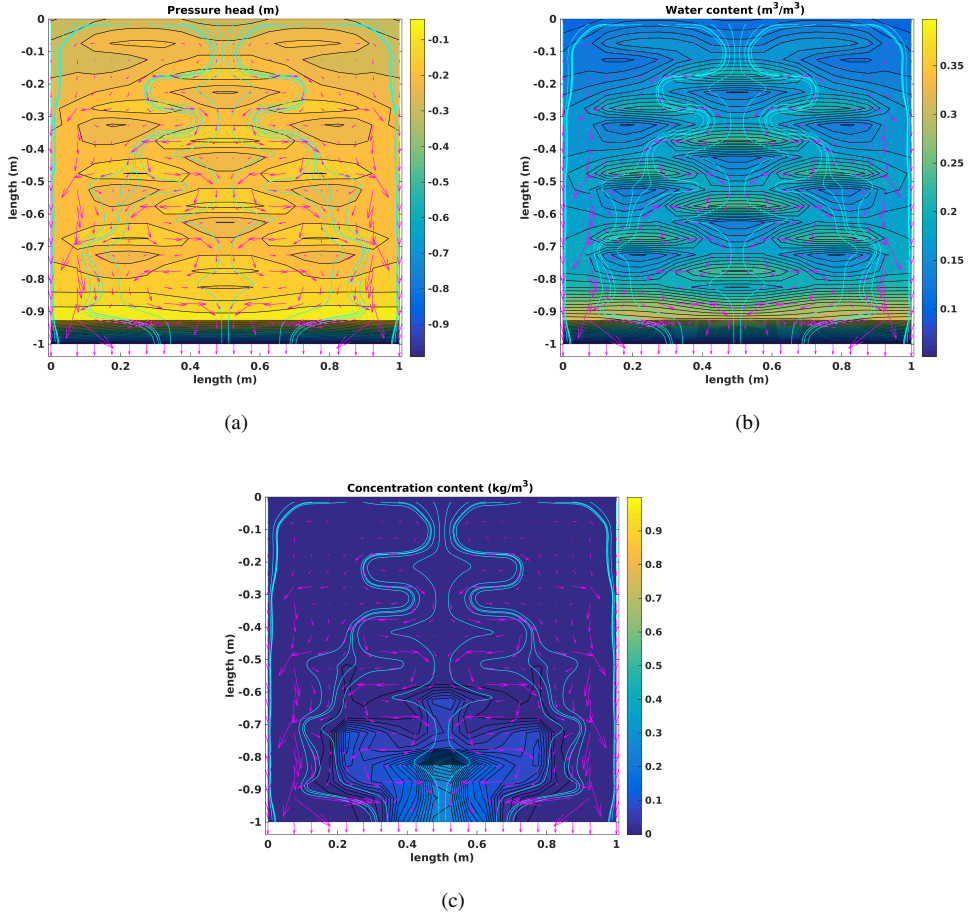


Figure 3.5: Distribution of pressure head (a) water content (b) and solute concentration (c) for the GP spatial scenario subjected to an infiltration rate of $-1.00 \times 10^{-4} \text{ m s}^{-1}$ with the R2I inflow pattern. Results are shown after 12 h of the total simulation time.

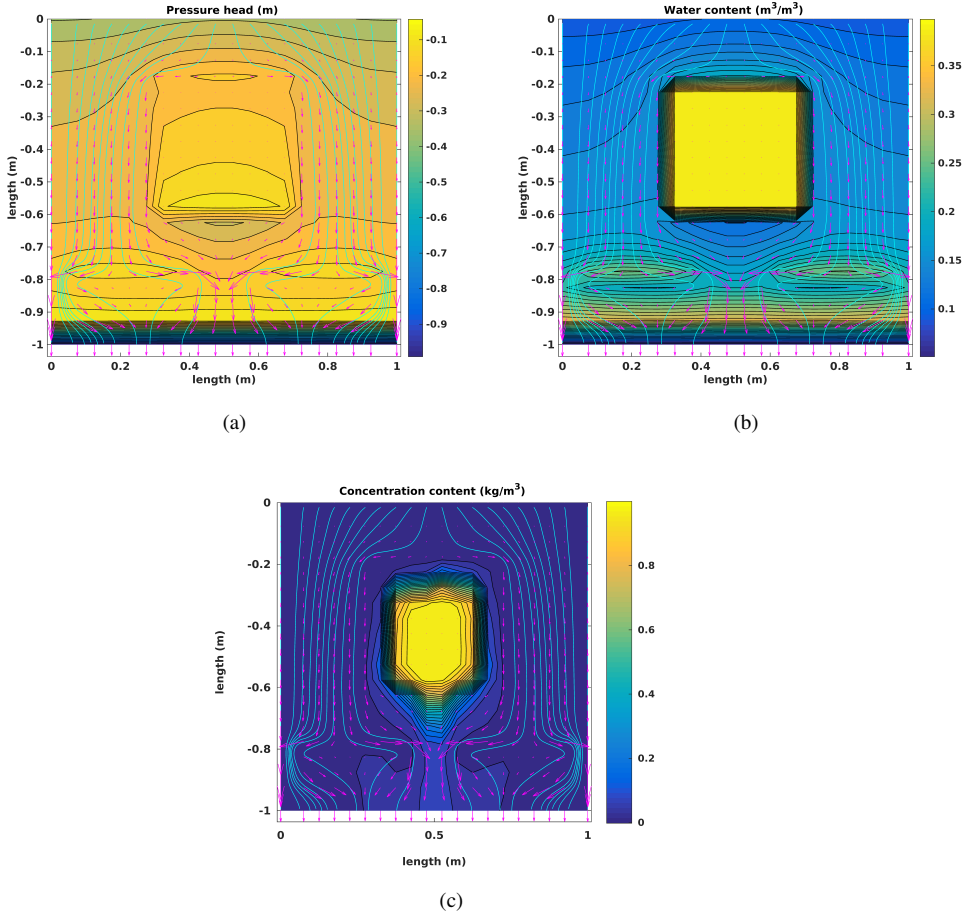


Figure 3.6: Distribution of pressure head (a) water content (b) and solute concentration (c) for the GLP spatial scenario subjected to an infiltration rate of $-1.00 \times 10^{-4} \text{ m s}^{-1}$ with the R2I inflow pattern. Results are shown after 12 h of the total simulation time.

3.6(a),(b)). The perched water tables induce horizontal pressure gradients in time causing flow directed along the periphery of the loam block and plastics (figure 3.6(a),(b),(c)). The low saturation of the gravelly sand below the loam block, leads to lower relative permeabilities. Capillary suction retains the water in the block of loam (figure 3.6(b)). No advective solute transport can take place in the block of loam, only diffusion can occur, driven by the gradients in concentration near the edges of the block of loam (figure 3.6(c)). Clearly extreme differences in material properties cause an incomplete flushing of the solute concentrations from the loam block at the observed time even though 2.19 pore volumes have been flushed.

The results of the FM-scenario show a combination of the effects found in the previous scenarios (See figure 3.7). Perched water tables develop on top of the fine soil blocks (loam, sandy clay loam, sandy loam, sandy clay) because of the difference in hydraulic conductivity (figure 3.7(a),(b)). The perched water tables induce horizontal pressure gradients which vary in time. As a result flow is directed along the periphery of these fine material blocks (figure 3.7(a),(b),(c)). Due to the reduced advective transport in these fine material blocks, solutes are retained because diffusion is a slow process (figure 3.7(c)). Thus solute concentrations are retained in the domain at 1.73 flushed pore volumes at the observed time.

The results observed in figures 3.4, 3.5, 3.6 and 3.7 clearly show that the presence of plastics and fine soil blocks leads to emergence of horizontal flow. The anisotropic nature of permeabilities in heterogeneous scenarios lead for a development of horizontal pressure gradients. More horizontal pressure gradients are observed for the scenario with higher heterogeneities (FM>GLP>GP). Retention time of solutes depends on the length of the stream lines which tends to increase when the heterogeneity in the domain increases. Presence of impermeable layers also leads to a focussing of streamlines with depth in unsaturated systems. This focussing causes shadow zones below impermeable layers which will retain solutes as they are not flushed. Materials with low hydraulic conductivity values can retain solutes for a long time as the only leaching process is diffusion. The larger the size of such blocks of materials, the longer solutes will be retained. This leads to formation of the immobile and mobile regions, where immobile regions retain solutes much longer than mobile regions. Therefore increased heterogeneity leads to an increased variation in lengths of streamlines and therefore an increased variation in travel times for water moving through the domain. At the macroscopic level, the lowest travel times can be considered to be flowing through preferential flow paths (Kohler et al. 2001; Šimunek et al. 2003; Šimunek and van Genuchten 2008). However, one should realize that there can be a very wide distribution of travel times. In principle two dominant mechanisms can be identified: 1) increased travel time due to increased streamlines and 2) long retention of salts due to presence of materials with low hydraulic conductivity.

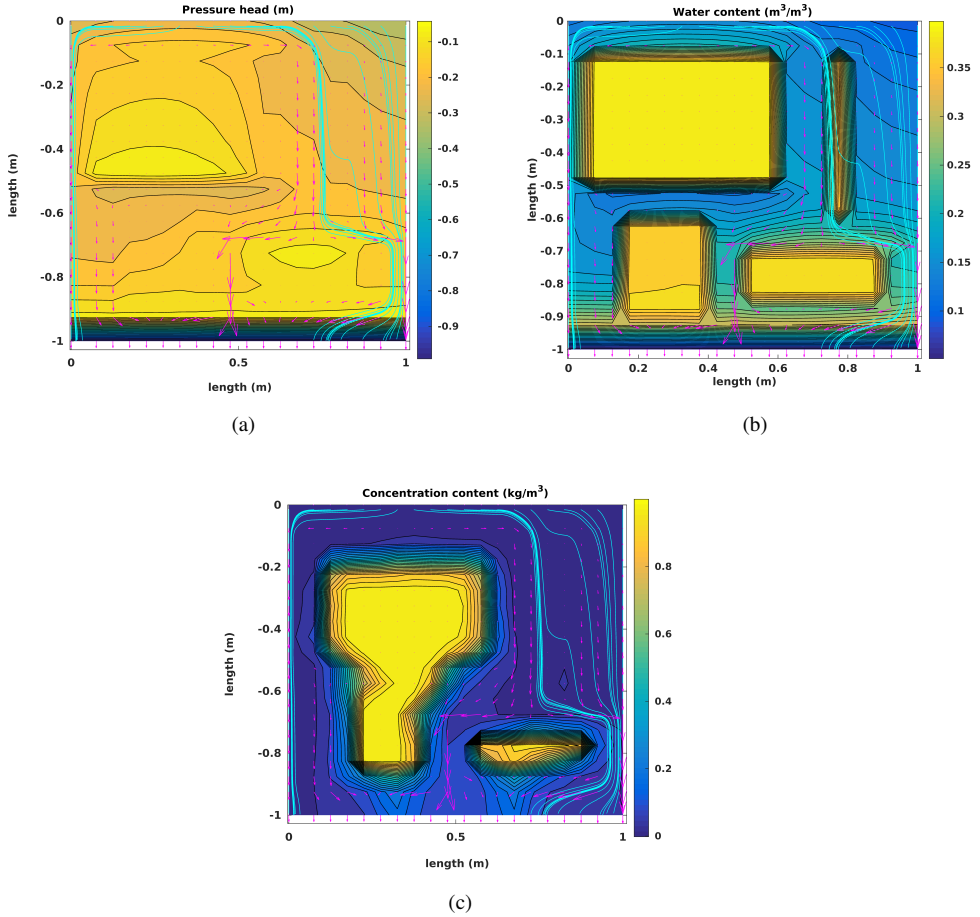


Figure 3.7: Distribution of pressure head (a) water content (b) and solute concentration (c) for the FM spatial scenario subjected to an infiltration rate of $-1.00 \times 10^{-4} \text{ m s}^{-1}$ with the R2I inflow pattern. Results are shown after 12 h of the total simulation time.

3.4.2 Average total drainage relationships

The simulation results allow us to calculate total drainage relationships for the complete model domain for the different scenarios. Here we show the normalized average solute concentrations and average solute masses obtained in the discharged leachate as a function of the number of flushed pore volumes.

3.4.2.1 Effect of heterogeneity on flow and transport

The results shown in figure 3.8(a) illustrated the impact heterogeneities have on the leachate. The solute breakthrough for scenarios GP, GLP and FM reflect the intermittent infiltration pattern R2I. The variation in solute concentration in the breakthrough curves (BTCs) is caused by the timing between flow and no-flow during the simulation. Solute concentrations only increase only in the heterogeneous scenarios (in order of FM>GCP>GP) and not for homogeneous (H) scenario. The increase is caused by local diffusion of solute from the relative immobile pore water to the mobile pore water during stagnant flow conditions. When flow starts again, the solute leaches with the mobile water.

In addition we also observe an early break through of solute for the different heterogeneous scenarios (in order of FM followed by GP and then by GLP). The break through for scenario H is obtained at 1 pore volume. Relatively longer streamlines causes a broader break through curve for scenario GP as compared to other heterogeneous scenarios and homogeneous scenario. Scenarios GLP and FM requires more than 1 pore volume for complete drainage of solute because slow diffusion from the immobile to mobile pore water. The tailing of solute for scenario FM is longest as compared to that observed in GCP, GP and H.

The difference in pore volumes required to drained the solute can be partly be explained by the differences in porosity distributions (Lunati et al. 2003). The porosity in heterogeneous scenarios is in order of FM>GLP>GP. However, more important is the fact that differences in hydraulic conductivity prevent water from flowing through a significant part of the domain. Diffusion instead of advection leads to the long tailing and therefore, the large number of pore volumes required to leach the solute.

3.4.2.2 Effect of infiltration pattern on flow and transport

Figure 3.9 shows the effect of varying the infiltration patterns where we move from continuous infiltration to more and more heterogeneous infiltration (CI, SI, R1I, and R2I). For the H-scenario, it appears that solute breakthrough occurs earlier with the CI and SI infiltration patterns compared to those observed with the R1I and R2I infiltration patterns. The difference between these scenarios is that the variation in water content throughout

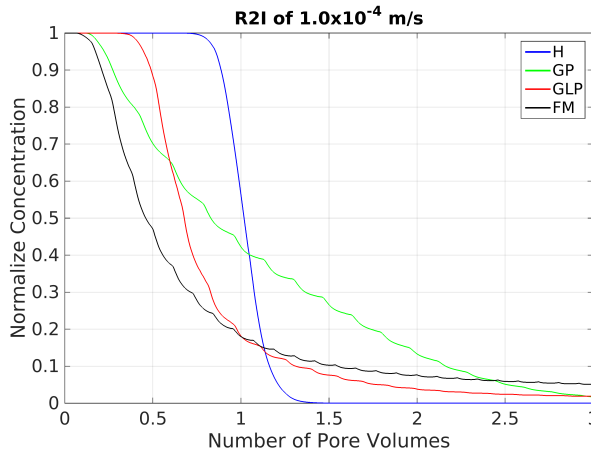


Figure 3.8: Effect of Heterogeneity: normalized average solute concentration against number of pore volumes obtained for all scenarios applied with R2I infiltration pattern with $-1.0 \times 10^{-4} \text{ m s}^{-1}$ infiltration rate.

time is larger for the R2I and R1I scenarios because the water drains in the conditions with no flow. This result is physically not realistic as it should disappear when expressing the leached solute as a function of pore volume. Therefore this result indicates an error in the implementation of the model. The linearisation during finite discretization in time leads to this error.

For the GP-scenario, solute tailing is significantly longer for the R2I infiltration pattern than observed for R1I, SI and CI. The breakthrough curve breaks in four parts (See figure 3.9(b)), the first three parts indicates the three types of streamlines classified with respect to their lengths and the last part indicates the diffusion process. For the GLP-scenario, all results for infiltration patterns (CI, SI and R1I) are similar, only infiltration pattern R2I differs. For the FM-scenario, a longer tailing is observed for the R2I pattern compared to R1I, SI and CI.

The continuous infiltration for the CI-pattern leads to a steady state water content in the domain. The time of the no-flow conditions in the SI-pattern is apparently so-small that no significant drainage could occur. In a dry column, water can be stored in the pore-space before drainage occurs, the temporal variation in storage is largest in scenario R2I. In a heterogeneous porous system where concentration gradients are present, increased storage during infiltration will lead to relatively more time for solute exchange to take place before water is discharged from the system as leachate. This will cause larger variations in leachate concentration. The slow exchange implies a non-equilibrium between the solute concentrations in the immobile and mobile pore water.

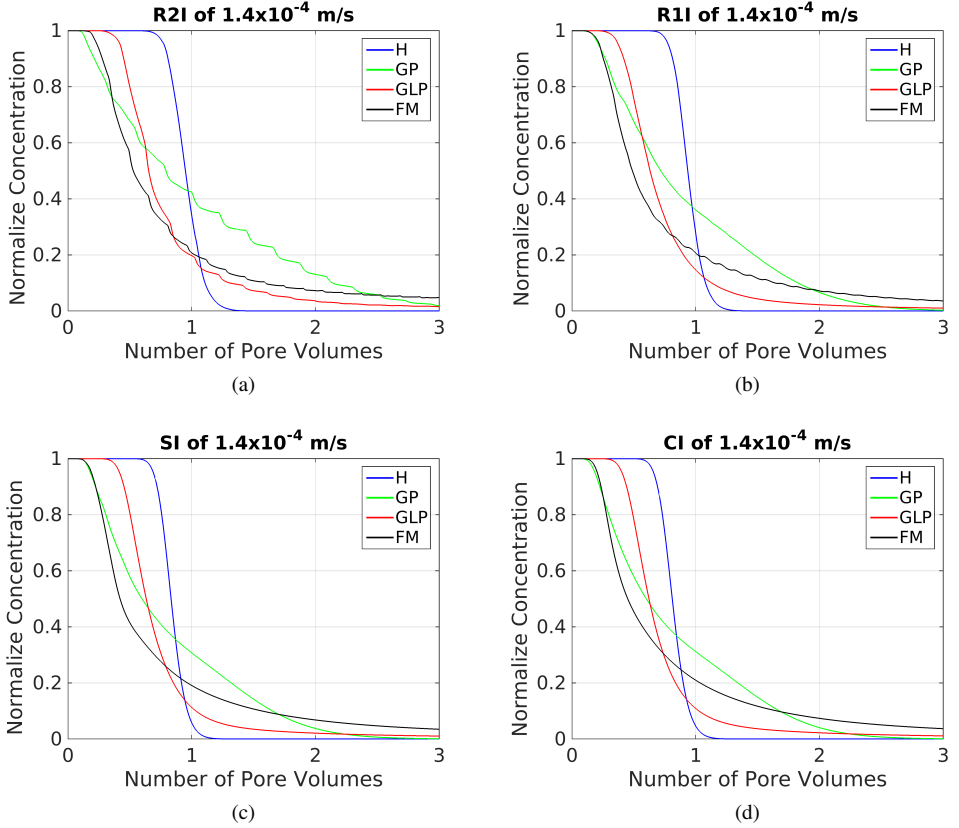


Figure 3.9: Effect of Infiltration pattern: Normalize average solute concentrations plotted against number of pore volumes obtained from drainage for all spatial scenarios (H, GP, GLP and FM) applied with different types of infiltration patterns (R2I, R1I, SI and CI) with $-1.4 \times 10^{-4} \text{ m s}^{-1}$ infiltration rate.

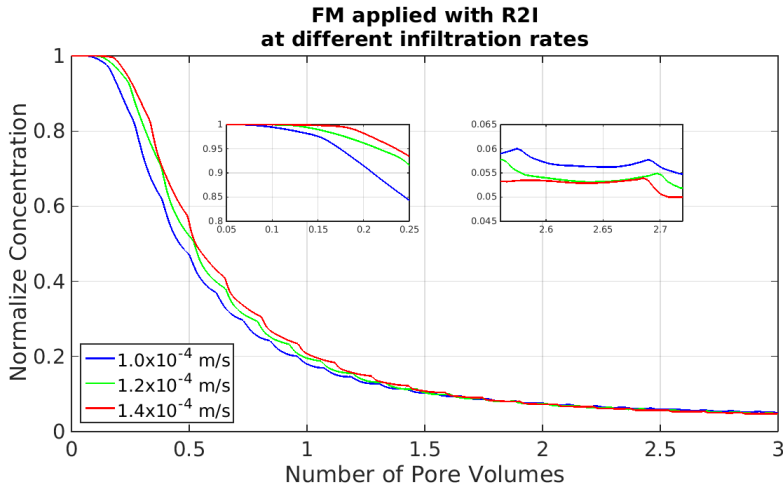


Figure 3.10: Effect of Infiltration rates: normalized average solute concentration against number of pore volumes obtained for FM scenario applied with R2I infiltration pattern with $-1.0 \times 10^{-4} \text{ m s}^{-1}$, $-1.2 \times 10^{-4} \text{ m s}^{-1}$ and $-1.4 \times 10^{-4} \text{ m s}^{-1}$ infiltration rates.

3.4.2.3 Effect of infiltration rates on flow and transport

Figure 3.10 shows breakthrough curves for the FM-scenario with the R2I infiltration pattern subjected to all three infiltration rates $-1.0 \times 10^{-4} \text{ m s}^{-1}$, $-1.2 \times 10^{-4} \text{ m s}^{-1}$ and $-1.4 \times 10^{-4} \text{ m s}^{-1}$. The enlarged plots show details of the early drainage and long tailing for the three different infiltration rates. It is clear that slow diffusion from the immobile water leads to a rise in concentration of the mobile water. The differences between the three infiltration rates is caused by a larger dilution in the mobile water for the highest flow rate, the residence time of the mobile water during flushing is shorter. As a consequence, the mobile water flushes faster in the high flow rated condition. However, the large volume of immobile water dominates the tailing. Presence of non-equilibrium exchange in a system with variation in infiltration regime has a significant impact on the dynamics in the leachate concentrations. Decreasing amounts of mobile pore water lead to larger variations in leachate concentrations.

3.4.2.4 Factors controlling emission potential

The normalized cumulative mass in the leachate as a function of flushed pore volumes is shown in figure 3.11. The outflow mass is normalized to the initial amount of solute present in the model domain. As expected, complete flushing occurs for the H-scenario after about 1 pore volume. The variation in travel times in the GP-scenario and the development of shadow zones requires significantly more water to be infiltrated to achieve

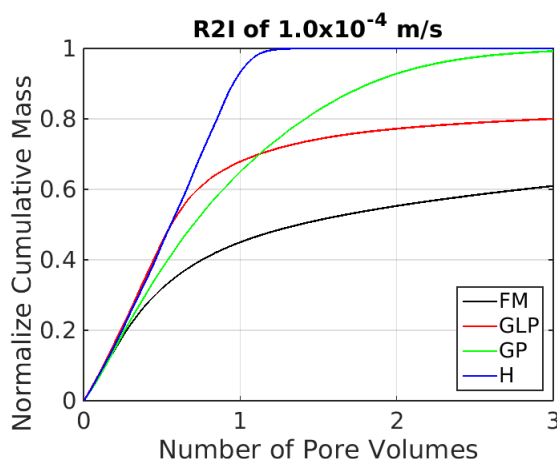


Figure 3.11: Normalize cumulative average solute mass against number of pore volumes obtained from drainage for all scenarios for R2I infiltration pattern of $-1.00 \times 10^{-4} \text{ m s}^{-1}$ rate.

complete flushing. The presence of zones with low hydraulic conductivity in the GLP and FM scenarios prevent complete flushing. The mobile zone flush quickly, slow diffusion causes a long tailing.

Bun et al. (2013) proposed that the solute mass in the waste body at a certain point time should be considered to be the emission potential of a full scale landfill. The simulations on small scale systems discussed in this section 3.4.2.2 and 3.4.2.3 show that high rates with the CI-pattern removes solute most effectively because of maintaining the largest gradients in concentration between the mobile and immobile water. In full scale landfills where rainfall is in general intermittent, it takes more than 10 years to obtain a drainage of 1 pore volume ². Increasing infiltration in a relatively continuous mode in order to increase the cumulative amount of water infiltrating would increase the reduction of emission potential of a landfill. However the tailing effect is difficult to address. After flushing the mobile pore volume, concentrations in the leachate are dominated by the ratio between the mobile and immobile pore volumes.

In full scale landfills, the volume of preferential pathways responsible for draining 95% of the infiltrating water can be only 0.2% of the total volume (Fellner and Brunner 2010) and leachate concentrations are highly correlated with discharge rate.

²Let us assume the dry density of MSW is 1200 kg m^{-3} and its porosity is 0.6. Suppose the depth of landfill is 15 m. Average precipitation in Netherlands is 300 mm per year. Then the calculated pore volume is 9 m and the liquid solid ratio (L/S) is 0.0167 l kg^{-1} for a year. It will require 30 years to achieve 1 pore volume and therefore 0.5 L/S ratio to achieve 1 pore volume.

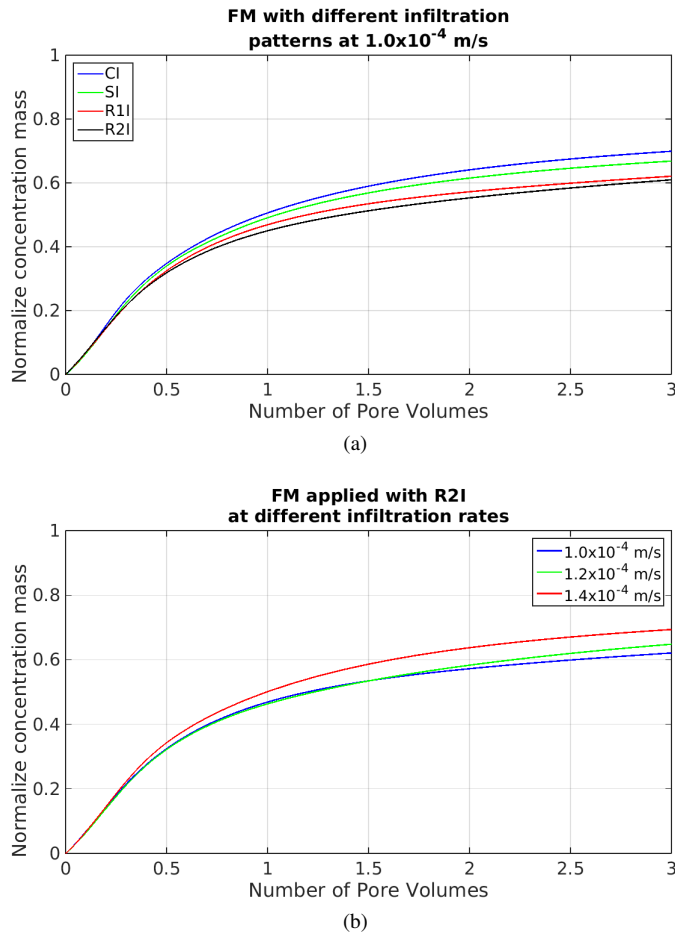


Figure 3.12: Normalize cumulative average solute mass against number of pore volumes obtained from drainage for scenario FM with different infiltration patterns (a) and rates (b).

3.4.3 Feasibility of single continuum modelling method for MSW landfill

Richards' equation has often been used for modelling the production of leachate from landfills (McDougall 2007; Gholamifard et al. 2008). This common modelling approach is based on assumptions of homogeneity of the landfill media (Ahmed et al. 1992; Demetrapoulus et al. 1986; Vincent et al. 1991). In full scale landfill the heterogeneity scale may vary from the size of a gravel to a large plastic sheet and may change in time. In this chapter we show that preferential flow exists even for a small scale heterogeneous systems (See figure 3.8). So it is very likely that preferential flow occurs within the representative elementary volume (REV) of 1 cubic meter, used in continuum models by McDougall (2007) and Gholamifard et al. (2008). As a consequence the results obtained using such single continuum models for a full scale landfill do not match field observations (Ugoccioni and Zeiss 1997; Rosqvist and Destouni 2000; Rosqvist et al. 2005b). Preferential flow in MSW landfill occurs only through 0.2-10% of the volume of landfill (Ugoccioni and Zeiss 1997; Fellner et al. 2009).

In addition, in closed landfills the location of the different waste materials is not known. There is a large variation in the material properties of waste and therefore varying chemical composition (El-Fadel et al. 1997a; Ziyang et al. 2009). Material properties of waste inside landfill cannot be quantified. Therefore the single continuum deterministic modelling approach for full scale landfill becomes unrealistic (Bun et al. 2013).

3.4.4 Suitable modelling methods for MSW landfill

In modern landfills, the easily available parameters obtained during landfill monitoring are the infiltration rate (i.e rainfall or irrigation inflow rate), the outflow discharge and the electrical conductivity of the leachate obtained from the drainage layer (van Vossen and Heyer 2009b,a). Jury and Stolzy (1982); Jury (1982); Jury and Roth (1990) has shown how these types of inlet and outlet parameters could be related together and utilized as an modelling approach for flow and transport in the vadose soil zone. Similarly Zacharof and Butler (2004a,b) relates these input output parameters to model landfill leachate quality and quality. Therefore it seems that models which take the preferential flow and non-equilibrium in transport into account is better than the single continuum based models.

The drainage relations obtained in section (3.4.2.1) can be described using non-equilibrium models. For instance the drainage relationships for GLP and FM scenarios can be modelled using a dual or a multi-permeability model (Bendz et al. 1998; Šimunek et al. 2003). In the GP scenario, the non-equilibrium emerges due to varying length of streamlines so we could use a stream tube model to model this behaviour (Matanga 1996).

In figure 3.13 we plot outflow mass and discharge along number of pore volumes for

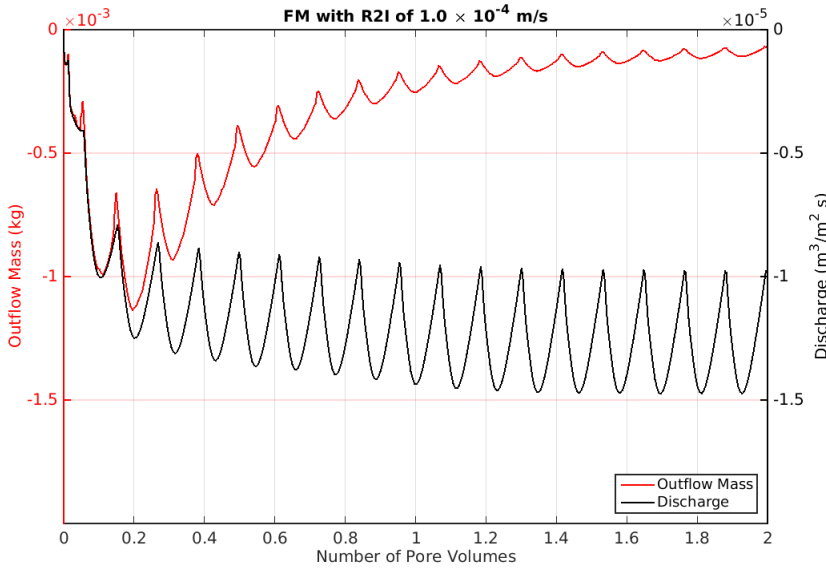


Figure 3.13: Outlet solute mass along against number of pore volumes obtained at drainage for heterogeneous scenario FM for $-1.0 \times 10^{-4} \text{ m s}^{-1}$ rate and R2I pattern.

FM scenario for R2I infiltration with $1.0 \times 10^{-4} \text{ m s}^{-1}$ rate. For same number of pore volumes, an increase in outlet solute mass corresponds to an increase in discharge rate (See, the BTC of solute mass and discharge, along same vertical grid lines). This is observed until all the mass is drained out from the domain. The negative sign for the solute mass suggests draining in downward direction. Using this relation the type and rate of infiltration can be designed to optimize the required emission potential of a landfill. However this type of correlation between the solute concentrations or EC measurements and the discharge outflow is observed only for intermittent patterns of infiltration or for rainfall precipitations. This relationship can be used to determine the probability distribution of the solute transport time. The transfer function approach by Jury and Roth (1990) can be utilized to determine the emission potential of full scale landfill.

3.5 Conclusions

In this chapter we show that introducing spatial heterogeneities in small scale systems can lead to preferential pathways and, therefore, emergence of non-equilibrium behaviour in solute transport. It is highly probable that the spatial distribution of pressure head, water content and solute concentration observed in this study is similar to locations present in existing landfills. The heterogeneous scenarios show an increase in travel time distribu-

tions along a range of streamlines compared to travel time distributions in homogeneous scenarios. This is a strong indication of the emergence of preferential flow in heterogeneous scenarios. The emergence of solute non-equilibrium effects is due to the emergence of concentration gradients in heterogeneous systems due to local variations in water content and solute transport.

The averaged total drainage results show that larger numbers of pore volumes are required to flush solute mass from heterogeneous porous media. More efficient flushing is achieved when continuous modes of infiltration are used. Decreasing infiltration rates slightly increases the non-equilibrium in transport, reducing efficiency of flushing. For flow and transport in heterogeneous small scale systems, infiltration rate and infiltration pattern acts as the controlling factors for non-equilibrium in transport due the induced variations in water content in the system.

Reducing the emission potential from a full scale MSW landfill with continuous infiltration requires large amounts of water, hence it is infeasible. Especially when taking the heterogeneity of a landfill in to account. Slow diffusion from the immobile pore water will require a very long time. Actively approaches aiming to reduce residence time of water in the waste body are probably the most effective approach for controlling emissions via leachate.

The single continuum equilibrium coupled flow and transport model we developed shows the emergence of non-equilibrium effect in small scale heterogeneous systems. These results provide compelling evidence that preferential flow for a full scale landfills is most likely. However, using a single continuum deterministic modelling methods based on volume averages or empirical values of these waste properties gives different results from field observations is impractical because of the very small REV scale required. Upscaled approaches which consider the non-equilibrium transport provide better results corresponding to field observations. We recommend utilization of transfer function approach to model leachate dynamics of full scale landfills.

Chapter 4

Controlling factors of non-equilibrium in transport: Lab scale experiments with numerical simulations

Abstract

We believe the heterogeneous and unsaturated nature of landfills causes its leachate to flow in preferential pathways. This preferential flow leads to non-equilibrium solute transport at the macro-scopic scale. In this research, we study the controlling factors responsible for the emergence of non-equilibrium behaviour in a two dimensional unsaturated sand frame. The hypothesis is that material heterogeneity and infiltration patterns and rates affect transport equilibrium. We compare flow and transport in a heterogeneous domain with that in a homogeneous domain. Both the domains are subjected to similar initial unsaturated conditions and water is applied to the top with different infiltration patterns and application rates. The results show that more time and water is required to leach out the solute from heterogeneous scenarios compared with the homogeneous case. Two lab scale experiments are simulated using a two dimensional deterministic model. In the model, the water flow is represented by Richards' equation and the non-sorbing, single component, solute transport by the advection dispersion equation. The results observed

in the experiments and the numerical solutions give us insight into the non-equilibrium phenomenon occurring in full-scale waste bodies.

Keywords: Unsaturated medium, preferential flow, non-equilibrium in transport, numerical simulation.

4.1 Introduction

The heterogeneous nature of the waste bodies in landfills leads to a rapid flow of leachate through a limited number of flow paths (Blight et al. 1992). These preferential pathways induce flow through the limited volume of the waste bodies inside landfills (Fellner and Brunner 2010). A consequence of preferential flow is that a large amount of pollutants remains in the slow or stagnant flow region of the landfill (Rosqvist and Destouni 2000). Preferential flow leads to a faster leaching of solutes from the mobile water regions in the waste compared to the stagnant flow regions. This induces a concentration gradient between the immobile and the mobile water which induces a (slow) diffusion of pollutants (Brusseau and Rao 1990; Rosqvist et al. 2005a). Thus, the non-equilibrium in solute transport originates due to slow diffusion of pollutants between immobile and mobile water. Non-equilibrium in transport is an important characteristic of the preferential flow occurring in waste bodies (Jarvis 1998; Rosqvist and Destouni 2000; Rosqvist et al. 2005a).

Many approaches to modelling flow and transport in municipal solid waste (MSW) landfills assume that waste bodies can be described using single domain flow with representative elementary volume (REV) scales in the order of cubic meters (McDougall 2007; Gholamifard et al. 2008). This assumption implicitly ignores the existence of preferential flow at scales below the REV scale (See Chapter 3). As a result this continuum modelling approach makes it nearly impossible to simulate the presence of preferential pathways and its effect of non-equilibrium in transport. Consequently, the outcomes are not in agreement with actual field observations (Uguccioni and Zeiss 1997). Many upscaled mathematical models are based on an input-output approach (Rosqvist and Destouni 2000; Rosqvist et al. 2005b; Jury and Stolzy 1982; Jury 1982), a stochastic transfer function approach (Zacharof and Butler 2004b,a), a dual porosity, dual permeability (Bendz et al. 1998; Fellner and Brunner 2010) or stream tubes models (Matanga 1996) and include non-equilibrium transport using a dual porosity or immobile - mobile concepts in their implementations. Results with these models correspond with field observations.

In this chapter we carry out, flow and transport experiments in a small scale laboratory set-up to study non-equilibrium in transport in a sand frame. Water is applied in different

patterns and rates of infiltration on an initially unsaturated heterogeneous and homogeneous samples. The heterogeneous sample is inspired on the type of heterogeneity found in waste bodies. A two dimensional (2D) coupled water flow and solute transport model was used to simulate the experiments. In this model Richards' equation (RE) (Celia et al. 1990a) is used to model unsaturated-saturated water flow. The non-sorbing, single component, solute transport is modelled using the advection dispersion equation (ADE) (Fetter 1993). This flow and transport coupled model is the Variably Saturated Flow and Transport (VarSatFT) toolbox implemented in MATLAB (MATLAB 2014b). The hypothesis for this research is that material heterogeneity, infiltration patterns and infiltration rates are controlling factors for non-equilibrium solute leaching.

The set-up for the 2D sand frame is described in section 4.2 together with the description of the numerical simulations. The results indicating the consequences of the presence of heterogeneities and the different boundary conditions are reported in 4.3. Section 4.4 contains concluding remarks.

4.2 Materials and Methods

4.2.1 Lab setup of 2D sand frame

A sketch of the experimental set-up used in this research is shown figure 4.1. The experiment was carried out in a temperature and humidity controlled environment at 19 °C and 55 % relative humidity. A photograph of the aluminium framed, glass panelled box used in this experiment is shown in figure 4.2. Three types of well graded sand were used (See Table 4.1). Water was infiltrated at the top of the sand frame through a polyethylene infiltration pipe, of 1.00×10^{-2} m diameter, with holes of diameter 1.00×10^{-3} m cm^{-1} along its length of 0.40 m. Woollen threads were weaved inside the holes of the infiltration pipe, in order force the infiltration to a drip mode. The infiltration pipe was connected to a hydraulic peristaltic pump (VERDERFLEX R2550120 AU RS1). Two polyethylene water cans, each of 12 l capacity were placed on two weighing scales in order to automatically record the infiltration and the drainage rates (METTLER PM 16,P). Common salt (NaCl) was used as a tracer. Electrical conductivity (EC) was measured with a sensor (EUTECH EC91346S and Transmitter DO 9786T-RI) placed in the bottom outlet of the sand frame in order to monitor variations in the salt concentration in the leachate. All measurements were computer controlled.

A thin geo-synthetic filter paper was laid at the bottom, inside the frame to prevent flushing of sand particles. Two experiments were done, one with a homogeneous domain and second with a heterogeneous domain inspired on the heterogeneity found in waste bodies (See figure 4.3). In both spatial scenarios fine sand, Sa1 with a thickness 0.04 m

Table 4.1: Abbreviations used in this chapter.

Abbreviation	Lengthen
Sa1	Sand sample with particle size ranging between 100 μm - 250 μm
Sa2	Sand sample with particle size ranging between 250 μm - 500 μm
Sa3	Sand sample with particle size ranging between 500 μm - 1 mm
Hom	Homogeneous scenario
Het	Heterogeneous scenario
C41	Continuous mode inflow of magnitude of 41% of pump flow rate.
S41	Square pattern inflow of magnitude of 41% of pump flow rate.
S51	Square pattern inflow of magnitude of 51% of pump flow rate.
S61	Square pattern inflow of magnitude of 61% of pump flow rate.
V4181	Variable intermittent pattern inflow of magnitude ranging between 41%, 51%, 61%, 71% and 81% of pump flow rate.

was placed at the bottom of the frame in order to act as bottom filter. This fine sand has a high air-entry value and should remain fully saturated throughout the experiment. In the homogeneous scenario only one type of sand, Sa3 was used. For the heterogeneous scenario two types of sand, Sa2 and Sa3 were used. The heterogeneity in the heterogeneous scenario was further increased by introducing some impermeable plastic strips at different locations. A vibration table (TRILTECHNIEK TT-100) was used for both the scenarios to compact the material inside the frame.

Each experiment was started by initially saturating the sand frame from the bottom with a 0.50 kg m^{-3} NaCl salt solution. After an equilibration time of 3.0 hours, the water was allowed to drain over night against a fixed bottom out-flow level, leading to a hydrostatic unsaturated pressure head profile in the sand frame. The experiments consisted of flushing the remaining salt by applying fresh water to the top of the sand frame with the infiltration tube using different infiltration rates and patterns. Discharge rates and electrical conductivity of the draining water were continuously measured during the experiment until the electrical conductivity indicated that no salt was present in the leachate.

The fresh water infiltrated at the top of sand frame was applied in a continuous mode, in a square wave pattern and in a variable wave pattern. In the continuous mode only 41% of 0.24 l min^{-1} the fixed pump flow rate was used. In square wave intermittent infiltration pattern, the varying inflow rates were set to 41%, 51% and 61% of pump flow rate. In the variable intermittent infiltration pattern, different percentages of pump flow rates ranging between 41%-81% were used (See Table 4.1). Figure 4.4 shows the cumulative volume applied to the sand frame as a function of time for the different infiltration patterns. All infiltration scenarios were carried out on both the homogeneous and the heterogeneous domains. The duration of each of these drainage experiment was between 1-4 hours. Overall 10 infiltration experiments were carried out (e.g. 2 spatial domains; 1 continuous mode infiltration; 3 square wave pattern infiltration; 1 variable intermittent infiltration pattern).

The EC measurements obtained in mS cm^{-1} from Delta Ohm were recorded in mA and were converted to kg m^{-3} for different known salt concentrations using a calibration curve. The weighing scales are regularly calibrated as part of the service contract with the suppliers.

4.2.1.1 Correction for lab scale measurement

The point of measurement at the discharge outlet was 1.44 m from the point of EC measurement (See figure 4.1). This distance in measurement points leads to a time delay between the discharge and the EC measurements. We correct for this by dividing 1.44 m length of the tube by the outlet discharge velocity. The tube has a constant internal diameter and is assumed to be impermeable to air. The discharge outflow measurement is

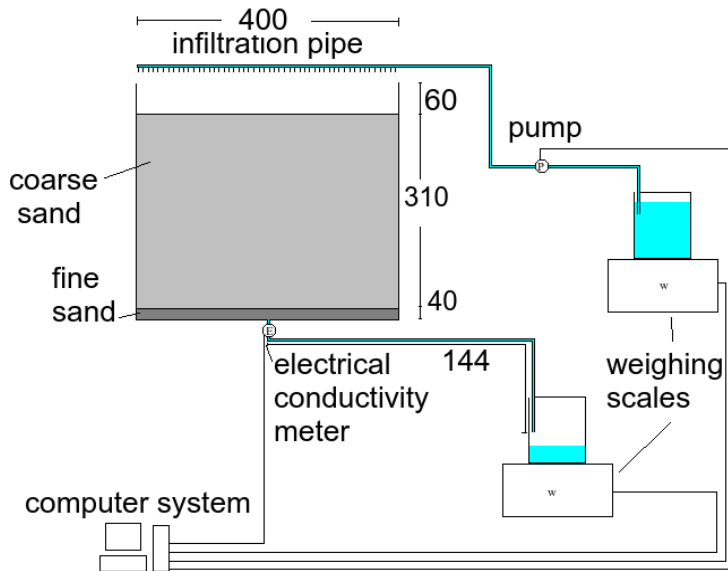


Figure 4.1: Sketch of the lab scale experiment (All dimensions are in millimetres and diagram is not to scale).

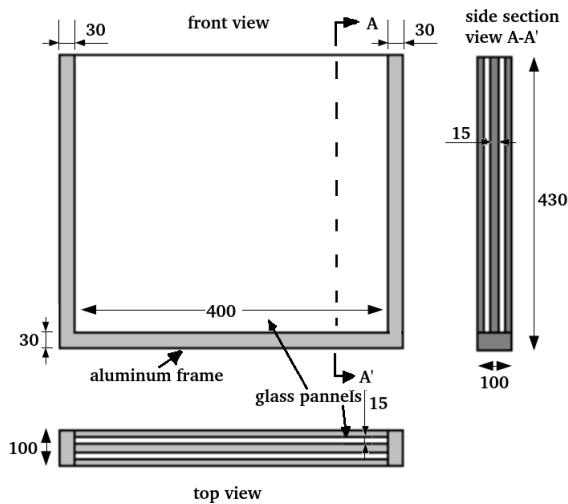


Figure 4.2: Glass panelled aluminium frame used for the lab scale experiment (All dimensions are in millimetres and diagram is not to scale).

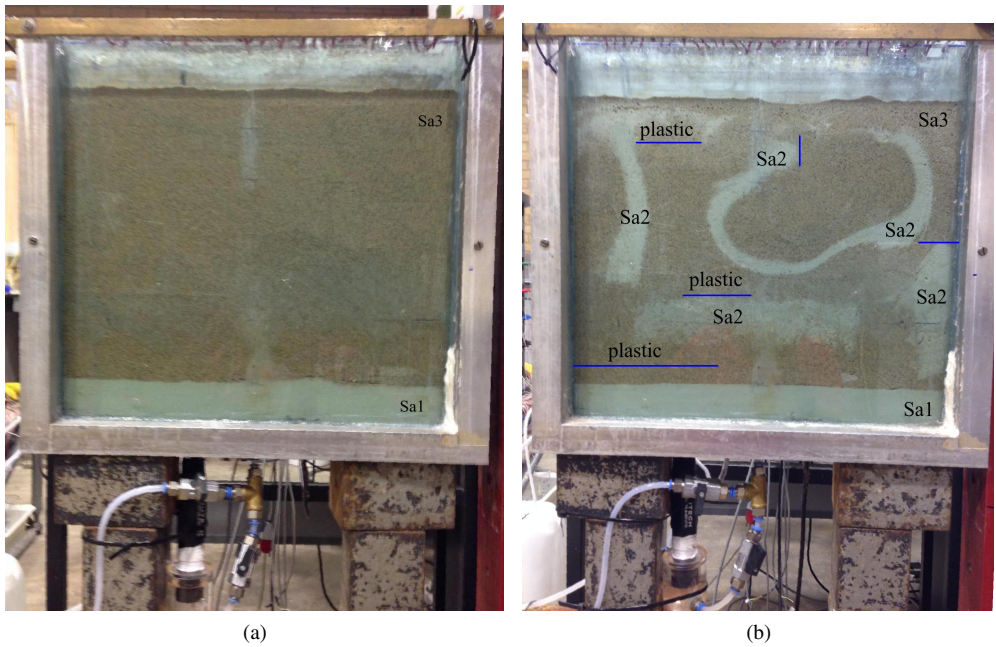


Figure 4.3: Homogeneous (a) and Heterogeneous (b) domains, in which Sa1, Sa2 and Sa3 are the different types of sands used.

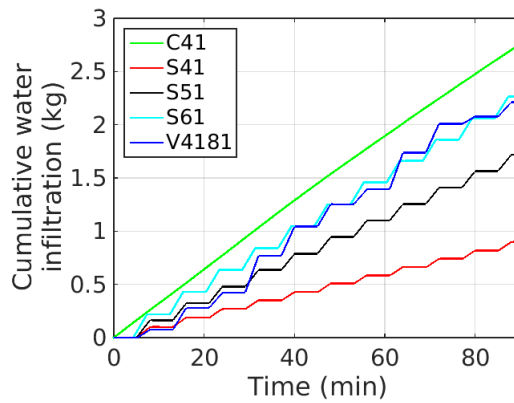


Figure 4.4: Cumulative infiltration for different patterns and rates.

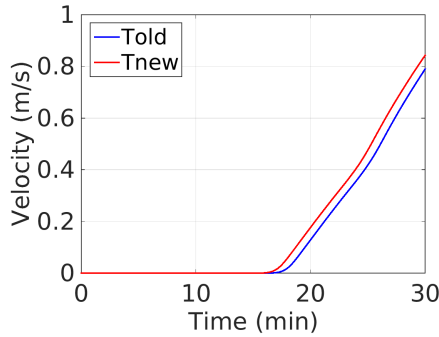


Figure 4.5: The time delay correction for S51 infiltration scenario.

Table 4.2: Material parameters for different types of sands.

Material parameters of sand	Sa1	Sa2	Sa3
α [m^{-1}]	1.36	2.64	4.36
n	15.0946	13.4219	8.3404
θ_r [$\text{m}^3 \text{m}^{-3}$]	0.0759	0.0823	0.1423
θ_s [$\text{m}^3 \text{m}^{-3}$]	0.4393	0.4190	0.4135
\mathbf{K}_{sat} [m s^{-1}] in xx and zz	1.8600×10^{-5}	1.7620×10^{-4}	4.4525×10^{-4}

corrected for this time delay. Figure 4.5 shows the corrected (Tnew) and old (Told) discharge times for the square intermittent inflow rate, where, $\text{Tnew} = \text{Told} - \text{time delay}$. The discharge velocity shown on the y-axis was calculated by dividing the outflow discharge rate by the cross sectional area of tube. All results presented in this chapter are based on Tnew.

4.2.2 Material properties for numerical simulations

The measurements with infiltration pattern S41 for both the homogeneous and the heterogeneous domain were simulated using the VarSatFT toolbox. VarSatFT is an implementation of the mixed-form of RE with Picard iteration (Celia et al. 1990a) together with an implementation of the advection dispersion equation using an Eulerian - Lagrangian approach. In this approach, dispersion was solved on Eulerian nodes and advection was solved using Lagrangian markers (Refer to Chapter 2 for the general equations and for initial and boundary conditions equations of RE and ADE).

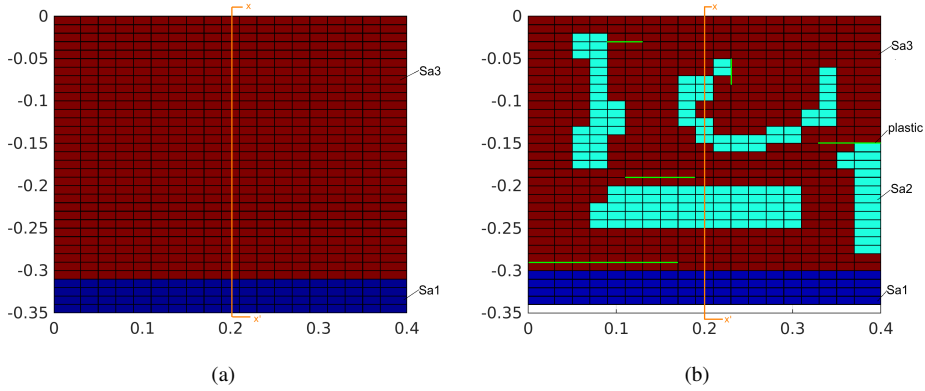


Figure 4.6: Mesh for Hom(a) and Het (b) scenarios used for numerical simulation.

The unsaturated retention parameters of the sands Sa1, Sa2 and Sa3 were determined using an evaporation method with the a HYPROP-S UMS equipment. These retention parameters were then obtained from the measurements using a Bayesian inversion scheme with the DiffereNtial Evolution Adaptive Metropolis (DREAM_{ZS}) toolbox, implemented in MATLAB (Vrugt et al. 2008). Table 4.2 gives the parameters values with highest likelihood. The recommended settings for DREAM_{ZS} for this research are listed in Appendix C. The falling head method was used to determine the saturated hydraulic conductivities of the sand samples by using the KSAT UMS equipment (See Table 4.2).

We constructed the mesh for homogeneous (Hom) and heterogeneous (Het) scenarios using the material parameters as listed in Table 4.2 (See figure 4.6). The initial and boundary conditions for the S41 infiltration pattern are listed Table 4.3. The z_{ref} and ψ_{amb} values were obtained by observing the boundary heads at the bottom of the frame (See figure 4.3). The values for K_{surf} in the Robbins bottom boundary condition were estimated from trial simulations. The top boundary condition for the intermittent infiltration q_{top} was $-7.70 \times 10^{-5} \text{ m s}^{-1}$ (See figure 4.7). Surface ponding was observed when the infiltration (q_{top}) was greater than infiltration capacity ($K(\psi)$). The top boundary condition in the implementation of the RE was able to account these surface ponding conditions (for details see Sec B.1.1 of Appendix B).

The measured initial solute concentrations were used for the simulations. The top boundary condition was a concentration boundary, c_{top} and the bottom boundary condition was a zero-gradient condition, $\nabla c = 0$. We estimated the values of D_m following Rowe and Badv (1996) and α_L and α_T following Fetter (1993) (Refer Chapter 2).

Table 4.3: Assumed parameters and boundary conditions for numerical simulation.

Material parameters	Homogeneous	Heterogeneous
z_{ref} [m]	-0.12	-0.11
K_{surf} [s^{-1}]	5.00×10^{-2}	5.00×10^{-3}
ψ_{amb} [m]	-0.17	-0.17
c_{ini} [$kg\ m^{-3}$]	0.50	0.50
c_{top} [$kg\ m^{-3}$]	0.00	0.00
D_m [$m^2\ s^{-1}$]	1.07×10^{-9}	1.07×10^{-9}
α_L [m] for Sa1 and Sa2	0.10	0.10
α_T [m] for Sa1 and Sa2	0.01	0.01
α_L [m] for Sa3	0.50	0.50
α_T [m] for Sa3	0.05	0.05

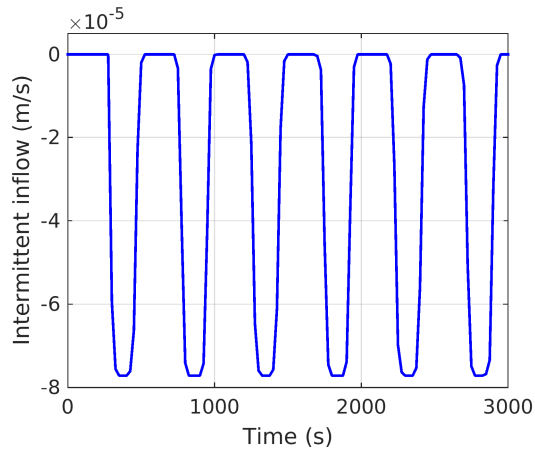


Figure 4.7: Intermittent inflow applied at the top edge of domain used during numerical simulations.

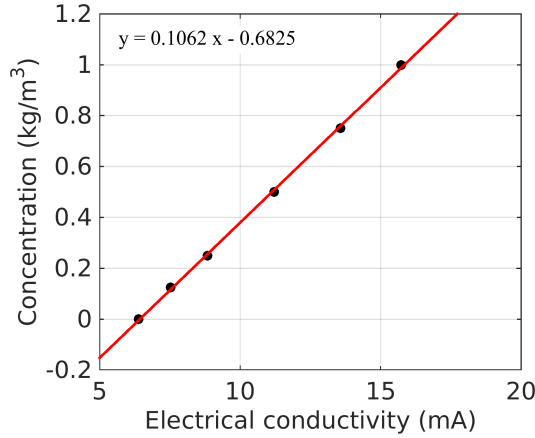


Figure 4.8: Calibration plot for salt solution.

4.3 Results and Discussion

4.3.1 EC calibration for lab scale experiments

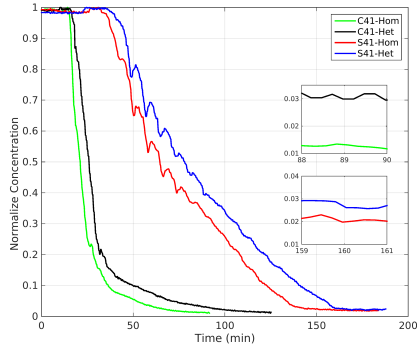
The solute concentration of the solution used for saturating the domain was 0.5 kg m^{-3} . This concentration is well in the linear range of the calibration curve between EC and solute concentration (figure 4.8), so we can directly obtain concentration from EC.

4.3.2 Lab scale experiments: flow and transport in 2D sand frame

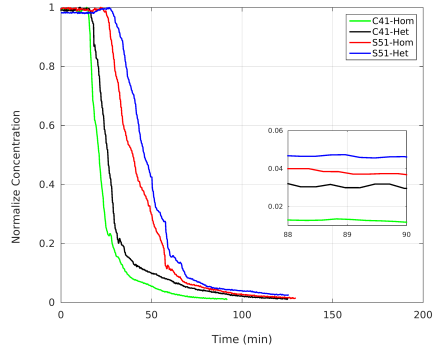
The aim of the experiments is to obtain a deeper understanding how material heterogeneity, infiltration patterns and infiltration rates influences leachate discharge and concentration dynamics.

4.3.2.1 Effect of heterogeneity

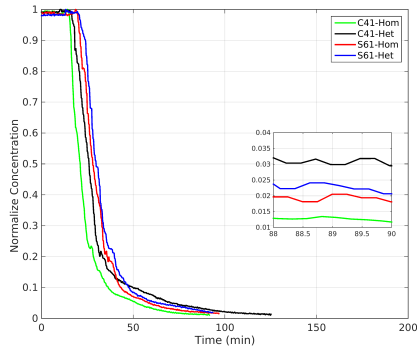
Figure 4.9 shows that the breakthrough curves (BTCs) of salt expressed as normalized drained solute concentration as a function of time, for the homogeneous (Hom) and heterogeneous (Het) domains for all infiltration patterns and rates. Strong tailing is observed in the BTCs for the Het domain. The plastics and variation in sand properties induce of horizontal pressure gradients. Horizontal gradients lead to an increase in variation of flow paths throughout the domain in comparison with the Hom-domain. Variation in flow rate throughout the Het-domain induces concentration gradients between mobile and immobile water and a result slow diffusion occurs from high concentration to low concentration zones (Refer to Chapter 3). The enlarged plots in figure 4.9 show variations



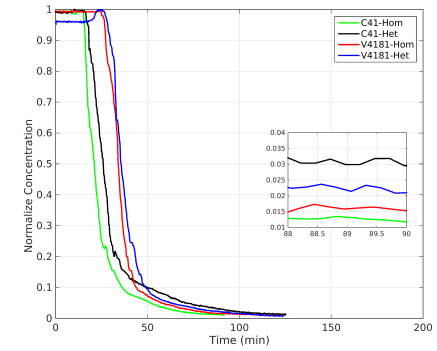
(a)



(b)

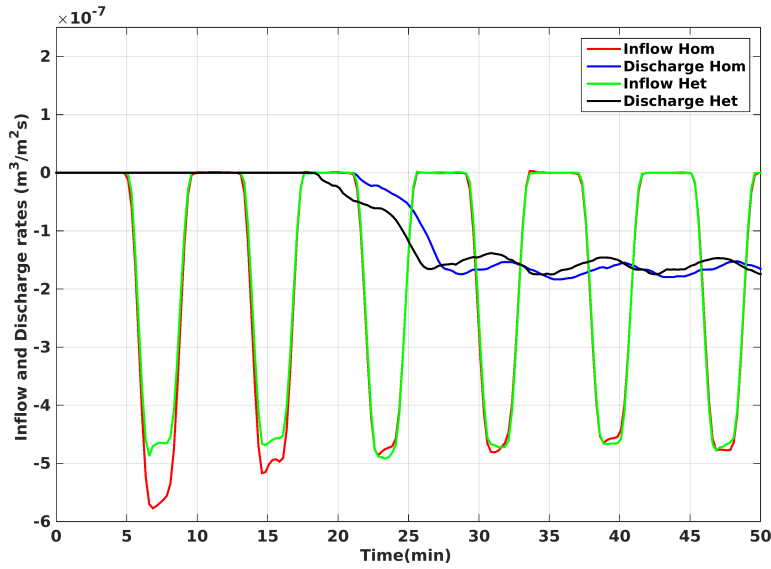


(c)

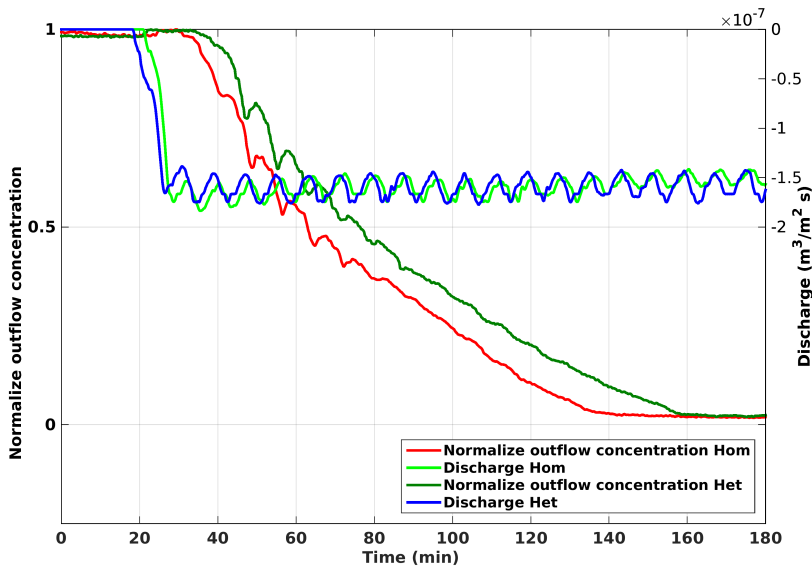


(d)

Figure 4.9: Normalized concentration against time for infiltration scenarios S41(a) S51(b) S61 (c) and V4181 (d) compared with for infiltration scenario C41 in Homogeneous (Hom) and Heterogeneous (Het) domains scenarios.



(a)



(b)

Figure 4.10: Inflow and outflow drainage (a) and normalize outlet solute concentration and discharge in time (b), obtained for S41 infiltration scenario for Homogeneous (Hom) and Heterogeneous (Het) domains scenarios.

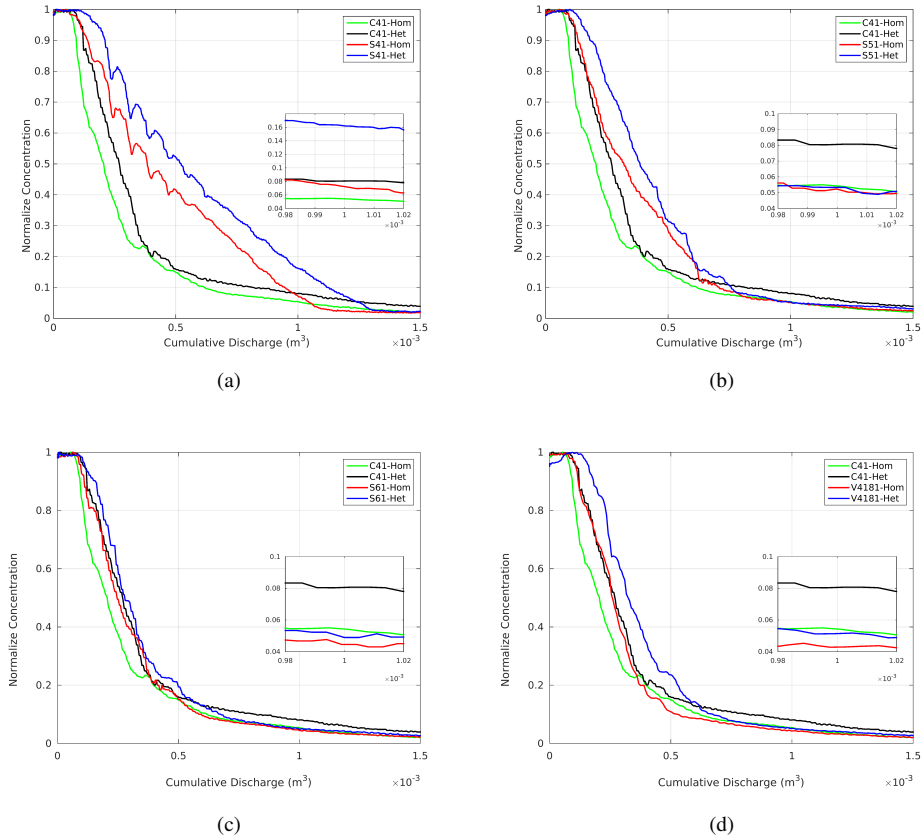


Figure 4.11: Normalized concentration against cumulative discharge for infiltration scenarios S41(a) S51(b) S61 (c) and V4181 (d) compared with for infiltration scenario C41 in Homogeneous (Hom) and Heterogeneous (Het) domains scenarios.

in the tail of the BTCs for all scenarios. All results, indicate non-equilibrium transport. Non-equilibrium effects are most significant for the Het-domain, but also clearly present for the Hom-domain. This is probably due to the presence of the fine sand filter at the bottom of the sand-frame combined with the fact that the outflow only occurred in the middle of the sand frame.

The delayed breakthrough for the Het-domain experiments indicate longer travel times due to the presence of longer streamlines compared with the Hom-domain.. In addition, the BTCs for experiments with low flow rates show a significant spread in travel times, indicating a wider diversity of streamlines compared with the Hom-domains and the experiments with higher flow rates. The variation in leachate concentrations in the Het-domain experiment at the lowest flow rate clearly shows the impact of slow exchange of solutes between mobile and immobile water during stagnant flow conditions. Heterogeneity in material properties combined with variations in boundary conditions have a strong impact on the non-equilibrium phenomena observed and therefore a large impact on the concentration dynamics in the leachate.

4.3.2.2 Effect of infiltration pattern and infiltration rates

Ponding was observed during infiltration for all scenarios. This indicated that the applied infiltration rates were more than the infiltration capacity of the domain (Green and Ampt 1911). Consequently, all experiments were performed at near saturated conditions. The cumulative amounts of water applied during the different experiments differed (See figure 4.4), where most water was applied during the continuous infiltration experiments and least water was applied in the square wave pattern at 41% of the pump rate. The water content in the domain adjusts itself to the inflow regime. Initially the water content needs to increase in order to have the relative permeability increase to match the applied flow rate. This is clearly seen in figure 4.10(a), where the outflow from the domain starts about 18 minutes after the start of the experiment. Once out flow occurs, the variation in outflow is much smaller than the variation in the infiltration rate. The lower the infiltration rate, the larger the variation in the outflow. Water is apparently continuously moving through the domain, and water content is more or less constant implying gravity driven flow. For the square wave infiltration patterns, the water content will vary between a minimum and maximum value controlled by the flow rate and the timing in the infiltration pattern. The variation in water content is largest for the pattern with the lowest flow rate.

The concentration drop for Hom and Het-domains shown in figure 4.10(b) occur more or less at the same time. This difference between the two domains is smaller than we originally expected. We attribute this to the dominant effect of the sand layer we used at the bottom of the sand-frame.

Variation in high flow infiltration conditions has only a limited impact on the measured

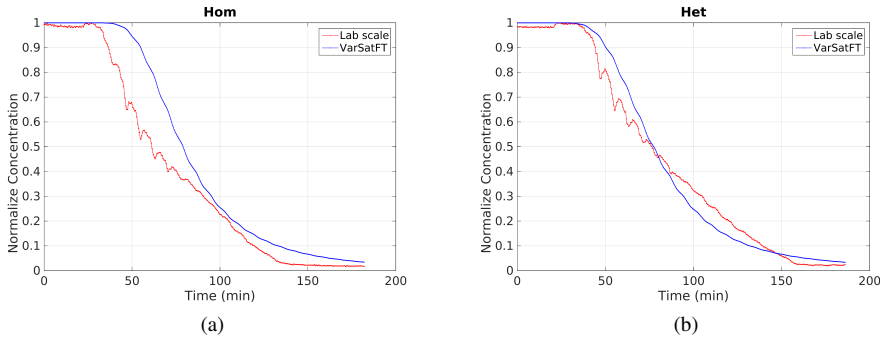


Figure 4.12: Average outlet normalized solute concentrations in time duration obtained for homogeneous (Hom) (a) and heterogeneous (Het) scenarios (b) for lab scale and using VarSatFT simulator.

BTCs because the flow variation in the domain is small. Decreasing flow rates leads to an increasing impact on the BTCs. This is caused by the increased variation in water content in the domain. More water can be stored in a relatively dry domain, increasing the travel time and therefore the impact of slow diffusion on the dynamics in leachate concentration.

Diffusion is slow process, causing a non-equilibrium condition to be present in the domain. As was shown in figure 4.4, different volumes were flushed through the domain during the experiments. In order to investigate the impact of non-equilibrium more closely we plot the BTCs as a function of cumulative discharge (See figure 4.11). If the domain would be in equilibrium, all BTCs would plot on top of each other. The results clearly show the above described effect of increasing non-equilibrium for the experiments where variation in saturation is large. The spread in BTCs is smallest for the S61 scenarios and increase for the V4181, S51 and S41 scenarios. For each of these scenarios, the variation in water content in the domain increases. Clearly non-equilibrium is largest for the S41 scenario in both domains, illustrated by the dynamics in leachate concentration. The increase is caused by recharge of the mobile water during the stagnant phase.

4.3.3 Numerical simulations for lab scale experiments

The results for the numerical simulation of the S41 infiltration experiments for both the Hom and Het-domains are discussed in this section. The are shown in figure 4.12(a) and (b). The measurements for both spatial domains, showed some increasing values in the BTCs which are not found in the numerical results. Currently, we have not been able to identify the cause for the this, however we believe the model does not capture the true water content variation.

Figure 4.13, shows the simulated BTCs as the function of time and number of pore

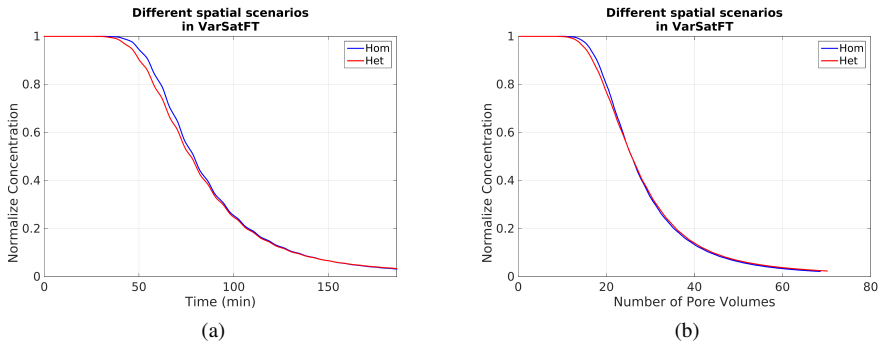


Figure 4.13: Average outlet normalized solute concentrations as a function of time (a) and number of pore volumes (b) obtained for homogeneous (Hom) and heterogeneous (Het) scenarios simulated in VarSatFT.

volumes. Although the difference is small, the Het-domain simulation has slightly earlier break through than the Hom-domain. The tailing however is very similar which indicates the dominant effect of the bottom sand layer on the results. This indicates the presence of diffusion controlled non-equilibrium in solute transport and large number of pore volumes are required for flushing the solute completely for both scenarios.

Figure 4.14 (a) and (b) shows the simulated pressure heads and water contents along the x-x' section marked in figure 4.6, at different times for the Het and Hom-domains. The pressure head profiles clearly indicate the increase in saturations during the experiment. Heterogeneity leads to a variation in water content along the depth is observed for the Het-domain (See figure 4.14 (c) and (d)).

Figure 4.14 (e) shows the height of the water layer on top of the domain due to ponding for both the Hom and Het-domains. Apparently, higher ponding levels are occurring for the Het-domain.

The spatial variation in water content of the different domains is shown in figure 4.15. Clearly both domains are very wet, with the Het-domain clearly being influenced by the presence of heterogeneity.

Figure 4.16 shows the distribution of solute concentrations obtained for both spatial domains, obtained at 0.5 hr, 1.5 hr, 2.5 hr and 3.0 hr. The contour lines show the flushing pattern of the solute at different times. The presence of the plastics and sand Sa2 and Sa3 makes the spatial distribution of solute non-uniform as seen at different time durations. The streamlines in the Het-domain are directed along the periphery of the plastics and form preferential flow paths which are narrowing towards the bottom at discharge outlet. The streamlines in the Hom-domain are directed in vertically downwards but also converge in the fine-sand layer towards the discharge outlet. The consequence is that solutes

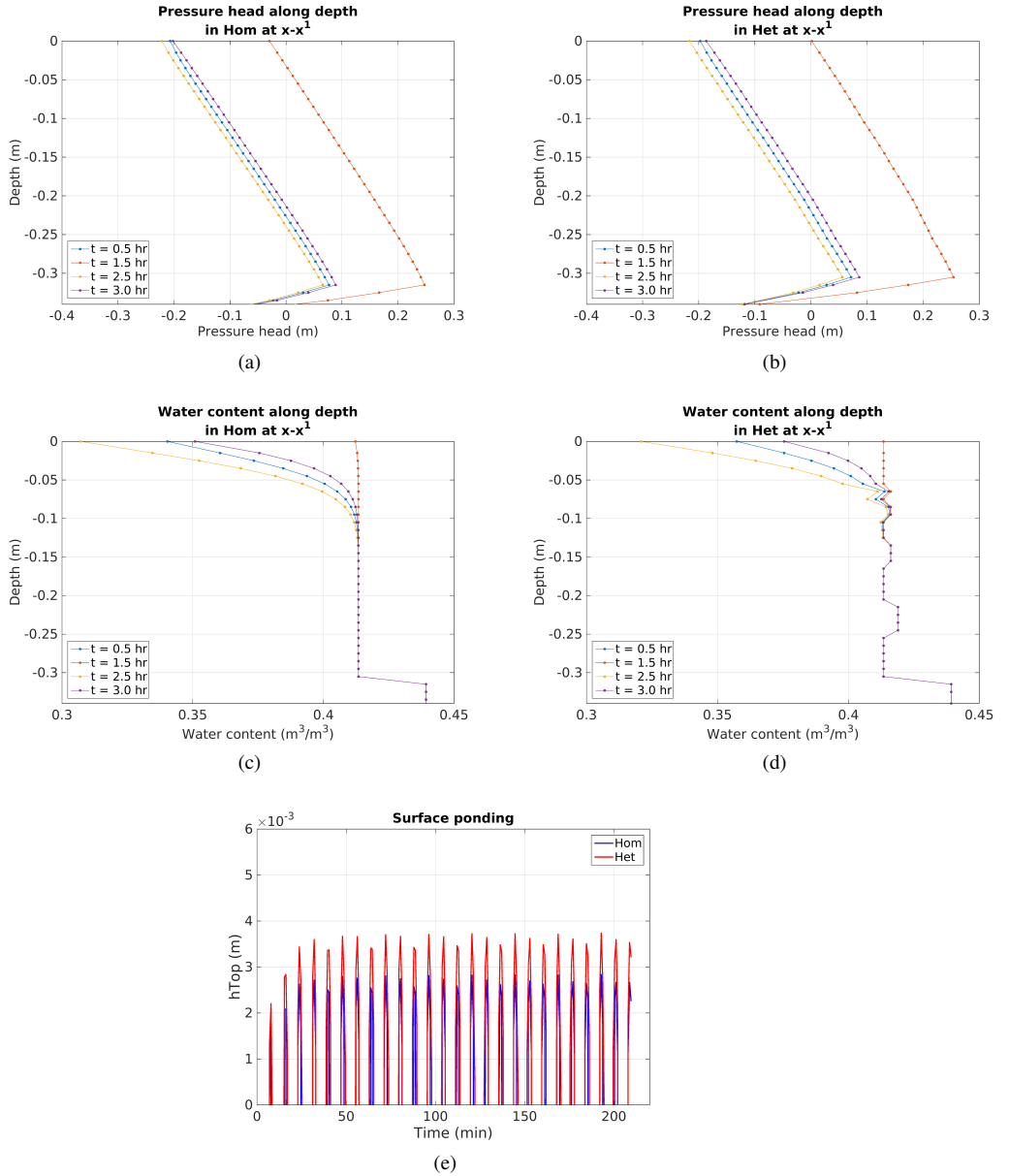


Figure 4.14: Pressure head and water content along $x-x^1$ sections along the depth at time 0.5 hr, 1.5 hr, 2.5 hr and 3.0 hr for S41 infiltration scenario for homogeneous (Hom) ((a),(c)) and heterogeneous (Het) ((b),(d)) scenario, simulated in VarSatFT. Comparing the surface pondings in Hom and Het scenarios (e).

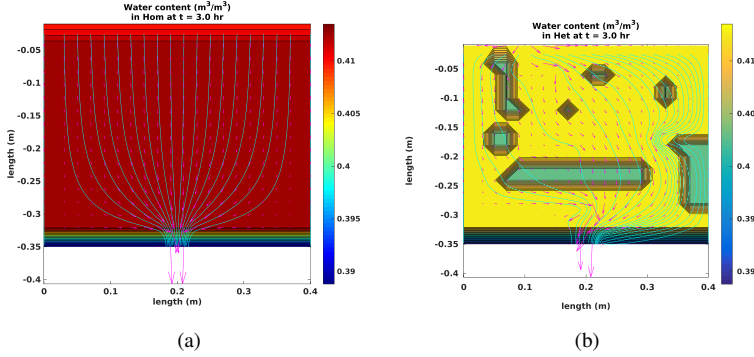


Figure 4.15: Spatial distribution of water content for homogeneous (Hom) and heterogeneous (Het) obtained at 3.0 hr for S41 infiltration scenario simulated in VarSatFT.

remain present in the corners at the bottom of the sand frame. In addition, the small outlet part for the discharge outflow at the bottom of the frame restricts the flow. This effect is found for both the Hom as well as the Het-domain although it is most pronounced for the Het-domain (See figure 4.16 (f) and (h)).

4.4 Conclusions

In this study, the hypothesis was that material heterogeneity, infiltration patterns and infiltration rates act as controlling factors for transport non-equilibrium impacting leachate concentration dynamics. Experiments were performed on homogeneous and heterogeneous domains in order to test this hypothesis. Slightly longer tailing in solute BTCs were observed for the heterogeneous domain compared with the homogeneous domain. But the largest impact the BTCs was found to be the variation in infiltration rates and infiltration timing which is caused by the variation in the water content within the domain. The presence of a fine sand filter at the bottom of the sand-frame dominated the measured results, clouding the differences between the Het-domain and the Hom-domain. However, conclusions about the impact of heterogeneity and varying infiltration boundary conditions can be made.

The experiments clearly showed the impact of saturation on the leachate concentrations. High flow rates lead to near saturated flow conditions where variations in water content were limited. Tailing in the BTCs was an indication of significant diffusion from stagnant water present in both the Hom and the Het domain. Lowering the flow rate in the intermittent infiltration experiment, lead to increased variation in leachate concentration, indicating recharge in the concentration of the mobile water during non-flow conditions in both domains.

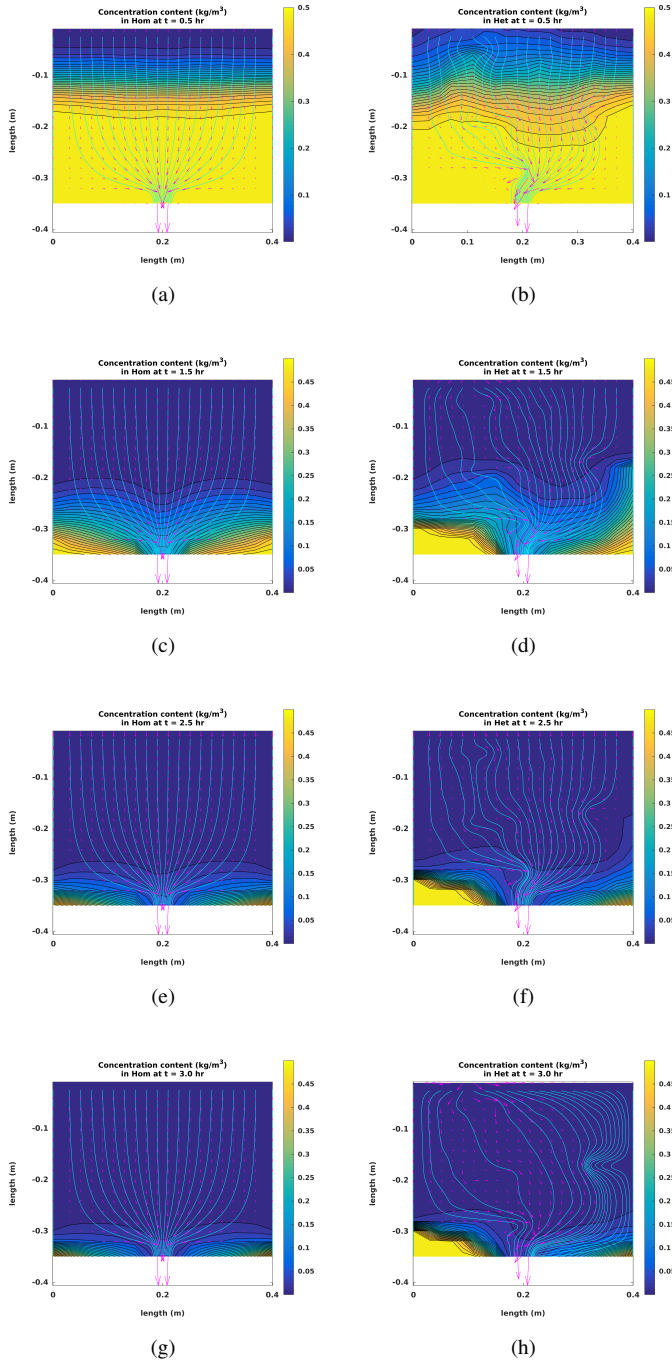


Figure 4.16: Spatial distribution of concentration content for homogeneous (Hom) and heterogeneous (Het) obtained at 0.5 hr, 1.5 hr, 2.5 hr and 3.0 hr for S41 infiltration scenario simulated in VarSatFT.

The results from these experiments clearly indicate that non-equilibrium processes in solute transport will nearly always influence the dynamics of in leachate concentrations. These effects will be more pronounced in full-scale landfills where infiltration is controlled by variations in rainfall, evapo-transpiration and where waste bodies are much more heterogeneous compared with this simple laboratory tests.

The results imply that reducing emission potential from a full scale MSW landfill using flushing would require large amounts of water, making this infeasible. However, presence of preferential flow through a small volume of the waste body leads to fast flushing of this mobile volume and therefore to a fast decrease in leachate concentration. This concentration increases during no-flow conditions, if the time of such no-flow conditions can be limited, concentrations in leachate could be kept at acceptably low values.

Chapter 5

Quantification of soil water retention parameters using multi-section TDR-waveform analysis

Abstract

Soil water retention parameters are important for describing flow in variably saturated soils. TDR is one of the standard methods used for determining water content in soil samples. In this study, we present an approach to estimate water retention parameters of a sample which is initially saturated and subjected to an incremental decrease in boundary head causing it to drain in a multi-step fashion. TDR waveforms are measured along the height of the sample at assumed different hydrostatic conditions. The cumulative discharge outflow drained from the sample is also recorded. The saturated water content is obtained using volumetric analysis after final step involved in multi-step drainage. The equation obtained by coupling the unsaturated parametric function and the apparent dielectric permittivity is fitted to a TDR wave propagation forward model. The unsaturated parametric function is used to spatially interpolate the water contents along TDR probe. The cumulative discharge outflow data is fitted with cumulative discharge estimated using the unsaturated parametric function. The weight of water inside the sample estimated at

the first and final step in multi-step drainage is fitted with the corresponding weights calculated using unsaturated parametric function. A Bayesian optimization scheme is used to obtain optimized water retention parameters for these different objective functions. This approach can be used for samples with long heights. It can be used for samples with uniform particle size distribution for low capillary heads. The multi-step discharge outflow is validated using Richards' equation. This helps to analyse the pressure head and water content distribution in the sample in space and time.

Keywords: retention parameters; time domain reflectometry; multi-step draining; hydrostatic condition.

5.1 Introduction

Water retention parameters for soils are used to determine the relationship between volumetric water content and soil water potential (Buckingham 1907). They are also important for understanding hydraulic conductivity for unsaturated soils (Mualem 1976; van Genuchten 1980) and as such are important to model variably saturated flow through soils. For a wide range of water contents, many methods are available for determining the water retention parameters of soils (Schelle et al. 2013). Water retention properties can be determined using pressure plates (Betteli and Flury 2009; Solone et al. 2012), porous cups or tensiometers (Lourenco et al. 2007; HYPROP-S UMS), tension disk infiltrometer (Šimunek 1999) or cone permeameter (Gribb 1996; Homma et al. 2004). Techniques like evaporation methods (Šimunek et al. 1998) or multi-step outflow (Peters and Durner 2006) are not new to soil scientists either.

The above approaches, however, do not consider vertical distribution of water along the height of sample. The disadvantage of these classic approaches is that only average water content can be estimated from the water balance measurements. The error in estimation of water retention parameters thus increases when height of the sample is increased (Betteli and Flury 2009; Solone et al. 2012). Also an error in parameter estimation increases when measurements are performed close to air entry, making measurements under wet conditions problematic (Peters and Durner 2006).

Recent advances in interpreting Time Domain Reflectometry (TDR) wave forms have led to the approaches which can estimate the distribution of water content along the probe (Heimovaara et al. 2004; Laloy et al. 2014). However in these methods the number of parameters to be estimated increases with the chosen resolution.

In this research, we present an approach quantifying the water retention properties for an initially saturated sample subjected to a multi-step outflow experiment, where the

boundary head is incrementally decreased causing water to drain from the sample. The TDR measurements are obtained along the height of sample at the moment when we can assume the sample is at hydrostatic equilibrium based on the measured outflow. The cumulative outflow is recorded with a computer system. The weights of the sample are measured at the first and final step during the multi-step drainage. Using a parametric function for describing the vertical distribution of water content along the TDR probe we can significantly reduce the number of unknowns in this problem. We discretize the length of TDR probe into a discrete number of nodes. Using the van Genuchten equation (van Genuchten (1980)) together with the linear TDR calibration function of Ledieu et al. 1986 allows us to calculate the apparent permittivity value for every node along the height of sample assuming hydrostatic conditions. The parameters in this coupled equation are obtained by optimization using the frequency domain multi-section scattered function (MSSF) (Feng et al. 1999; Heimovaara et al. 2004). The objective of the optimization is to minimize the difference between the measured and the modelled, TDR waveforms, the cumulative discharge outflow and the weight of water inside the sample obtained during first and final step involved in multi-step drainage. The objective function is optimized using the Differential Evolution Adaptive Metropolis (DREAM_{ZS}) algorithm (Laloy and Vrugt 2012; Laloy et al. 2014) to obtain the soil water retention parameters.

The cumulative discharge data obtained from the multi-step drainage experiment is validated using Richards' equation (Celia et al. 1990a). This is carried out using the flow model of Variably Saturated Flow and Transport (VarSatFT) simulator (See Chapter 2). From the simulation results we obtain the pressure head and water content distributions in time and along the height of sample.

The remaining of the chapter is as follows. Section 5.2 describes the theory of our approach. Section 5.3 describes methods of the wave propagation model, DREAM_{ZS}, materials and methods for calibration TDR system and multi-step drainage experiment, numerical modelling using flow model of VarSatFT simulator. Section 5.4 describes the results and discussion for the, calibration for TDR waveforms, the posterior distribution analysis of the optimized water retention parameters, its comparison with other approaches, and numerical simulation using Richards' equation. Finally section 5.5 gives the conclusions.

5.2 Theory

The sample is obtained or packed in a cylinder with a height L and a constant cross-section area A_c . From the bottom of this sample we install a two - wire TDR probe. The sample is initially completely saturated with water from the bottom using a head balancing water reservoir at the lower boundary. This allows for the head at the bottom

boundary condition to be decreased in several steps. The cumulative amount of water drained ($\sum Q_{out}$) from the sample due to every incremental decrease in boundary head is recorded in time t . Before applying the next step in the bottom boundary conditions, we wait until hydrostatic conditions, which we verify by checking the outflow. The TDR waveforms are measured during these hydrostatic conditions. The weight of the sample is measured at the first and final step. After the final step, we estimate the remaining water content, dry and wet bulk densities by measuring the weight of the material before and after drying in an oven.

The flow through the sample after change in boundary head can be described with the unsaturated form of Darcy's law (5.1).

$$q_z = -k_r(\psi)K_{sat,z}\left[-\frac{d\psi_{wat}}{dz} + 1\right] \quad (5.1)$$

In which q_z is the specific discharge or Darcy velocity $[M/L]$ in the vertical direction, ψ_{wat} is the pressure head along the height of the sample $[L]$, z is the vertical direction, which is assumed negative in downward direction, k_r is the relative hydraulic permeability function and $K_{sat,z}$ is the vertical component from the saturated hydraulic conductivity tensor $[L/T]$.

At hydrostatic conditions, there is no flow ($q_z = 0$) inside the porous domain implying that $\frac{d\psi_{wat}}{dz} = -1$ and that the pressure head distribution along the height of the sample can be calculated using equation (5.2).

$$\psi_{wat}(z) = z_{aw} - z \quad (5.2)$$

Where z_{aw} corresponds to the measured boundary heads at the lower boundary of the sample. The top edge of the sample is considered as the reference position for measuring pressure head. Knowing the pressure head along the sample allows us to calculate the water content using the van Genuchten equation (van Genuchten 1980) (Equations (5.3) and (5.4)).

$$S_{eff} = [1 + (\alpha_{wat}|\psi_{wat}|)^{n_{wat}}]^{-m_{wat}} \quad (5.3)$$

$$\theta_{wat} = \theta_r + S_{eff}(\theta_s - \theta_r) \quad (5.4)$$

Where S_{eff} is the effective saturation [-], α_{wat} is the air entry value $[1/L]$, θ_r is the

residual water content $[L^3/L^3]$, θ_s is saturated water content $[L^3/L^3]$, θ_{wat} is the volumetric water content $[L^3/L^3]$ and n_{wat} [-] and $m_{wat} = 1 - 1/n_{wat}$ are other empirical water retention parameters.

Using the linear TDR calibration equation of Ledieu et al. (1986) allows us to relate the water content (θ_{wat}) in the sample to the apparent dielectric permittivity ϵ_{app} , which can be obtained from the TDR waveforms (See equation (5.5)).

$$\theta_{wat} = a_{wat}\sqrt{\epsilon_{app}} + b_{wat} \quad (5.5)$$

where a_{wat} and b_{wat} are linear curve fitting coefficients. We assume ϵ_{app} is independent of the frequency for the TDR measurements. We also assume that ϵ_{app} is closely related to the real part of the dielectric permittivity (See equation D.15 in Appendix D).

Combining equation (5.4) and equation (5.5), we obtain

$$\epsilon_{app} = (c_{wat} + d_{wat}S_{eff})^2 \quad (5.6)$$

where

$$c_{wat} = \frac{\theta_r - b_{wat}}{a_{wat}} \quad (5.7)$$

$$d_{wat} = \frac{(\theta_s - \theta_r)}{a_{wat}} \quad (5.8)$$

The distribution of apparent permittivities along the length of the sample is to calculate the TDR waveform using the multi-section wave propagation model as described in Heimovaara et al. (2004).

The cumulative discharge outflow ($\sum Q_{out}$) is recorded during multi-step drainage experiment is fitted to the cumulative discharge estimated from the calculated water content distribution (See right hand side of equation (5.9)).

$$\sum_{t_{aw}=2}^{t_{aw}=3} Q_{out} = A_c \cdot \left[\sum_{t_{aw}=1}^{t_{aw}=2} \theta_{wat} \cdot \Delta z - \sum_{t_{aw}=2}^{t_{aw}=3} \theta_{wat} \cdot \Delta z \right] \quad (5.9)$$

where

$$\left[\sum_{t_{aw}=1}^{t_{aw}=2} \theta_{wat} \cdot \Delta z - \sum_{t_{aw}=2}^{t_{aw}=3} \theta_{wat} \cdot \Delta z \right] = (S_{t_{aw2}} - S_{t_{aw3}}) \cdot \theta_e \quad (5.10)$$

and

$$S_{t_{aw}} = \sum_{i=1}^N S_{eff} \Delta z \quad (5.11)$$

and

$$\theta_e = \theta_s - \theta_r \quad (5.12)$$

where Q_{out} is the discharge outflow, t_{aw} is the manually recorded times during hydrostatic conditions when taking the TDR measurements. The subscripts 1, 2 and 3 are the different boundary heads. The water content at hydrostatic equilibrium is θ_{wat} (See equation (5.4)). $S_{t_{aw}}$ is the summation of effective saturation along the sample height at time t_{aw} . The sample height is discretized into N nodes of size Δz .

The estimated weight of the water inside the sample at the first and the final step is fitted to their corresponding weights calculated using water content distribution.

$$Wg_{wat}^{t_{aw1}} = \theta_r \cdot A_c \cdot L + S_{t_{aw1}} \cdot \theta_e \quad (5.13)$$

$$Wg_{wat}^{t_{aw5}} = \theta_r \cdot A_c \cdot L + S_{t_{aw5}} \cdot \theta_e \quad (5.14)$$

In equations (5.13) and (5.14) the left hand side is the weight of water estimated knowing its bulk wet and dry densities evaluated using gravimetric analysis. Thus $Wg_{wat}^{t_{aw1}} = \theta_s \cdot A_c \cdot L$ in $[M]$ in which θ_s is estimated after drying the sample in an oven. The $Wg_{wat}^{t_{aw5}}$, is the weight of water remaining inside the sample at the final step, calculated by subtracting the dry density of the sample from the measured density at the final step multiplied by the volume of sample in $[M]$. Weights on the right hand side of equations (5.13) and (5.14) are calculated using equations (5.4) and (5.11).

We optimize the parameters in the above equations by minimizing the difference between modelled and measured TDR waveforms (5.6), cumulative discharge (5.9) and wa-

ter weights in sample at first (5.13) and final (5.14) step using Bayesian optimization algorithm DREAM_{ZS} (Laloy and Vrugt 2012; Vrugt 2016)

5.3 Methods and Materials

5.3.1 Modelling the TDR wave form

The basic modelling approach of TDR waveform has been described by Heimovaara et al. (2004). The MSSF model for system function is given in Appendix D. A schematic overview of the TDR measurement system is given in figure 5.2. The system with two-wire probe is modelled with 12 transmission-line sections (9 subsections within section 4). The transmission line sections 3 to 4 (the cable, connector, and the integral part of cable tester) are modelled using equation (D.8-D.10) (See Appendix D). The two probe model section was modelled with equations (D.5-D.7) (See Appendix D). The value of the static permittivity, ϵ_s for the internal cable-tester sections and the connector was set to 1 because the square root of this parameter is inversely related to the impedance and the length of the sections which both are free parameters in the optimization.

5.3.2 Parameter estimation by DREAM_{ZS}

The DREAM_{ZS} algorithm (Laloy and Vrugt 2012; Vrugt 2016) is an Monte Carlo Markov Chain method used to sample the posterior parameter distribution. This algorithm is based on a Bayesian inference scheme (Thiemann et al. 2001) in which the prior probability density distribution of the model parameters is updated in order to obtain posterior distribution.

DREAM_{ZS} samples the posterior distribution $p(\phi|\hat{\mathbf{y}})$ for their prior distribution $p(\phi)$ and their likelihood $L(\phi|\hat{\mathbf{y}})$, as shown in the following equation (5.15)

$$p(\phi|\hat{\mathbf{y}}) \propto p(\phi) \cdot L(\phi|\hat{\mathbf{y}}) \quad (5.15)$$

where ϕ is the vector of model parameters within Bayesian statistic framework and $\hat{\mathbf{y}}$ is the vector of observations. The settings for DREAM_{ZS} used for this chapter are listed in Appendix D.

The objective function for fitting the parameters in equations (5.6), (5.9), (5.13) and (5.14) are expressed as a natural logarithm of the likelihood function $L(\phi|\hat{\mathbf{y}})$ implemented in the Gaussian form (Guo 2011) which includes the standard deviation of the total error

(model error + measurement error) σ :

$$\ln(L(\phi|\hat{\mathbf{y}})) = -\frac{n}{2} \cdot \ln(2 \cdot \pi) - \sum \ln(\sigma) - \frac{1}{2} \cdot \sum \left(\frac{\hat{\mathbf{y}} - \mathbf{y}}{\sigma} \right)^2 \quad (5.16)$$

where $\hat{\mathbf{y}}$ contains data points of measured waveform, measured cumulative discharges obtained at time t_{aw} , i.e. $\sum Q_{out}$, and estimated quantity of water in the sample obtained by measuring corresponding weights at first and final step. Whereas \mathbf{y} contains modelled data points of the waveform which is constructed by the MSSF-TDR model using predicted values of apparent permittivities along the sample height, ϵ_{app} . The \mathbf{y} also contains modelled cumulative discharges and modelled quantity of water in the sample obtained using water content distribution. The ϕ is the vector of model parameters of equation (5.6), (5.9), (5.13) and (5.14) within Bayesian statistic framework. n is the size of vector $\hat{\mathbf{y}}$.

The vector of model parameters consisted of α_{wat} , n_{wat} , c_{wat} , d_{wat} , θ_e and θ_r and the bulk electrical conductivity σ_{DCC} for each of the measured waveforms (See equation (D.6) in Appendix D) and the boundary head of the last outflow step z_{aw} . We optimized the value for the last boundary condition because control experiments after the measurements on the sample clearly showed that the air entry value of the filter sand pack at the bottom of the column was exceeded between the two last boundary values. The vector σ contains the standard deviations $\hat{\sigma}$ for each dataset (the five measured waveforms, the set of cumulative discharge data and one data set containing the weight of water inside sample at first and final step). The values of $\hat{\sigma}$ in σ are inferred together with the values of ϕ with uniform prior ranging from 1×10^{-9} to 1×10^3 .

5.3.3 Experiment

5.3.3.1 Setup

A cylindrical column with a height of 0.40m and an internal diameter of 0.19m was fitted with a two - wire TDR probe with a length of 30.75×10^{-2} m connected with an epoxy encased probe head of 1.00×10^{-2} m length from the column bottom and a 2.73 m long RG58 C/U type coaxial cable to a MOHR CT Viewer TDR cable tester (See figure 5.1(a)). The wires of the probe were 4.50×10^{-2} m apart. The diameter of each wire was 3.52×10^{-3} m. TDR measurements were performed using a MOHR CT Viewer cable tester. Water and air measurements were taken in order to calibrate the transmission line parameters (Heimovaara et al. 2004).

The bottom of the cylinder was closed and fitted with an outflow port connected to a small head balancing cylindrical reservoir using a polyethylene pipe (See figure 5.1(b)). The overflowing water from the head balancing cylinder was drained into a container

placed on scale. The scale was connected to a computer which continuously recorded the cumulative discharge readings in time duration during the multi-step drainage experiment (See figure 5.1(c)). The weights of the sample at the first and final step involved in multi-step drainage experiment were measured using the weighing scale.

A 0.01 m thick layer of well sorted fine sand with particle size ranging between 60 μm - 100 μm was used as an air impermeable filter at the bottom of the column. For the experiment we filled the column filled with a sorted coarse sand sample with particle size distribution between 250 μm - 500 μm . The coarse sand was filled inside the column layer by layer under water and subsequently compacted by tamping until a height of 0.35 m was reached. The sand column was saturated with water from the bottom and left overnight with a small ponding layer of 0.03 m. We drained the column in step wise fashion by lowering the head balancing cylinder. We assumed that the column was at hydrostatic equilibrium after 24 h. The TDR waveforms were measured at hydrostatic equilibrium. During the multi-step drainage experiment, we covered the top of the column with a moist cloth to avoid any evaporation.

The datum ($z = 0\text{ m}$) was set at the top of the coarse sand in the column. The TDR measurements were taken at the following boundary levels (z_{aw}): 0.03 m, -0.21 m , -0.35 m , -0.49 m and -0.64 m . The time when we changed the boundary level was recorded manually (See t_{aw} in equation (5.9)).

The weight of the complete column was recorded when it was fully saturated (at the first step) and at the final step involved in multi-step drainage. At the end of the multi-step drainage experiment, the sample from the column was put inside an oven for 24 h at 100 °C. Using the weights we calculated the saturated water content θ_s and the total amount of water in the sample at the end of the experiment.

5.3.3.2 Calibration of the parameters in the MSSF-TDR method

A summary of all steps to involved with the TDR measurement and interpretation are given in Table 5.1. The first two steps were used to calibrate the TDR system using the approach of Heimovaara et al. (2004). The first calibration step (Step 1 in Table 5.1) is needed to determine the two parameters (inverse of rise time, α and starting position of input signal, t_0) for the analytical input function (See equation (2) of Heimovaara et al. 2004). We measured a waveform with a 50 Ω load while making sure that the initial step in the waveform was sampled. In the second step TDR waveforms measured in air and water were used to obtain the parameters for the transmission line sections of the cable tester, the coaxial connectors, the coaxial cable, the probe head and two-wire probe using equation (D.3-D.12) (in Appendix D).

Table 5.2 gives a summary of the parameters that we obtained from the calibration measurements. In total 134 parameters are required, to fully model the TDR waveforms

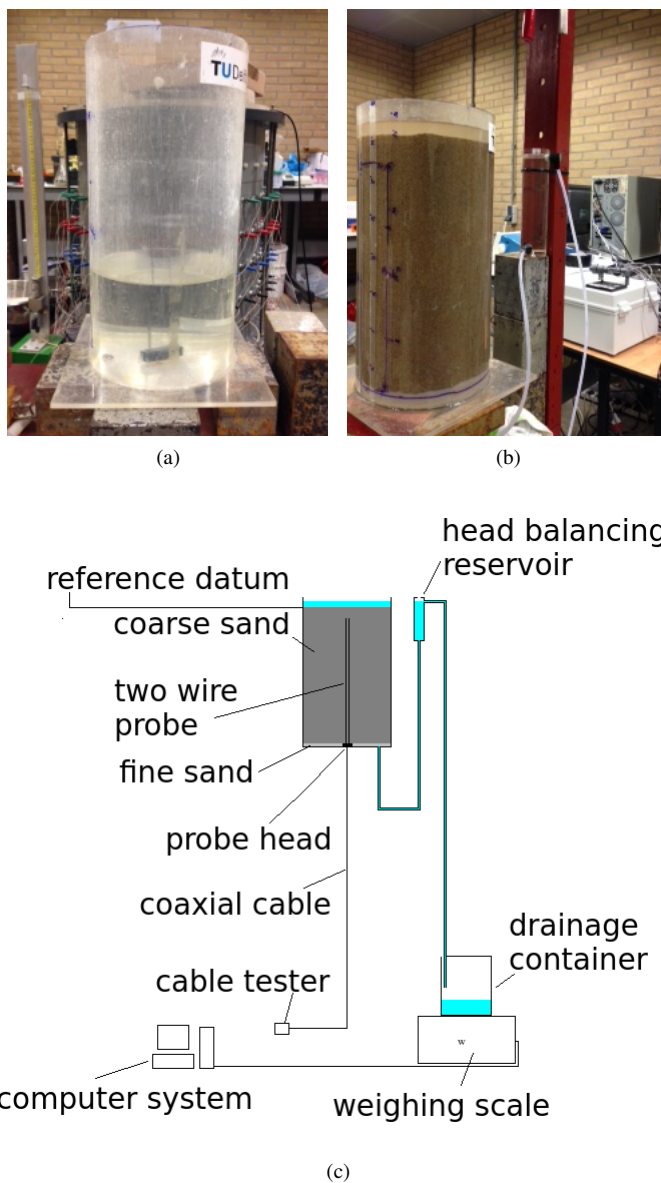


Figure 5.1: TDR column (a), saturated TDR sand column with initial water ponding (b) and schematics of multi-step draining experiment (c).

Table 5.1: Summary overview of all waveform measurement and waveform analysis-steps carried out for calibrations and experiment (See Appendix D).

	Measurements	Analytical Steps
<u>Calibration</u>		
Step 1	Measurement of 50 Ω load.	DREAM _{ZS} optimization of parameters in analytical input-signal 2 parameters.
Step 2	Measurement of probe in water and air.	DREAM _{ZS} optimization of impedance Z for all sections (1 to 12), length L for section 1, 2 and 3, relative static permittivity ϵ_S for section 2 and 3, high frequency skin effect term R_{AC} for section 1, 2 and 3, DC resistance term R_{DC} for section 1, 2 and 3, coaxial cable's bulk conductivity σ_{DC} for section 2 and 3, two-wire probe's bulk conductivity σ_{DCC} for section 1.
<u>Multi-step drainage experiment</u>		
Drainage of saturated sand sample in multi-step fashion till it attains dryness.	Measurement of series of TDR waveforms at hydrostatic equilibrium. Measurement of cumulative discharge outflow. Measurement of weight of water at first and final step.	DREAM _{ZS} optimization of water retention parameters α_{wat} , and n_{wat} . The first order polynomial curve fitting parameters c_{wat} , d_{wat} as shown in equation (5.7) and (5.8). The water content at the end of the experiment θ_e (See, equation (5.12)). The residual water content θ_r (See, equation (5.13) and (5.14)). The boundary head level z_{aw} (last boundary head in the multi-step drainage). The σ_{DCC} for each waveform (in all 5). The standard deviation of total error σ for each waveform, cumulative discharge and weights of water at first and final step (in all 7) as shown in equation (5.16).

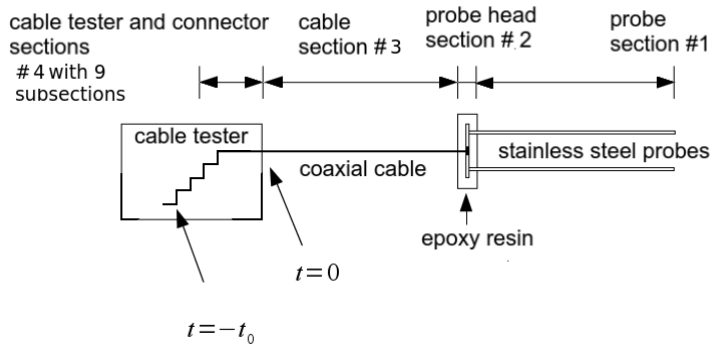


Figure 5.2: Overview of the multi section transmission line connected to the cable tester. The numbers indicate the transmission-line section numbering convention adopted. Section 4 transmission line is inside the cable tester, Section 3 is the coaxial cable, Section 2 is the probe to cable interface, and Section 1 is the two wire probe. Figure used from Heimovaara et al. (2004).

Table 5.2: Overview of all parameters in the 12 section transmission line model for TDR measurement setup.

Probe Section	Parameters	Total
Input	α, t_0	2
Section 4 subdivided into 9 subsections, cable tester and connectors.	$Z_0, b, \epsilon_S, \epsilon_H, \mu_r, f_{rel}, \sigma_{DC}, \sigma_{DCC}, R_{DC}, R_{AC}, L$	99
Section 3 cable	$Z_0, b, \epsilon_S, \epsilon_H, \mu_r, f_{rel}, \sigma_{DC}, \sigma_{DCC}, R_{DC}, R_{AC}, L$	11
Section 2, probe-cable interface	$Z_0, b, \epsilon_S, \epsilon_H, \mu_r, f_{rel}, \sigma_{DC}, \sigma_{DCC}, R_{DC}, R_{AC}, L$	11
Section 1, probe	$Z_0, b, \epsilon_S, \epsilon_H, \mu_r, f_{rel}, \sigma_{DC}, \sigma_{DCC}, R_{DC}, R_{AC}, L$	11
Total		134

for this set-up. Only a few of these parameters were obtained by optimization, the remainder were set to default assumed values. (See Tables 5.1 and 5.2).

The measure of misfits evaluating the input function in first step and fitting the waveforms for air and water medium in second step was expressed by equation (5.16), in which σ was not considered.

5.3.3.3 Multi-step drainage experiment

The TDR probe length was divided into 16 segments. The nodes of size Δz were assigned along the sample height. For different boundary heads, ψ_{wat} and θ_{wat} were estimated along these nodes using unsaturated parametric relations (See equation (5.2) and (5.4)). This implicit discretization of the probe and sample height provides vertical distribution of water content.

Using the transmission line parameters obtained from Step 1 and Step 2 (See, Table 5.1), the optimized values of the parameters as shown in Table 5.1 (See under the sub heading of Multi-step Drainage Experiment) were obtained for measure of misfits with maximum likelihood function as shown in equation (5.16). The optimization was carried out using DREAM_{ZS} to obtain the posterior distribution of α_{wat} , n_{wat} , c_{wat} , d_{wat} , θ_e , θ_r , 5 different σ_{DCC} (i.e. $\sigma_{DCC}^1, \sigma_{DCC}^2, \sigma_{DCC}^3, \sigma_{DCC}^4, \sigma_{DCC}^5$) and 7 different σ (i.e. $\sigma^1, \sigma^2, \sigma^3, \sigma^4, \sigma^5, \sigma^6, \sigma^7$). It was found from the literature (Chesworth 2007; Laloy et al. 2014) that the setted value of the last boundary head, z_{aw}^5 was greater than the air entry head of samples similar to the fine sand sample placed at the bottom of the column. Hence we also included z_{aw}^5 in prior to obtain its posterior distribution.

With the known optimized values of α_{wat} , n_{wat} , c_{wat} , d_{wat} , θ_e and θ_r the θ_s , a_{wat} , and b_{wat} parameters were determined using equation (5.12), equation (5.8) and equation (5.7). The θ_s value estimated using equation (5.12) was checked with its the value determined using gravimetric analysis. Using these optimized parameters and the van Genuchten function (See equation (5.4)) we evaluated the spatial distribution of θ_{wat} at different assumed hydraulic equilibriums.

5.3.4 Numerical modelling of the multi-step drainage experiment

The soil water retention parameters were validated by simulating the cumulative outflow recorded during the multi-step drainage experiment with the Richard's equation (RE). A mixed-form RE with Picard iteration (Celia et al. 1990a) was used to simulate the multi-step drainage experiment. We used the VarSatFT simulator, implemented in MATLAB (MATLAB 2014b) (See Chapter 2).

The 2D spatial domain of 0.01 m width and 0.35 m height was discretized into finite difference grid with a spacing of 5.00×10^{-3} m.

Table 5.3: Calibrated parameters for input function of the Mohr CT-100 cable tester used for TDR measurements.

Parameter	Mean	Std
t_0 [ns]	-1.3087	7.8489×10^{-5}
α [ns^{-1}]	12.4675	0.0131

The initial condition assumed hydrostatic conditions was implemented as

$$\psi_{wat}(x, z, 0) = z_{ref} - z \quad (5.17)$$

where z_{ref} is water level in the domain $[L]$. It is possible to account for water storage in a ponding layer in VarSatFT (See Chapter 2, Appendix B).

The boundary condition at the top of model domain was a zero flow condition for the whole experiment. The boundary at the bottom of the column is a Robbins condition.

$$\mathbf{q}(x, -0.35, t) = K_{surf}(\psi_{amb} - \psi_{wat}) \quad (5.18)$$

where K_{surf} is the surface permeability $[1/T]$ and ψ_{amb} is ambient pressure head $[L]$. For the bottom boundary condition at the bottom of the column, ($z = -0.35$ m), we set ψ_{amb} equal to the different values of z_{aw} for the five steps. We assumed that K_{surf} is equal to $K_{sat,z}$. The saturated hydraulic conductivity K_{sat} of the sand was $4.45 \times 10^{-4} \text{ m s}^{-1}$. The K_{sat} value was obtained using falling head method by using KSAT UMS equipment. The lower boundary condition was changed according to the measured timing of the multi-step drainage experiment. The bottom boundary condition was changed at time t_{aw} 734, 81490, 167580, 254500, 339960 s. The simulation was carried out for 339 960 s with model output at every 1000 s and at each boundary time.

5.4 Results and Discussion

5.4.1 Calibration Step1: The input waveform

The probability density functions for the optimal set of parameters of the input function (See equation (2) in Heimovaara et al. 2004) optimized with DREAM_{ZS} are summarized in Table 5.3 with their mean value and the standard deviation (Std) values.

5.4.2 Calibration Step2: Complete TDR system using Air and Water waveforms

Table 5.4 shows the minimum and maximum of the uniform prior distribution for all parameters optimized with DREAM_{ZS} in order to calibrate the MSSF-TDR model. In addition the table gives the parameter set with the highest likelihood and the standard deviation calculated from the posterior distribution. All parameters obtained have converged to relatively a narrow (normal) distribution, which is an indication that the TDR waveforms for air and water contain sufficient information to identify the chosen 26 parameters.

Figure 5.3 shows the measured waveforms and the optimized waveforms obtained for the highest likelihood for the converged posterior distribution. Sampling last 500 parameters sets from the posterior distribution and plotting the calculated TDR waveforms showed that all waveforms overlap and closely match the measured waveforms. In addition the parameters are within physically realistic ranges.

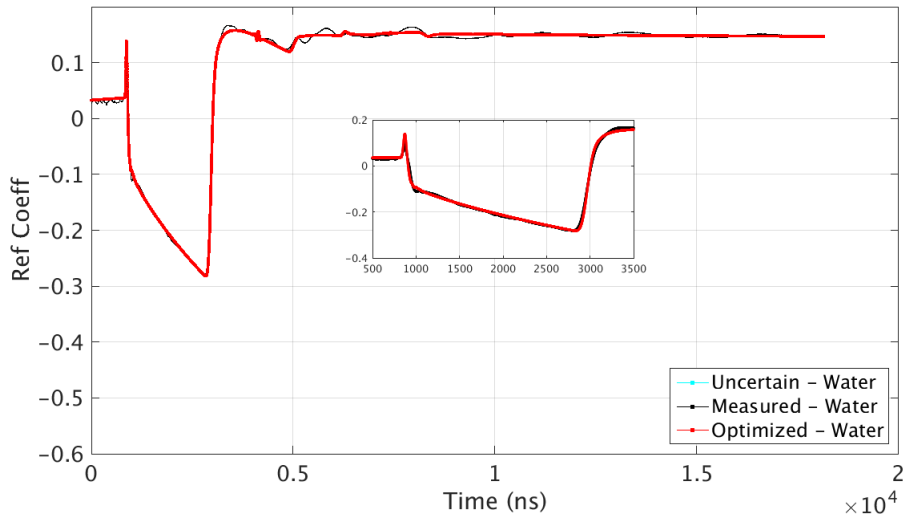
5.4.3 Multi-step drainage experiment

Table 5.5 shows the optimized parameters obtained from the multi-step drainage experiment.

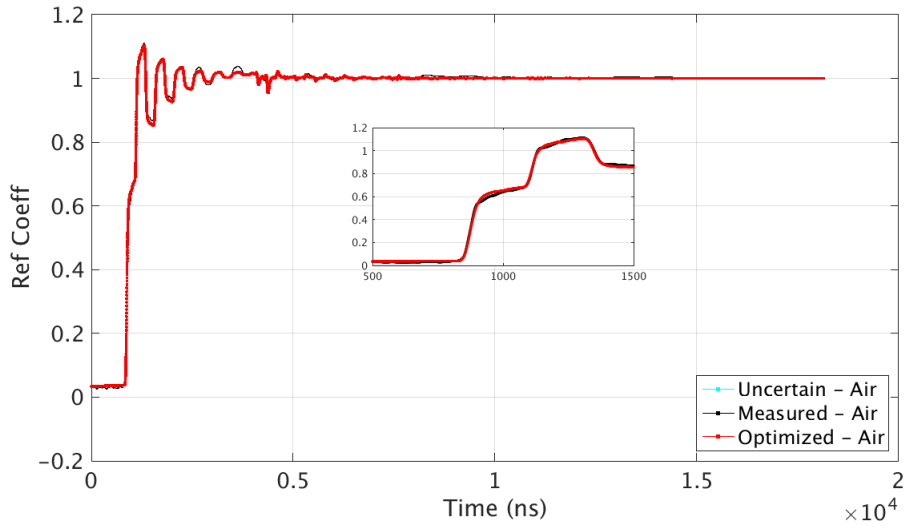
Figures 5.4 and 5.5 shows that the posterior marginal probabilities of all 19 parameters have all converged to clearly defined distributions, each with relatively small standard deviations. The marginal probability distributions plotted along the diagonals shows that c_{wat} and d_{wat} are correlated to some extent. This is due to the fact they both are scaled by a_{wat} (see equations 5.7 and 5.8). The fact that the parameters have converged to distinct relatively narrow distributions with very limited correlations between the different parameters indicates that the model given in equations (5.6) to (5.14) are an accurate description of the measured TDR, the cumulative discharge and water weights datasets.

The optimized air entry value (α_{wat}) and the residual water content (θ_r) matches the values obtained for similar sand samples by others (Chesworth 2007; Laloy et al. 2014). The relatively high value obtained for n_{wat} is due to uniform particle size distribution of the sand sample. The values of a_{wat} , b_{wat} and θ_s (See Table 5.7) determined using equations (5.7), (5.8) and (5.12) are similar to those found by others for similar soils (Heimovaara 1992; Chesworth 2007; Thoma et al. 2013). The decrease in electrical conductivities, σ_{DCC} , is explained by the reduction in water filled pore space for the subsequent drainage steps.

The optimized z_{aw}^5 is larger than the value set as the boundary condition in the experiment which indicates that due to some reason the air entry value of the fine sand layer placed at the bottom of the sand column was exceeded between the boundary condition



(a)



(b)

Figure 5.3: Calibration of Water (a) and Air (b) waveform.

Table 5.4: Prior summary of the posterior parameter for calibration of TDR measurement setup.

Parameter	Tranmission line section	Min _{ini}	Max _{ini}	Min	Max	Optimum	Std
L [m]	1	0.30	0.45	0.30	0.45	0.3160	4.4426×10^{-5}
	2	0.01	0.10	0.01	0.10	0.0101	6.0688×10^{-5}
	3	2.60	2.80	0.50	3.50	2.5626	5.9685×10^{-4}
Z [Ω]	1	120	130	50	175	125.3543	0.0695
	2	120	130	50	175	99.6301	1.6585
	3	65	95	25	100	84.8625	0.0236
	4	45	55	2	100	53.6541	1.6526
	5	45	55	2	100	30.9926	0.8982
	6	45	55	2	100	99.9628	0.4706
	7	45	55	2	100	21.0067	0.2754
	8	45	55	2	100	90.4546	2.9593
	9	45	55	2	100	76.7326	4.5075
	10	45	55	2	100	32.6868	2.8306
	11	45	55	2	100	39.7708	2.4909
	12	45	55	2	100	21.5476	0.7439
ϵ_S [-]	2	1	5	1	15	6.4793	0.3087
	3	1	5	1	15	2.8095	0.0014
$\log_{10}(R_{AC})$ [$\Omega \text{ m}^{-1}$]	1	-20	-10	-20	0	-2.8446	0.0025
	2	-20	-10	-20	0	-17.7357	5.2096
	3	-20	-10	-20	0	-3.5608	0.0071
$\log_{10}(R_{DC})$ [$\Omega \text{ m}^{-1}$]	1	-20	-10	-20	0	-15.0760	2.7628
	2	-20	-10	-20	0	-0.0044	0.1288
	3	-20	-10	-20	0	-13.3061	4.2858
$\log_{10}(\sigma_{DC})$ [S m^{-1}]	2	-5	-1	-20	0	-19.8916	0.1251
	3	-5	-1	-20	0	-16.1439	3.4441
$\log_{10}(\sigma_{DCC})$ [S m^{-1}]	1	-5	1	-20	1	-1.3800	4.1491×10^{-4}

set at z_{aw}^4 and z_{aw}^5 . We think this is because of leakage of air along the probe head. The top of the fine sand layer was exactly flush with the top of the probe head, in order to ensure the probe wires were completely installed in the sample of interest.

Figure 5.6(a) shows the measured waveforms, the optimized waveforms obtained for the highest likelihood for the converged posterior distributions and the uncertainty in the optimized waveforms for last 500 sampled parameter sets from the final distribution parameters. As was the case for the calibration measurements, the uncertainty bandwidth is very small and completely overlaps the best fit waveforms. The fit however is not optimal. The difference in the measure and simulated waveforms can be explained by the simplification we made in the model where we consider the dielectric permittivity to be completely frequency independent and that the electrical conductivity is constant along the probe independent of the water content variation. The mismatch between measurements and simulated results indicate that dielectric relaxation does occur as the electro-magnetic signal moves along the sample.

The RMSE values obtained for simulated waveforms over measured waveform obtained at boundary head z_{aw}^1 , is 1.22×10^{-2} , at z_{aw}^2 is 1.12×10^{-2} , at z_{aw}^3 is 1.17×10^{-2} , at z_{aw}^4 is 1.17×10^{-2} and at z_{aw}^5 is 1.51×10^{-2} . The fact that all values are in the same range indicates similar quality of fits for all measurements.

Figure 5.6(b) shows the measured and optimized cumulative discharge obtained for the highest likelihood for the converged posterior distribution. The width of the uncertainty bandwidth is very narrow for first two steps but it becomes broader for last three steps. The relatively large width of θ_r combined with the presence of a slight correlation in posterior distributions between n_{wat} , c_{wat} , d_{wat} and the optimized value of the boundary head z_{aw}^5 is the cause for this uncertainty (See figure 5.5). The RMSE value for the optimal parameter set is 6.33×10^{-5} . Hence the simulated fit is acceptable.

Figure 5.6(c) and Table 5.6 shows that the optimized weights of the water in sample obtained at first and final step matches closely with the measured data.

In Laloy et al. (2014), the optimization of water content is carried out at every node along the height of sample, without assuming any relation between nodes. We explicitly use a relationship based on the assumption of hydrostatic conditions and homogeneity of sample. Therefore, the spatial interpolation of water content along the probe is carried out using unsaturated parametric function (van Genuchten 1980) (See equation (5.3) and (5.4)). Consequently, the parameters to be optimized is significantly reduced for the chosen resolution by using only a few TDR waveforms. This reduces the computation time compared to the methods in which water content is optimized at every node (Heimovaara et al. 2004; Laloy et al. 2014). In addition, this technique of spatial interpolation can also be used for estimation of water retention parameters for samples with larger heights.

We also measured the water retention parameters of our sample with the evaporation

Table 5.5: Prior summary of the posterior parameter for multi-step drainage experiment.

Parameter	Dataset	Min	Max	Optimum	Measured /Set	Std
α_{wat} [m ⁻¹]	-	3	18	3.8241	-	2.0×10^{-3}
n_{wat} [-]	-	8	40	17.3971	-	0.2042
c_{wat} [-]	-	1.5	3	2.1133	-	2.0×10^{-3}
d_{wat} [-]	-	1.5	3	2.7295	-	2.1×10^{-3}
θ_e [m ³ m ⁻³]	-	0.1	0.7	0.3157	-	8.8×10^{-3}
θ_r [m ³ m ⁻³]	-	0	0.3	0.0408	-	4.2×10^{-2}
θ_s [m ³ m ⁻³]	-	-	-	0.3565 (Eq.(5.12))	0.3678	-
z_{aw} [m]	5	-0.8	-0.1	-0.5498	-0.64	1.8×10^{-4}
$\log_{10}(\sigma_{DCC})$ [S m ⁻¹]	1	-3.5	-1	-1.8753	-	1.57×10^{-4}
	2	-3.5	-1	-1.8426	-	1.47×10^{-4}
	3	-3.5	-1	-1.9059	-	1.66×10^{-4}
	4	-3.5	-1	-2.2161	-	3.82×10^{-4}
	5	-3.5	-1	-2.4871	-	5.19×10^{-5}
σ [-]	1	1×10^{-9}	1×10^3	0.0123	-	6.48×10^{-5}
	2	1×10^{-9}	1×10^3	0.0112	-	6.17×10^{-5}
	3	1×10^{-9}	1×10^3	0.0117	-	6.22×10^{-5}
	4	1×10^{-9}	1×10^3	0.0169	-	8.93×10^{-5}
	5	1×10^{-9}	1×10^3	0.0149	-	7.68×10^{-5}
	6	1×10^{-9}	1×10^3	1.10×10^{-4}	-	5.45×10^{-5}
	7	1×10^{-9}	1×10^3	1.4×10^{-3}	-	0.9544

Table 5.6: Weight of water in sample at first and final step involved in multi-step drainage.

Drainage step	Measured [kg]	Optimized [kg]
1	3.5366	3.5379
5	0.9863	0.9844

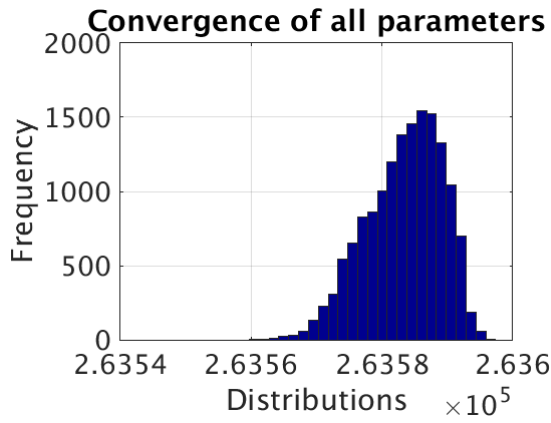


Figure 5.4: Posterior distribution of all parameters.

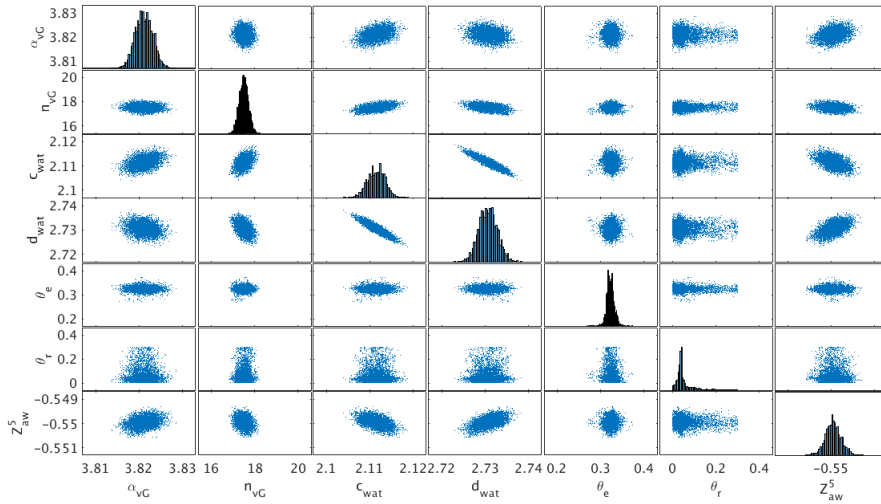


Figure 5.5: Plot matrix of α_{wat} , n_{wat} , c_{wat} , d_{wat} , θ_e , θ_r and z^5_{aw} in posterior distribution.

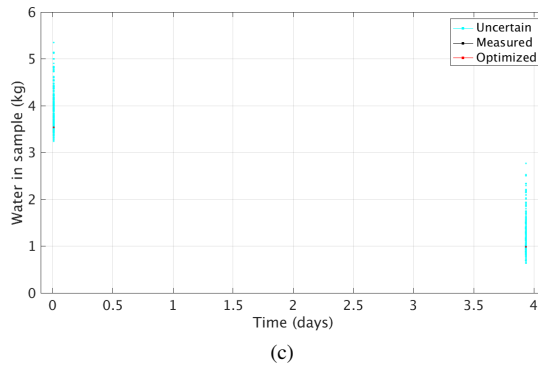
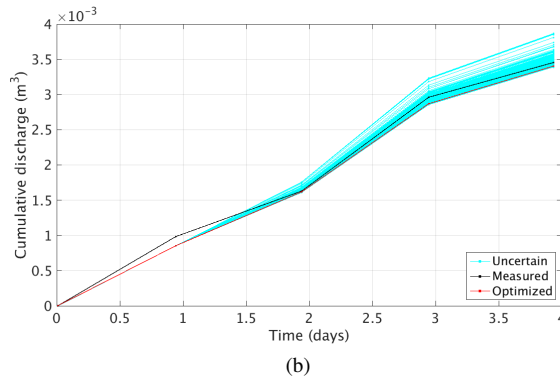
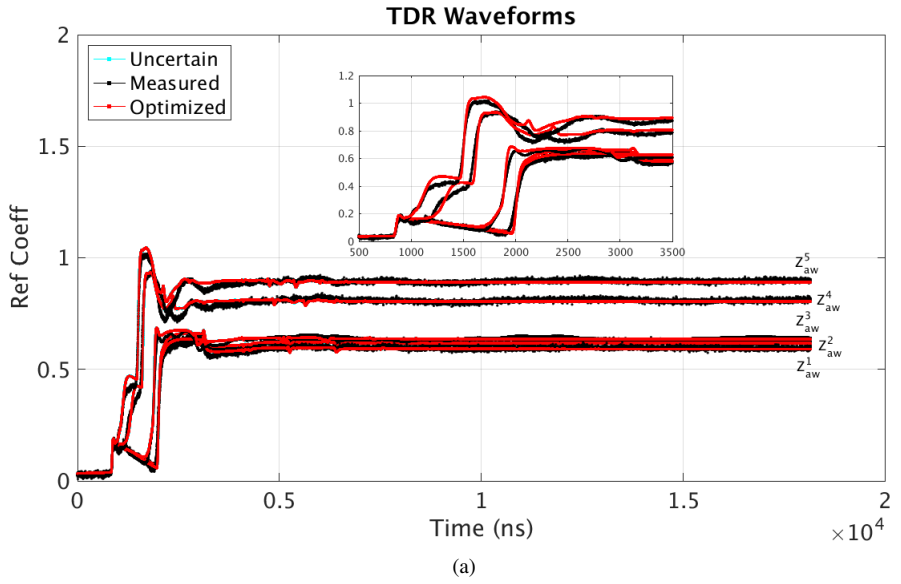


Figure 5.6: Waveforms (a) and cumulative discharge (b) obtained at different z_{aw} boundary heads. Water in sample at first and last step (c).

Table 5.7: Unsaturated parameters for coarse sand obtained using multi-step drainage experiment (MSDE) and those obtained using evaporation method in HYPROP.

Material parameters	MSDE	HYPROP
$\alpha_{wat} [\text{m}^{-1}]$	3.8241	4.3560
$n_{wat} [-]$	17.3971	8.3408
$\theta_r [\text{m}^3 \text{m}^{-3}]$	0.0408	0.1423
$\theta_s [\text{m}^3 \text{m}^{-3}]$	0.3565	0.4135
$a_{wat} [-]$	0.1157	-
$b_{wat} [-]$	-5.7276	-

method using the HYPROP equipment (HYPROP-S UMS). The results of this comparison are summarized in Table 5.7 and figure 5.7. The HYPROP setup, consists of two tensiometers, which are separated by a small distance. Using these two tensiometers, the average value of the pressure head is obtained. This average value is assumed to correspond with the average water content determined by the weight of the complete sample. Our sample is a rather extreme soil type, well sorted with a high saturated hydraulic conductivity and a very non-linear relative hydraulic permeability. As a consequence, evaporation will create a steep profile in the HYPROP experiment. When the water front is below the top tensiometer, this tensiometer will fail, indicating the stop point for the HYPROP analysis. However, in this case the bottom of the sample is still saturated, leading to a severe overestimation of the value of θ_r . The classic approach of averaging the water content along the sample height, fails to address the steep profile of retention curve for our sample. This leads also leads to a smaller value for n_{wat} . The higher value of θ_s in the HYPROP is probably due to is probably caused by the fact that we used a different procedure for compacting the sample in the smaller HYPROP sample holder than we used for the column for the TDR multi-step drainage experiment.

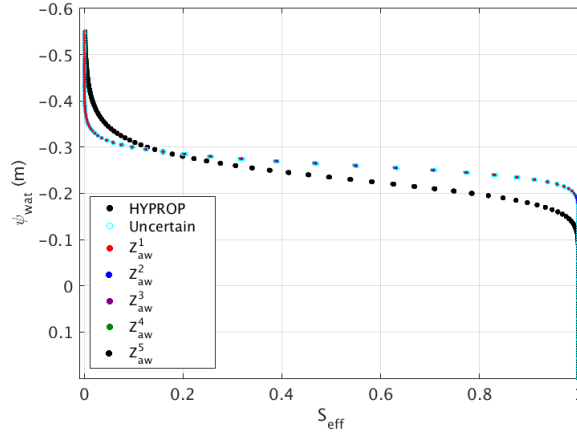


Figure 5.7: Water retention curve for our sand sample.

5.4.4 Model validation of multi-step drainage experiment.

The multi-step drainage experiment was simulated using the Richard's equation using the van Genuchten parameters obtained from the optimized posterior distributions. Figure 5.8(a) shows, the cumulative discharge obtained during the multi-step drainage experiment. The simulated cumulative discharge obtained for the optimal parameter set closely matches the measured cumulative discharge and it lies within the bandwidth of all RE solutions which were sampled from the final distribution of parameters. The water content along the depth of the column obtained after the different drainage steps at hydrostatic equilibrium is shown in figure 5.8(b). Clearly the uncertainty in the estimated value for θ_r is the cause for the wide bandwidth in the last outflow steps which is mainly due to its relatively wide distribution. Clearly in order to improve the TDR analysis more effort has to be applied in order to find an approach to reduce the uncertainty in θ_r . This could be done by applying a thicker filter layer of fine sand at the bottom of the column to ensure a high air entry value. In addition samples could be taken along the TDR probe for gravimetric water content measurements in order to independently measure θ_r .

Figure 5.9, shows the pressure head and water content as a function of time. The pressure head distribution in time clearly indicates that hydrostatic conditions prevail after 24 hours.

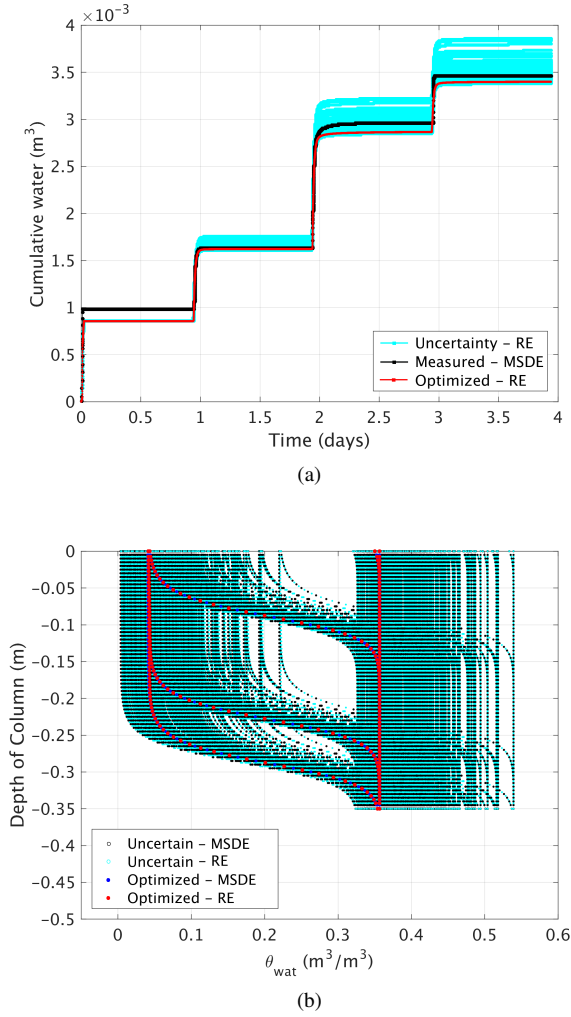
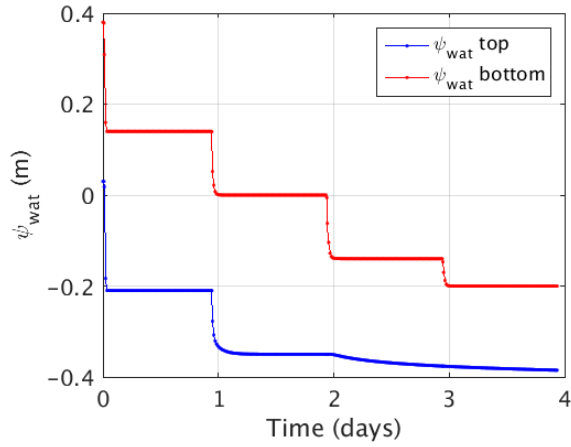
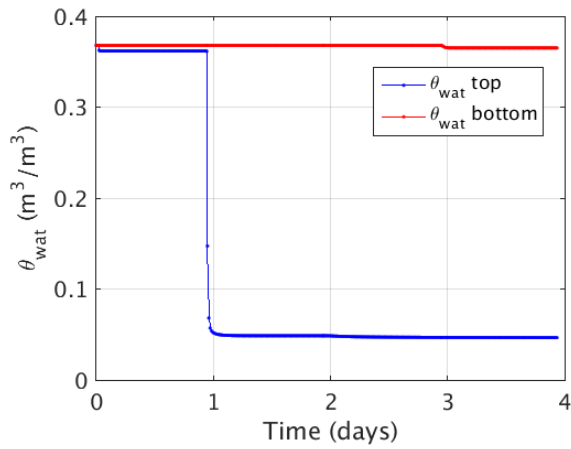


Figure 5.8: Validation of multi-step drainage experiment (MSDE) using flow model of VarSatFT for, cumulative discharge (a) and water content along depth at different hydrostatic conditions (b).



(a)



(b)

Figure 5.9: Pressure head (a) and water content (b) along time duration simulated for multi-step drainage experiment determined using RE solutions.

5.5 Conclusions

In this chapter, we present an efficient approach for measuring the water retention parameters of a soil sample using TDR measurements during hydrostatic conditions. The method is based on the multi-section transmission line approach which accounts for the spatial distribution of the dielectric permittivity along the TDR probe. In order to reduce the number of unknown parameters we interpolate the water content along the probe using the van Genuchten equation. Under hydrostatic conditions the capillary pressures are known everywhere along the probe. Applying this method to a multi-step drainage experiment requires only a few TDR measurements to measure a significant range of capillary pressures and it gives very accurate measurements close to saturation.

A detailed analysis of the posterior marginal probability distributions combined with an uncertainty analysis using numerical simulations of the multi step drainage experiment indicated a significant uncertainty in the residual water content optimized using our approach. This uncertainty can be reduced by performing an independent measurement or by adapting the experimental set-up in order to allow the experiment to be performed a conditions where higher suctions can be applied to the lower boundary of the sample.

Chapter 6

Conclusions

6.1 Overall summary and conclusions

The primary aim of this thesis is to investigate the origin of preferential flow and determine the controlling factors affecting non-equilibrium in transport in heterogeneous porous media with similar properties as those found in waste bodies of Dutch MSW landfills. In order to achieve this aim we combined numerical analysis and lab scale experiments in small scale systems. The hypothesis is that variable infiltration in to heterogeneous unsaturated porous materials leads to preferential flow and as a result non-equilibrium solute transport.

For the numerical experiments we developed a relatively simple 2D simulator as a MATLAB(tm) (MATLAB 2014b) toolbox. We call this simulator Variably Saturated Flow and Transport (VarSatFT). VarSatFT is based on the unsaturated Richards' flow equation coupled to the Advection Dispersion solute transport equation. These coupled equations are solved on a 2D finite difference grid where the mixed form of Richards' equation is solved with the Picard iteration method (Celia et al. 1990a) and the solute transport equation is solved with the slightly modified Eulerian-Lagrangian Marker in Cell approach inspired by Gerya (2010). In order to verify the implementation of VarSatFT we compared the results on a scenario by scenario basis with results obtained with two other Finite Element implementations of the coupled Richards' and ADE problem. One of these solvers was implemented in COMSOL (COMSOL 4.3b) using the default porous media flow and solute transport interfaces, the other was implemented using the open-source MATLAB finite element package FAESOR (Krysl 2010). Because it is relatively easy to adapt the implementation of VarSatFT, we optimized its performance with respect to

water and solute mass balance conservation and reduction of numerical dispersion. This makes VarSatFT a very suitable code for modelling scenarios with extreme heterogeneity in permeability leading to very steep concentration gradients which occur in waste bodies. Based on the initial simulation results a relatively simple small scale 2D laboratory experiment was performed in order to verify the results obtained from the different model scenarios.

The numerical simulations clearly show that the presence of impermeable plastic layers in the porous system increases the tortuosity of streamlines leading to a spread in residence times of water in the porous domain. The solute breakthrough curve becomes wider due to this spread in residence times, however breakthrough as a function of flushed pore volume shows that solute transport occurs under equilibrium conditions. The presence of materials in the porous domain with low permeability (such as clay) also increases the tortuosity of the streamlines, but the solutes present within these materials leach out by diffusion. Solute breakthrough curves for the complete porous domain exhibit flow rate dependent behaviour with a significant tailing which is a clear indication of non-equilibrium processes at the overall scale of the porous domain caused by the diffusion of solutes. High flow rates, lead to low solute concentrations in the discharged leachate, slow flow rates to higher concentrations. Simulations where infiltration is a mixture of high flow, low flow and no flow conditions, led to the most extreme non-equilibrium behaviour in the discharged leachate where in certain scenarios, solute concentrations in the discharge increased at the onset of flow after an extended no-flow period.

The main conclusions from the modelling and experimental work confirm the initial hypothesis, where the origin of preferential flow and non-equilibrium solute transport lies in the combination of highly heterogeneous unsaturated porous media subjected to highly variable infiltration boundary conditions. These conditions do occur in the waste bodies of the majority of Dutch landfills. The waste bodies are unsaturated because of the requirement of having leachate levels which are maximally 1 m above the bottom liner and waste bodies have heights of 10 m and higher. The heterogeneity in waste bodies is caused by the presence of very diverse materials with a large variation of hydraulic properties (big bags filled with asbestos, parcels of news paper, soil remediation residues, mattresses, blocks of wood, food waste in plastic bags, and infrastructure in the waste body such as gas wells). The infiltration boundary condition in the Netherlands is controlled by the meteorological conditions. In the Netherlands rainfall is more or less homogeneous through out the year. Evapo-transpiration is much larger in the summer leading to a net rainfall deficit. In winter we have a rainfall surplus, so infiltration occurs mainly during the winter and during some large rain storms in summer. Leachate concentrations will be higher in the summer because the relatively larger residence time of the water in the landfill due to the slow flow rates.

A main conclusion from this research on the origin for preferential flow and non-equilibrium transport in unsaturated waste material is that leachate quality is mainly controlled by the residence time of the mobile solute in the permeable zone of the landfill. Small volumes of high permeability in waste bodies lead to extreme preferential flow and low solute concentrations in landfill leachate because the time for diffusion of solutes from the polluted bulk of the waste to the relatively clean rainfall dominated mobile water is very small. This is beneficial for long term after-care. However, for treating waste bodies in order to decrease the emission potential we require water to reach as much of the waste body as possible. In addition because leachate is collected and treated, maximum mass removal also requires a more homogeneous flow condition so leachate concentrations are as high as possible. Increasing the average water content of the waste body by infiltration of water and recirculation of leachate leads to less extreme differences in permeabilities of the materials in the waste body because these differences are more extreme for dry materials due to the non-linear dependence of the relative permeability on water content. In addition, recirculation increases the residence time of the leachate in the waste body.

A secondary aim of the research was to develop a methodology for accurate measurement of the parameters in the water retention curve of well sorted granular materials near saturation. The available techniques in our laboratory gave results with a large uncertainty. We developed a multi-step drainage experiment where the water content along a vertically installed TDR-probe is used to inversely model (Heimovaara et al. 2004) the parameters of the water retention curve (van Genuchten 1980). The approach where TDR waveforms acquired at the hydrostatic conditions after a series of drainage steps are inversely modelled adjusting the parameters of the water retention curve using the DREAM_{ZS} Bayesian inversion scheme proved to be very effective and straightforward. With this approach we are able to measure the water retention curve from saturation to a suction of about -2 m ($pF = 2.3$) using measurements of the TDR waveform of a vertically installed probe in the sample. The suction is obtained assuming hydrostatic conditions at the end of a drainage step and measuring the height of the outflow port. For successful measurements it is important to keep the drainage system fully saturated.

Appendix A

In both COMSOL and FAESOR, Galerkin method (Smith and Griffiths 2004) is used to evaluate finite element approximation for the flow and solute transport equations. The domain divided into an equivalent system of quadratic triangular elements, has six basis functions formulated in terms of η and ξ .

Where $[N] = \begin{bmatrix} (\eta + \xi - 1)(2\eta + 2\xi - 1) \\ \xi(2\xi - 1) \\ \eta(2\eta - 1) \\ -4\xi(\eta + \xi - 1) \\ 4\eta\xi \\ -4\eta(\eta + \xi - 1) \end{bmatrix}$. In Figure A.1, the values of coordinates η and ξ are shown in brackets near to their node number.

A.1 FEM discretization of water transport model

The ψ -based form of RE can be written as (Celia et al. 1990a; Pinder and Celia 2006; Shahraiyini and Ashtiani 2012) as shown in equation (A.1) in which $\mathbf{C} = [C_m(\psi) + S_w S_s]$

$$\mathbf{C} \frac{\partial \psi}{\partial t} - \nabla \cdot \mathbf{K} [\nabla(\psi + z)] = 0 \quad (\text{A.1})$$

Applying residual to equation (A.1) we get.

$$rB = \mathbf{C} \frac{\partial \psi}{\partial t} - \nabla \cdot \mathbf{K} [\nabla(\psi + z)] \quad (\text{A.2})$$

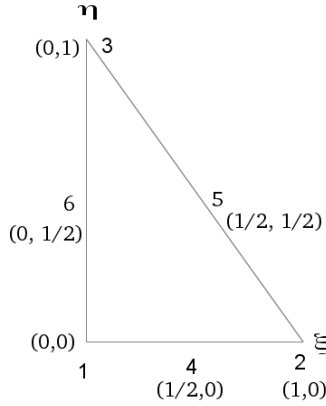


Figure A.1: quadratic triangular element for FEM.

The weighted balance residual reads $\int_V \eta(x) r_B(x, t) dV$. Multiplying by weighted fraction throughout equation (A.2) we get.

$$\int_V \eta C \frac{\partial \psi}{\partial t} dV - \int_V \eta \nabla \cdot \mathbf{K} [\nabla(\psi + z)] dV = 0 \quad (\text{A.3})$$

Considering the second term

$$- \int_V \eta \nabla \cdot \mathbf{K} [\nabla(\psi + z)^T] dV = \int_V \eta \nabla \cdot \mathbf{q} dV \quad (\text{A.4})$$

where is the test function η multiplies the second derivatives of pressure head ψ and z coordinate.

By divergence theorem

$$\int_V \eta \nabla \cdot \mathbf{q} dV = \int_V \nabla(\eta \mathbf{q}) dV - \int_V (\nabla \eta)(\mathbf{q}) dV \quad (\text{A.5})$$

Applying Green's theorem to equation (A.6)

$$\int_V \eta \nabla \cdot \mathbf{q} dV = \int_S \eta \mathbf{q} \cdot \mathbf{n} dS - \int_V (\nabla \eta) \mathbf{q} dV \quad (\text{A.6})$$

where \mathbf{n} is the normal to the surface S , and as $\mathbf{q} \cdot \mathbf{n}$ is known, we can write first term on

right hand side of the surface integral as

$$\int_V \eta \nabla \cdot \mathbf{q} dV = \int_{S_1} \eta \mathbf{q} \cdot \mathbf{n} dS + \int_{S_2} \eta \mathbf{q} \cdot \mathbf{n} dS + \int_{S_3} \eta \mathbf{q} \cdot \mathbf{n} dS - \int_V (\nabla \eta) \mathbf{q} dV \quad (\text{A.7})$$

The integral over the part of the subsurface S_1 is troublesome, because $\mathbf{q} \cdot \mathbf{n}$ is unknown there. We have optioned to vanish η along S_1 , $\int_{S_1} \eta \mathbf{q} \cdot \mathbf{n} dS = 0$, where the test function satisfy $\eta(x) = 0$ for $x \in S_1$. We eliminate the integral over S_1 .

$$\begin{aligned} \int_V \eta \nabla \cdot \mathbf{q} dV &= - \int_V \eta \nabla \cdot [\mathbf{K} \nabla (\psi + z)^T] dV \\ &= \int_{S_2} \eta \mathbf{q} \cdot \mathbf{n} dS + \int_{S_3} \eta \mathbf{q} \cdot \mathbf{n} dS \\ &\quad + \int_V (\nabla \eta) \cdot \mathbf{K} [\nabla (\psi + z)^T] dV \end{aligned} \quad (\text{A.8})$$

The water flux passing through the surface S_2 is known (Neumann boundary condition).

$$\int_{S_2} \underline{\eta} [\underline{q_n} - (\underline{q \cdot n})] dS = 0 \quad (\text{A.9})$$

Similarly on the boundary surface S_3 the boundary condition (Robins boundary condition) with the weighted residual equation.

$$\int_{S_3} \underline{\eta} [K_{surf}(\psi - \psi_{amb}) - (\underline{q \cdot n})] dS = 0 \quad (\text{A.10})$$

Substituting equation (A.9), equation (A.10) into equation (A.3) we get.

$$\begin{aligned} \int_V \eta (C \frac{\partial \psi}{\partial t} - \nabla \cdot \mathbf{K} [\nabla (\psi + z)]) dV \\ + \int_{S_2} \underline{\eta} [\underline{q_n} - (\underline{q \cdot n})] dS \\ + \int_{S_3} \underline{\eta} [K_{surf}(\psi - \psi_{amb}) - (\underline{q \cdot n})] dS \end{aligned} = 0 \quad (\text{A.11})$$

The underlined surface term cancel with the surface integrals in the equation (A.11).

$$\begin{aligned} \int_V \eta C \frac{\partial \psi}{\partial t} dV \\ + \int_V (\nabla \eta) \cdot \mathbf{K} [\nabla (\psi + z)]^T dV \\ + \int_{S_2} \eta \underline{q_n} dS + \int_{S_3} \eta K_{surf}(\psi - \psi_{amb}) dS \end{aligned} = 0 \quad (\text{A.12})$$

where $\eta(x) = 0$ for $x \in S_1$.

A.1.1 Solution technique for water transport model

The trial function will be exposed using the basis functions here (i) means the degree of freedom associated with node i . Therefore for ψ

$$\psi(x, z, t) = \sum_{i=1}^N N_i(x, z) \psi_{(i)}(t) \quad (\text{A.13})$$

We adopt notation $\eta(x, z) = N < i > (x, z)$, $i = 1, \dots, N_f$, where N_f is the number of unknown degrees of freedom, therefore $\psi(x, z, t) = \sum_{i=1}^N N < i > (x, z) \psi_i(t)$

The finite element expansions for the trial and test functions are now substituted into the weighted residual integral equation (A.12). Going term by term we get

$$\int_{S_c} \eta C \frac{\partial \psi}{\partial t} dV = \int_{S_c} N < j > C \sum_{i=1}^N N < i > \frac{\partial \psi}{\partial t} dV, \quad j = 1, \dots, N_f, \quad (\text{A.14})$$

which simplifies to

$$\sum_{i=1}^N \left[\int_{S_c} N < j > C N < i > dV \right] \frac{\partial \psi}{\partial t}, \quad j = 1, \dots, N_f \quad (\text{A.15})$$

The term in the bracket mixes together i and j from two different sets, and some of the degrees of freedom $\frac{\partial \psi}{\partial t}$ are known. By separating the known and unknown quantities we get

$$\begin{aligned} & \sum_{i=1}^N \left[\int_{S_c} N < j > C N < i > dV \right] \frac{\partial \psi}{\partial t} = \\ & \sum_{i=1}^{N_f} \left[\int_{S_c} N < j > C N < i > dV \right] \frac{\partial \psi}{\partial t} + \\ & \sum_{i=N_f+1}^N \left[\int_{S_c} N < j > C N < i > dV \right] \frac{\partial \bar{\psi}}{\partial t}, \quad j = 1, \dots, N_f, \end{aligned} \quad (\text{A.16})$$

We indicate the barred $\frac{\partial \bar{\psi}}{\partial t}$ for $i = N_f + 1, \dots, N$ quantities as prescribed. The first integral on the right-handed side of equation (A.17) suggests defining a square matrix the water capacity matrix.

$$C_{ji} = \int_{S_c} N < j > C N < i > dV, \quad i, j = 1, \dots, N_f, \quad (\text{A.17})$$

This matrix is multiplied by the vector of the unknown degrees of freedom. The integral in the second term will be given a different symbol, since the meaning of the two terms is

different.

$$L_{\bar{C},j} = - \sum_{i=N_f+1}^N \left[\int_{S_c} N < j > \mathbf{C} N < i > dV \right] \frac{\partial \psi}{\partial t}, \quad j = 1, \dots, N_f. \quad (\text{A.18})$$

We will call this the contribution of the prescribed pressure head

The second term in equation (A.13)

$$\begin{aligned} & \int_{S_c} (\nabla \eta) \mathbf{K} [\nabla (\psi + z)]^T dV \\ &= \int_{S_c} (\nabla N < j >) \mathbf{K} (\nabla N < i > (\psi_i + z_i))^T dV \\ &= \sum_{i=1}^{N_f} \left[\int_{S_c} (\nabla N < j >) \mathbf{K} (\nabla N < i >)^T dV \right] \psi_i + \\ & \quad \sum_{i=N_f+1}^N \left[\int_{S_c} (\nabla N < j >) \mathbf{K} (\nabla N < i >)^T dV \right] \bar{\psi}_i + \\ & \quad \sum_{i=N_f+1}^N \left[\int_{S_c} (\nabla N < j >) \mathbf{K} (\nabla z)^T dV \right], \quad j = 1, \dots, N_f, \end{aligned} \quad (\text{A.19})$$

The hydraulic conductivity matrix may be defined as

$$K_{ji} = \int_{S_c} (\nabla N < j >) \mathbf{K} (\nabla N < i >)^T dV, \quad i, j = 1, \dots, N_f, \quad (\text{A.20})$$

The contribution to the pressure head load vector due to the second term on right of equation (A.13), the prescribed pressure head loads reads as

$$L_{\bar{K},j} = - \sum_{i=N_f+1}^N \left[\int_{S_c} (\nabla N < j >) \mathbf{K} (\nabla N < i >)^T \Delta z dS \right] \bar{\psi}, \quad i, j = 1, \dots, N_f. \quad (\text{A.21})$$

The third term is the gravity term which can be written as

$$L_{G,j} = - \sum_{i=N_f+1}^N \left[\int_{S_c} (\nabla N < j >) \mathbf{K} (\nabla z)^T dV \right], \quad j = 1, \dots, N_f. \quad (\text{A.22})$$

where the ∇z represents $\frac{\partial z}{\partial z}$ or equal to unity. Here for 2D term $\nabla z = \begin{bmatrix} 0 & 1 \end{bmatrix}$.

The term corresponding to natural boundary condition i.e. $C_{c,2}$ part of the boundary, the load term results

$$L_{q2,j} = - \int_{C_{c,2}} N < j > \bar{q}_n dC \quad (A.23)$$

The $C_{c,3}$ part of boundary, where the water flux is proportional to the difference between the ambient pressure head and surface pressure head, we get an ambient pressure head load term.

$$L_{q3,j} = - \int_{C_{c,3}} N < j > K_{surf} \psi_{amb} dC, \quad j = 1, \dots, N_f. \quad (A.24)$$

where K_{surf} is the surface permeability and ψ_{amb} is ambient pressure head. The surface pressure head transfer matrix is given as

$$H_{ji} = \int_C N < j > K_{surf} N < i > dC, \quad i, j = 1, \dots, N_f, \quad (A.25)$$

and the respective prescribed load condition is given as

$$L_{\bar{H},j} = - \sum_{i=N_f+1}^N \left[\int_{C_{c,3}} N < j > K_{surf} N < i > dC \right] \psi, \quad j = 1, \dots, N_f. \quad (A.26)$$

The system of ordinary differential equations resulting by summarizing various matrices and load terms, from the introduction of finite element test and trial functions is given as

$$\sum_{i=1}^{N_f} C_{ji} \frac{\partial \psi}{\partial t} + \sum_{i=1}^{N_f} K_{ji} \psi_i + \sum_{i=1}^{N_f} H_{ji} \psi_i = \begin{aligned} &L_{\bar{C},j} + L_{\bar{K},j} + L_{G,j} \\ &+ L_{\bar{H},j} + L_{q2,j} \\ &+ L_{q3,j}, \quad j = 1 \dots N_f \end{aligned} \quad (A.27)$$

We calculated the Darcy velocities using finite difference on the finite difference mesh Desai. Subsequently we then back interpolated them on finite element nodes using linear scatterInterpolant and interp2 function available in MATLAB. The formulation for Darcy

velocities in x and z direction for 2D domain is carried as shown in equation (A.28).

$$\begin{aligned} q_x &= -\mathbf{K}_{xx} \frac{\partial \psi}{\partial x} \\ q_z &= -\mathbf{K}_{zz} \left(\frac{\partial \psi}{\partial z} + 1 \right) \end{aligned} \quad (\text{A.28})$$

A.1.2 Time discretization for water transport model

The ordinary differential equation (A.27) need to be numerically integrated in time. In order to uncluttered the equations we use the matrix notation

For the water capacity matrix

$$\mathbf{C}_m = [C_{ji}], j, i = 1, \dots, N_f \quad (\text{A.29})$$

For the hydraulic conductivity matrix

$$\mathbf{K}_m = [K_{ji}], j, i = 1, \dots, N_f \quad (\text{A.30})$$

For the surface pressure transfer matrix

$$\mathbf{H}_m = [H_{ji}], j, i = 1, \dots, N_f \quad (\text{A.31})$$

The prescribed pressure heads and their rates.

$$\mathbf{L}w_v = [L_{\bar{C},j} + L_{\bar{K},j} + L_{G,j} + L_{\bar{H},j} + L_{q2,j} + L_{q3,j}], j = 1, \dots, N_f \quad (\text{A.32})$$

where subscripts \mathbf{m} denotes square matrix and \mathbf{v} denotes column matrix.

The free pressure heads, and rate of pressures head are collected in column matrices

$$\psi_v = [\psi_j], \frac{\partial \psi}{\partial t}_v = \left[\frac{\partial \psi_j}{\partial t} \right], \text{ free } j. \quad (\text{A.33})$$

Therefore equation (A.27), may be recast as

$$\mathbf{C}_m \frac{\partial \psi}{\partial t}_v + (\mathbf{K}_m + \mathbf{H}_m) \psi_v - \mathbf{L}w_v = 0 \quad (\text{A.34})$$

We have applied the Picard iteration method for converging the nonlinearity (Celia et al. 1990a). By applying Taylor expansion for first term on the left hand side of equation (A.34) we get

$$\theta_i^{a+1,b+1} = \theta_i^{a+1,b} + \frac{\partial \theta_i}{\partial \psi_i} (\psi_i^{a+1,b+1} - \psi_i^{a+1,b}) + \dots (\text{neglecting higher order terms})$$

Here in the formulates b denotes the iteration level. Initially the first iteration ($b = 0$) corresponds to the solution at the previous time level, so that $\psi_i^{a+1,0} - \psi_i^a$, is known, then we initiate the iterative calculation beginning with $b = 0$ and progresses to larger integer values of b until the solution converges.

$$\theta_i^{a+1,b+1} = \theta_i^{a+1,b} + C \delta_i^{b+1} \quad (\text{A.35})$$

where

$$C = \frac{\partial \theta_i}{\partial \psi_i}, \text{ and } \delta_i^{b+1} = (\psi_i^{a+1,b+1} - \psi_i^{a+1,b}) \quad (\text{A.36})$$

Substituting equation (A.36) into equation (A.27) we get

$$\frac{\theta_v^{a+1,b} - \theta_v^a}{\Delta t} + C_m \frac{\delta_v^{b+1}}{\Delta t} + (K_m + H_m) \psi_v - L w_v = 0 \quad (\text{A.37})$$

The storativity and fluid compressibility term can be included along with specific water capacity, such as $C_{ij} = [C_m(h) + S_w S_s]$ in above equation (A.37) and the θ for different iteration level is evaluated using van Genuchten 1980 relations. The first term is can be substituted as $T_{ij}^b = \frac{\theta_{ij}^{a+1,b} - \theta_{ij}^a}{\Delta t}$, therefore,

$$T_v^b + C_m \frac{\delta_v^{b+1}}{\Delta t} + (K_m + H_m) \psi_v - L w_v = 0 \quad (\text{A.38})$$

In order to find unknown δ_v^{b+1} we write equation (A.38) as

$$\delta_v^{b+1} = \left[\left(\frac{C_m}{\Delta t} + (K_m + H_m) \right) \right]^{-1} [- (K_m + H_m) \psi_v^b + L w_v^b - T_v^b] \quad (\text{A.39})$$

From this value we get pressure head of next iteration

$$\psi_v^{a+1,b+1} = \delta_v^{b+1} + \psi_v^{a+1,b} \quad (\text{A.40})$$

In our water flow model we have adopted the automatic time step changing method depending on the flow rates and number of iterations.

$$dt = \min \left(\left(\frac{\theta \Delta x}{q_{xx}}, \frac{\theta \Delta z}{q_{zz}} \right)_{\min} ||\Delta t_{iter}|| \Delta t_{max} \right) \quad (A.41)$$

The time stepping is considered minimum of the time step as calculated in equation (A.41), depending on flow rates, depending on the iteration criteria (niter) i.e. Δt_{iter} set up in equation (A.46), equation (A.53) and equation (A.54). And the predefined maximum constant time step i.e. ($\Delta t_{max} = 5$ s). Where $miniter = 15$, minimum number of iterations, $maxiter = 25$ maximum number of iterations and the coefficients $\mu_1 = 0.25$ and $\mu_2 = 1.1$. If the required number of iteration are smaller than the minimum iterations then time step is increased. In addition if the number of iterations are larger than maximum iterations then the time step used in the numerical solution is decreased.

We have considered $\delta_r = 1 \times 10^{-3}$ and $\delta_a = 1 \times 10^{-3}$, that gives the convergence criteria

$$convcrit = \delta_r |\psi_v^{a+1,b+1}| + \delta_a \quad (A.42)$$

And then the test value is given by

$$testval = |\delta_v^{b+1}| - convcrit \quad (A.43)$$

We calculated equation (A.40) and equation (A.41) within the following loop in which we set initial values of nNotConverged = 0 and Converged = false.

if niter \geq maxiter && (mod(nNotConverged,15) \lnNotConverged==0) then,

$$nNotConverged = nNotConverged + 1 \quad (A.44)$$

$$\Delta t_{iter} = \Delta t \cdot \mu_1 \quad (A.45)$$

$$\psi_v^{a+1,b} = \psi_v^{a+1,b+1} \quad (A.46)$$

$$\theta^{a+1,b} = \theta^{a+1,b+1} \quad (\text{A.47})$$

$$\text{niter} = 0 \quad (\text{A.48})$$

elseif max(testval)<0|| ~mod(nNotConverged,15) && nNotConverged,

$$\text{Converged}=\text{true} \quad (\text{A.49})$$

if nNotConverged>=15,

$$\text{TotNotConverged} = \text{TotNotConverged} + 1 \quad (\text{A.50})$$

end

$$\text{nNotConverged} = 0 \quad (\text{A.51})$$

$$t = t + \Delta t \quad (\text{A.52})$$

if $niter < miniter$

$$\Delta t_{iter} = \Delta t \cdot \mu_2 \quad (\text{A.53})$$

else if $niter \geq maxiter$

$$\Delta t_{iter} = \Delta t \cdot \mu_1 \quad (\text{A.54})$$

end

end

In COMSOL, highly nonlinear Newton iteration process is used with maximum iteration of 25 and with $\delta = 1e - 3$ and with automatic time stepping process during solving same coupled problem.

Note: (COMSOL/Study1/SolverConfigurations/Solver1/TimeDependentSolver1/FullyCoupled/Automatic(Newton))

A.2 FEM discretization of solute transport model

The advection dispersion equation is given as.

$$\theta \frac{\partial c}{\partial t} - \nabla \cdot [\mathbf{D} \nabla c - \mathbf{q}c] = 0 \quad (\text{A.55})$$

Applying the residual to it, we get.

$$r_B = \theta \frac{\partial c}{\partial t} - \nabla \cdot \mathbf{D}(\nabla c - \mathbf{q}c) \quad (\text{A.56})$$

The weighted balance residual reads $\int_V \eta(x) r_B(x, t) dV$. By multiplying weighted fraction throughout equation (A.55) we get

$$\int_V \eta \theta \frac{\partial c}{\partial t} dV - \int_V \eta \nabla \cdot \mathbf{D}(\nabla c - \mathbf{q}c) dV = 0 \quad (\text{A.57})$$

In the second term the test function η multiplies both first and second derivatives of concentration c .

$$- \int_V \eta \nabla \cdot \mathbf{D}[\nabla c^T - \mathbf{q}c^T] dV = \int_V \eta \nabla \cdot \mathbf{u} dV \quad (\text{A.58})$$

By divergence theorem

$$\int_V \eta \nabla \cdot \mathbf{u} dV = \int_V \nabla \cdot (\eta \mathbf{u}) dV - \int_V (\nabla \cdot \eta)(\mathbf{u}) dV \quad (\text{A.59})$$

Applying Green's theorem

$$\int_V \eta \nabla \cdot \mathbf{u} dV = \int_S \eta \mathbf{u} \cdot \mathbf{n} dS - \int_V (\nabla \cdot \eta) \mathbf{u} dV \quad (\text{A.60})$$

Since $\mathbf{u} \cdot \mathbf{n}$ is known on top and bottom edges of the domain, we split the surface

integral into one for each sub-surface,

$$\int_V \eta \nabla \cdot \mathbf{u} dV = \int_{S_1} \eta \mathbf{u} \cdot \mathbf{n} dS + \int_{S_2} \eta \mathbf{u} \cdot \mathbf{n} dS + \int_{S_3} \eta \mathbf{u} \cdot \mathbf{n} dS - \int_V (\nabla \cdot \eta) \mathbf{u} dV \quad (\text{A.61})$$

The integral over the part of the subsurface S_1 is troublesome, because $\mathbf{q} \cdot \mathbf{n}$ is unknown there. We have optioned to vanish η along S_1 , $\int_{S_1} \eta \mathbf{q} \cdot \mathbf{n} dS = 0$, where the test function satisfy $\eta(x) = 0$ for $x \in S_1$. We eliminate the integral over S_1 . And as we do not required Neumann boundary conditions for our numerical problem we also eliminate the integral over S_2 .

$$\begin{aligned} \int_V \eta \nabla \cdot \mathbf{u} dV &= - \int_V \eta \nabla \cdot [\mathbf{D} \nabla(c)^T - \mathbf{q} c^T] dV \\ &= \int_{S_3} \eta \mathbf{u} \cdot \mathbf{n} dS \\ &+ \int_V (\nabla \cdot \eta) \theta \mathbf{D} [\nabla(c)^T - \mathbf{q} c^T] dV \end{aligned} \quad (\text{A.62})$$

The boundary surface S_3 (i.e. Robbins boundary condition) we attempt to satisfy the boundary condition with the weighted residual equation as

$$\int_{S_3} \underline{\eta} [qc - (\underline{u} \cdot \underline{n})] dS = 0 \quad (\text{A.63})$$

Finally substituting equation (A.54) into equation (A.50) we get,

$$\int_v \eta \theta \frac{\partial c}{\partial t} - \nabla \cdot \mathbf{D} [\nabla c - \mathbf{q} c] dV + \int_{S_3} \underline{\eta} [qc - (\underline{u} \cdot \underline{n})] dS = 0 \quad (\text{A.64})$$

The underlined surface term cancel with the surface integrals in the equation (A.52)

$$\int_V \eta \theta \frac{\partial c}{\partial t} dV + \int_V (\nabla \cdot \eta) \mathbf{D} [\nabla(c^T) - \mathbf{q} c^T] dV + \int_{S_3} \eta \mathbf{q} c dS = 0 \quad (\text{A.65})$$

where $\eta(x) = 0$ for $x \in S_1$.

The Dirichlet boundary condition (i.e for c_{top}) is applied directly to the nodes situated at the top horizontal edge of the domain.

A.2.1 Solution technique for solute transport model

The trial function will be exposed using the basis functions here (i) means the degree of freedom associated with node i . Therefore for c

$$c(x, z, t) = \sum_{i=1}^N N_i(x, z) c_{(i)}(t) \quad (\text{A.66})$$

The finite element expansions for the trial and test functions are now substituted into the weighted residual integral equation (A.64). We go term-by-term

$$\int_{S_c} \eta \theta \frac{\partial c}{\partial t} dV = \int_{S_c} N < j > \theta \sum_{i=1}^N N < i > \frac{\partial c}{\partial t} dV, \quad j = 1, \dots, N_f, \quad (\text{A.67})$$

which simple to

$$\sum_{i=1}^N \left[\int_{S_c} N < j > \theta N < i > \Delta z dS \right] \frac{\partial c}{\partial t}, \quad j = 1, \dots, N_f, \quad (\text{A.68})$$

The term in the bracket mixes together i and j from two different sets, and some of the degrees of freedom $\frac{\partial c}{\partial t}$ are known. Therefore, separating the known and unknown quantities.

$$\begin{aligned} & \sum_{i=1}^N \left[\int_{S_c} N < j > \theta N < i > dV \right] \frac{\partial c}{\partial t} = \\ & \sum_{i=1}^{N_f} \left[\int_{S_c} N < j > \theta N < i > dV \right] \frac{\partial c}{\partial t} \\ & + \sum_{i=N_f+1}^N \left[\int_{S_c} N < j > \theta N < i > dV \right] \frac{\partial \bar{c}}{\partial t}, \quad j = 1, \dots, N_f, \end{aligned} \quad (\text{A.69})$$

We indicate by the barred $\frac{\partial \bar{c}}{\partial t}$ for $i = N_f + 1, \dots, N$ quantities as prescribed. The first integral on the left-handed side of equation (A.64) suggests defining a square matrix

$$T_{ji} = \int_{S_c} N < j > \theta N < i > dV, \quad i, j = 1, \dots, N_f, \quad (\text{A.70})$$

Where T_{ji} is the is mass matrix containing scalar θ values. This matrix is multiplied by the vector of the unknown degrees of freedom.

The integral in the second term will be given a different symbol, since the meaning of

the two terms is different. We define

$$L_{T,j} = - \sum_{i=N_f+1}^N \left[\int_{S_c} N < j > \theta N < i > dV \right] \frac{\partial c}{\partial t}, \quad j = 1, \dots, N_f. \quad (\text{A.71})$$

as a contribution to a concentration load.

Next, the second term in equation (A.64)

$$\begin{aligned} \int_{S_c} (\nabla \cdot \eta) [\mathbf{D} \nabla c^T - qc^T] dV &= \int_{S_c} \{ (\nabla \cdot \eta) [\mathbf{D} \nabla c^T dV] - (\nabla \eta) [qc^T dV] \} = \\ \int_{S_c} \{ (\nabla N < j >) \mathbf{D} (\nabla N < i > c^T dV - (\nabla N < j >) q (N < i > c^T dV) \} &= \\ \sum_{i=1}^{N_f} \left[\int_{S_c} (\nabla N < j >) \mathbf{D} (\nabla N < i >)^T dV - (\nabla N < j >) q (N < i >)^T dV \right] c_i &= \\ \sum_{i=N_f+1}^N \left[\int_{S_c} (\nabla N < j >) \mathbf{D} (\nabla N < i >)^T dV - (\nabla N < j >) q (N < i >)^T dV \right] \bar{c}_i &= \end{aligned} \quad (\text{A.72})$$

The combined dispersion and advection matrix is defined as

$$DA_{ji} = \frac{\int_{S_c} (\nabla N < j >) \mathbf{D} (\nabla N < i >)^T dV}{-(\nabla N < j >) q (N < i >)^T dV}, \quad i, j = 1, \dots, N_f \quad (\text{A.73})$$

The contribution to the concentration load vector due to the second term on right of equation (A.62) reads as

$$\begin{aligned} L_{DA,j} &= \frac{- \sum_{i=N_f+1}^N \left[\int_{S_c} [(\nabla N < j >) \mathbf{D} (\nabla N < i >)^T dV - (\nabla N < j >) q (N < i >)^T dV] \bar{c}_i}{, \quad i, j = 1, \dots, N_f} \end{aligned} \quad (\text{A.74})$$

The $C_{c,3}$ part of the boundary, the concentration gradients is zero i.e and the prescribed concentration and their rates used for equation $\nabla c = 0$, the solute flux is proportional to only advection flux i.e qc .

$$L_{q3,j} = - \int_{C_{c,3}} N < j > qc dC, \quad j = 1, \dots, N_f \quad (\text{A.75})$$

To summarize, various matrices and load terms, the system of ordinary differential equations that results from the introduction of the finite element test and trial functions reads as

$$\sum_{i=1}^{N_f} T_{ji} \frac{\partial c}{\partial t} + \sum_{i=1}^{N_f} DA_{ji} c_i = L_{\bar{T},j} + L_{D\bar{A},j} + L_{q3,j} = 1 \dots N_f \quad (\text{A.76})$$

A.2.2 Time discretization for solute transport model

The advection dispersion equation (A.76) need to be numerically integrated in time. In order to uncluttered the equations we use the matrix notation, with the following symbols:

For the theta matrix

$$\mathbf{T}_v = [T_{ji}] , j, i = 1, \dots, N_f \quad (\text{A.77})$$

For the combined dispersion advection matrix

$$\mathbf{DA}_m = [DA_{ji}] , j, i = 1, \dots, N_f \quad (\text{A.78})$$

The free concentration, and rate of concentration are collected in column matrices

$$\mathbf{Ls}_v = [L_{\bar{T},j} + L_{D\bar{A},j} + L_{q2,j} + L_{q3,j}] , j = 1, \dots, N_f \quad (\text{A.79})$$

$$\mathbf{Con}_v = [c_j] , \mathbf{Con}_v \cdot = \left[\frac{\partial c_j}{\partial t} \right] , \text{ free } j \quad (\text{A.80})$$

and the prescribed concentration and their rates used for equation

$$\bar{\mathbf{C}}\mathbf{on}_v = [c_j] , \mathbf{C}\bar{\mathbf{on}}_v \cdot = \left[\frac{\partial \bar{c}_j}{\partial t} \right] , \text{ free } j \quad (\text{A.81})$$

Therefore equation (A.75) may be recast as

$$\mathbf{T}_v \mathbf{Con}_v \cdot + (\mathbf{DA}_m) \mathbf{Con}_v - \mathbf{Ls}_v = 0 \quad (\text{A.82})$$

The generalized trapezoidal method proposes to express the relationship between the concentrations and the rates of the concentrations at two different time instants, t_a and t_{a+1} , as (See Figure (A.2)),

$$\beta \dot{Con}_{v_{a+1}} + (1 - \beta) \dot{Con}_{v_a} = \frac{Con_{v_{a+1}} - Con_{v_a}}{\Delta t} \quad (A.83)$$

equation (A.82) is applied to the time stepping of equation (A.81) by writing it at the two time instants, t_a and t_{a+1} and then mixing together these two equations. Thus we add them together.

$$\beta [T_v \dot{Con}_{v_{a+1}} + (DA_m) Con_{v_{a+1}} - Ls_{v_{a+1}}] \quad (A.84)$$

and

$$(1 - \beta) [T_v \dot{Con}_{v_a} + (DA_m) Con_{v_a} - Ls_{v_a}] = 0 \quad (A.85)$$

Combining equation (A.75), equation (A.83), equation (A.84) we get,

$$\left[\frac{1}{\Delta t} T_v + \beta (DA_m) \right] Con_{v_{a+1}} = \frac{1}{\Delta t} T_v + (1 - \beta) (DA_m) Con_{v_a} + \beta Ls_v + (1 - \beta) Ls_v \quad (A.86)$$

Using Euler backward implicit method we substitute $\beta = 1$

$$\left[\frac{1}{\Delta t} T_v + DA_m \right] Con_{v_{a+1}} = \left[\frac{1}{\Delta t} T_v \right] Con_{m_a} + Ls_{v_{a+1}} \quad (A.87)$$

In FAESOR for solute transport model we have used predefined fixed time step of $\Delta t = 5$ s. We have used MATLAB (2014b) inbuilt ordinary differential equation solver named ode15s which is a implicit backward Euler method based on description shown in equation (A.81) - equation (A.86). Whereas in COMSOL the time steps for solute transport model were similar as respective water flow model as it is simulated simultaneously.

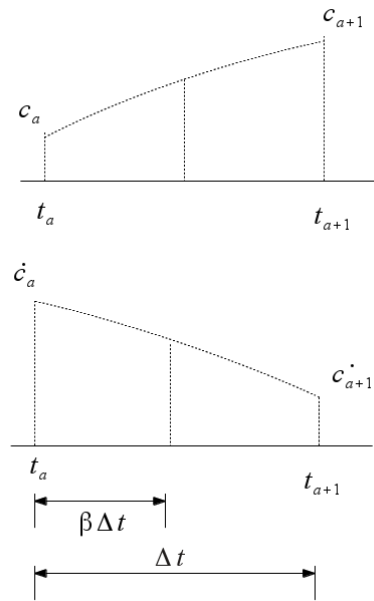


Figure A.2: Illustration of the equation (A.82).

Appendix B

In VarSatFT toolbox, the two-dimensional (2D) numerical approximation of Richards' equation (RE) for water flow and advection dispersion equation (ADE) for solute transport formulated by Eulerian-Lagrangian method is carried out on a finite difference grid. The discretization of water flow and solute transport is explained in following sections.

B.1 Finite difference approximation of Water Flow

The θ -form of RE in finite discretized form is written as shown in equation (B.1), which eventually is converted as mixed-form of RE in following.

$$\frac{\theta_{ij}^{a+1,b+1} - \theta_{ij}^a}{\Delta t} = -\frac{q_{z_{i+1/2}} - q_{z_{i-1/2}}}{\Delta z_{i-1/2}} - \frac{q_{x_{i+1/2}} - q_{x_{i-1/2}}}{\Delta x_{i-1/2}} \quad (\text{B.1})$$

where q_z and q_x are fluxes in z and x directions. i and j are indexes of nodes in z and x direction.

By applying Taylor expansion for first term on the left hand side of equation (B.1), we get.

$$\theta_{ij}^{a+1,b+1} = \theta_{ij}^{a+1,b} + \frac{\partial \theta_{ij}}{\partial h_{ij}} (\psi_{ij}^{a+1,b+1} - \psi_{ij}^{a+1,b}) + \dots (\text{neglecting higher terms})$$

$$\theta_{ij}^{a+1,b+1} = \theta_{ij}^{a+1,b} + C \delta_{ij}^{m+1} \quad (\text{B.2})$$

where $\delta_{ij}^{b+1} = (\psi_{ij}^{a+1,b+1} - \psi_{ij}^{a+1,b})$, $C_m = \frac{\partial \theta_{ij}}{\partial \psi_{ij}}$, a is time level and b is iteration level. We include the water saturation and specific storage coefficient along with specific water

capacity, as $C = C_m(\psi_{ij}) + S_w S_s$ in equation (B.2) (See equation (B.3)).

$$\frac{\theta_{ij}^{a+1,b} - \theta_{ij}^a}{\Delta t} + \frac{C(\psi_{ij}^{a+1,b}) + S_w S_s}{\Delta t} \delta_{ij}^{b+1} = \frac{-\frac{qz_{i+1/2,j} - qz_{i-1/2,j}}{\Delta z_{i-1/2,j}} - \frac{qx_{i,j+1/2} - qx_{i,j-1/2}}{\Delta x_{i,j-1/2}}}{\Delta x_{i,j-1/2}} \quad (\text{B.3})$$

equation (B.3) is solved to determine unknown δ_{ij} , which can further be used to find the converged ψ_{ij} .

For further simplifications, of the left hand side (LHS) of equation (B.3) we get equation (B.4).

$$LHS = \frac{\theta_{ij}^{a+1} - \theta_{ij}^a}{\Delta t} + \frac{C}{\Delta t} \delta_{ij}^{b+1} = \mathbf{T}_v + \mathbf{C}_m \delta_v^{b+1} \quad (\text{B.4})$$

The fluxes in equation (B.3) can be represented in terms of hydraulic conductivities ($\mathbf{K} = k_r \mathbf{K}_{sat}$). Therefore on simplification of the right hand side (RHS) of equation (B.3), we get equation (B.5). The Neumann and Robins boundary conditions are incorporated in the right hand side of equation (B.5).

$$\begin{aligned} RHS &= -\frac{qz_{i+1/2,j} - qz_{i-1/2,j}}{\Delta z_{i-1/2,j}} - \frac{qx_{i,j+1/2} - qx_{i,j-1/2}}{\Delta x_{i,j-1/2}} \\ &= \frac{Kx_{i,j-1/2}}{\Delta x_{i,j-1/2} \Delta x_{i,j-1}} \psi_{i,j-1} + \frac{Kz_{i-1/2,j}}{\Delta z_{i-1/2,j} \Delta z_{i-1,j}} \psi_{i-1,j} \\ &\quad - \left(\frac{Kz_{i+1/2,j}}{\Delta z_{i-1/2,j} \Delta z_{i,j}} + \frac{Kz_{i-1/2,j}}{\Delta z_{i-1/2,j} \Delta z_{i-1,j}} + \frac{Kx_{i,j+1/2}}{\Delta x_{i,j-1/2} \Delta x_{i,j}} + \frac{Kx_{i,j-1/2}}{\Delta x_{i,j-1/2} \Delta x_{i,j-1}} \right) \psi_{i,j} \\ &\quad + \frac{Kz_{i+1/2,j}}{\Delta z_{i-1/2,j} \Delta z_{i,j}} \psi_{i+1,j} + \frac{Kx_{i,j+1/2}}{\Delta x_{i,j-1/2} \Delta x_{i,j}} \psi_{i,j+1} + \frac{Kz_{i+1/2,j}}{\Delta z_{i-1/2,j}} - \frac{Kz_{i-1/2,j}}{\Delta z_{i-1/2,j}} \\ &= \mathbf{K}_m \psi_v^{a+1,b+1} + \mathbf{Y}_v \end{aligned} \quad (\text{B.5})$$

where \mathbf{K}_m is Jacobian matrix of hydraulic conductivity, ψ_v and \mathbf{Y}_v are column matrices. Therefore from equation (B.4) and equation (B.5) we get equation (B.6).

$$\mathbf{T}_v + \mathbf{C}_m \delta_v^{b+1} = \mathbf{K}_m \left[\delta_v^{b+1} + \psi_v^{a+1,b} \right] + \mathbf{Y}_v \quad (\text{B.6})$$

The implicit formulation can be written as equation (B.7).

$$[\mathbf{C}_m - \mathbf{K}_m] \delta_v^{b+1} = \mathbf{K}_m \psi_v^{a+1,b} + \mathbf{Y}_v - \mathbf{T}_v \quad (\text{B.7})$$

and therefore

$$\delta_v^{b+1} = [C_m - K_m]^{-1} [K_m \psi_v^{a+1,b} + Y_v - T_v] \quad (\text{B.8})$$

From equation (B.8) unknown value of δ^{b+1} can be determined and utilized further get pressure head for next iteration (See equation (B.9)).

$$\psi_v^{a+1,b+1} = \delta_v^{b+1} + \psi_v^{a+1,b} \quad (\text{B.9})$$

For convergence criteria and the automatic time stepping were carried out as similar to that described in Shahraiyini and Ashtiani (2012).

B.1.1 Surface ponding

When the infiltration flux (q_{top} , flux infiltrating at the top nodes) is greater than the infiltration capacity ($q_{IC} = K_{sat} k_r(\psi_{top})$; ψ_{top} is pressure head at the top nodes) water gets ponded (accumulated at the top edge). The ponding effect explained as surface water balance is shown in equation (B.10).

$$\frac{d\psi_{pond}}{dt} = q_{top} - q_{IC} \quad (\text{B.10})$$

In our implementation surface ponding occurs when pressure head at the top nodes is greater than zero. Thus simplifying equation (B.10), we get

$$\frac{d\psi_{pond}}{dt} = q_{top} - q_{IC} \approx \frac{d\psi(x, 0, t)}{\Delta z IN_{top} dt} \quad (\text{B.11})$$

where, zIN_{top} is the inter-node situated at the top edge. The term $\frac{d\psi(x, 0, t)}{\Delta z IN_{top}}$ is equivalent to term $d\theta(x, 0, t)$, which is the ponding water accumulated on the surface.

At $\psi(x, 0, t) > 0$, the equation (B.11) can be substituted in θ -form of RE as shown in equation (B.1). Equation (B.1) can be simplified to formulate the mixed-form of RE as shown in equation (B.3).

$$\frac{\partial \theta}{\partial t} + \frac{\partial \psi(x, 0, t)}{\Delta z IN_{top} \partial t} + \nabla \cdot \mathbf{q} = 0 \quad (\text{B.12})$$

When ponding occurs, the velocity for the top nodes is re-calculated as shown in equation

(B.13)

$$q_{new} = -\mathbf{K}_{sat} k_r(\psi_{(top-1/2)}) \left[\frac{\psi_{top} - \psi_{top-1}}{\Delta z_{(top-1)}} + 1 \right] \quad (\text{B.13})$$

where Δz and Δz_{IN} are gradients for nodes and inter-nodes.

During ponding, the Neumann boundary condition is switched to Dirichlet boundary condition by applying the ψ_{top} on the top nodes. This is done by changing the diagonal entries in matrix \mathbf{K}_m denoting top edge elements to -1 and changing the rest entries in matrix \mathbf{K}_m denoting top edge elements to 0. The entries of \mathbf{Y}_v matrix denoting the top edge elements are changed to ψ_{top} .

B.2 Eulerian-Lagrangian formulation for Solute Transport

In Eulerian-Lagrangian formulation for ADE implemented in VarSatFT, solves the dispersion on Euler nodes, and the sub-grid diffusion followed by the advection on Lagrangian markers using modified Marker-in-Cell (MIC).

The effective value of the parameters (B) like θ , c , and the x and z components of D , and v distributed on the markers (mrk) can be calculated using first order bilinear interpolation as shown in equation (B.14) (See Figure B.1(a)).

$$B_{mrk} = \begin{aligned} & B_{i,j} \left(1 - \frac{\Delta x_{mrk}}{\Delta x}\right) \left(1 - \frac{\Delta z_{mrk}}{\Delta z}\right) + B_{i,j+1} \frac{\Delta x_{mrk}}{\Delta x} \left(1 - \frac{\Delta z_{mrk}}{\Delta z}\right) \\ & + B_{i+1,j} \left(1 - \frac{\Delta x_{mrk}}{\Delta x}\right) \frac{\Delta z_{mrk}}{\Delta z} + B_{i+1,j+1} \frac{\Delta x_{mrk}}{\Delta x} \frac{\Delta z_{mrk}}{\Delta z} \end{aligned} \quad (\text{B.14})$$

The advected material properties are interpolated from the displaced markers to the Eulerian grid at every time step. First order accurate bilinear scheme as shown in equation (B.15) is used to calculate an interpolated value of $B_{(i,j)}$ for the i - j -th node using values (B_{mrk}) assigned to all markers found in the four surrounding cells (See Figure B.1(b)).

$$B_{i,j} = \frac{\sum_{mrk} B_{mrk} w_{mrk(i,j)}}{\sum_{mrk} w_{mrk(i,j)}} \quad (\text{B.15})$$

$$w_{mrk(i,j)} = \left(1 - \frac{\Delta x_{mrk}}{\Delta x}\right) \times \left(1 - \frac{\Delta z_{mrk}}{\Delta z}\right)$$

The interpolation of concentration from markers to nodes is mass based. The $w_{mrk} =$

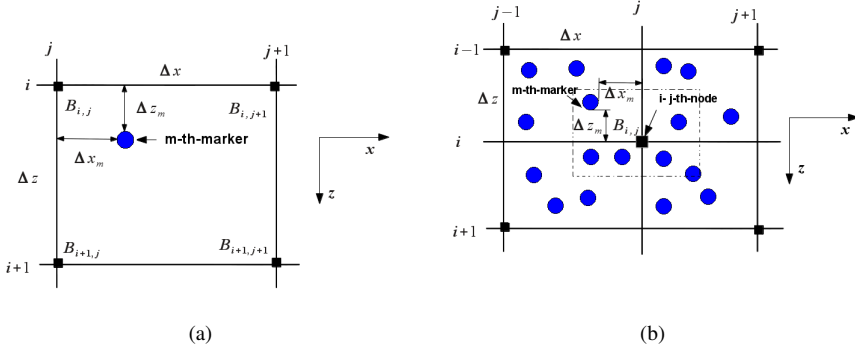


Figure B.1: 2D grid used for interpolation of physical properties from nodes to markers (a). 2D grid used for interpolation of physical properties from the markers to nodes (b), the dashed boundary indicates the area from which markers are used for interpolating properties to node (i, j) (Figures from Gerya 2010).

θ_{mrk} , thus improvising Eq (B.15) as equation (B.16).

$$c_{i,j} = \frac{\sum_{mrk} c_{mrk} \theta_{mrk}(i,j)}{\sum_{mrk} \theta_{mrk}(i,j)} \quad (\text{B.16})$$

The dispersion term discretized on Eulerian nodes is shown in equation B.17.

$$\nabla D \theta \nabla c = \frac{((-[(D\theta)_{z_{i+1/2,j}} \frac{c_{i+1,j} - c_{i,j}}{\Delta z_{i,j}}]) - (-[(D\theta)_{z_{i-1/2,j}} \frac{c_{i,j} - c_{i-1,j}}{\Delta z_{i-1,j}}]))}{\Delta z_{i-1/2,j}} \quad (\text{B.17})$$

$$- \frac{((-[(D\theta)_{x_{i,j+1/2}} \frac{c_{i,j+1} - c_{i,j}}{\Delta x_{i,j}}]) - (-[(D\theta)_{x_{i,j-1/2}} \frac{c_{i,j} - c_{i,j-1}}{\Delta x_{i,j-1}}]))}{\Delta x_{i,j-1/2}}$$

Boundary conditions of ADE are applied in equation (B.17). The equation (B.17) is computed using MATLAB inbuilt ordinary differential equation solver named ode15s to obtained $c_{i,j}$.

The changes in effective concentration field for the Eulerian nodes are calculated as equation (B.18).

$$\Delta c_{i,j} = c_{i,j}^{t+\Delta t} - c_{i,j}^t \quad (\text{B.18})$$

The corresponding concentrations increments for the markers (Δc_{mrk}) obtained by interpolating from the nodes (See equation (B.18)) using equation B.14 in order to calcu-

late new marker concentrations $c_{mrk}^{t+\Delta t}$ is shown in equation (B.19)

$$c_{mrkId}^{t+\Delta t} = c_{mrkId}^t + \Delta c_{mrkId} \quad (B.19)$$

where $Id = (Idx - 1) \cdot \sum zN + Idz$, in which Idx is index of x_{mrk} ,

Idz is index of z_{mrk} and Id is index used to identify location of θ_{mrk} and c_{mrk} .

This interpolation of the calculated concentration changes from the Eulerian nodal points, to the Lagrangian markers reduces numerical diffusion in very efficient manner.

The incremental update scheme in equation (B.19) produces small-scale variations on a sub-grid scale. Sub-grid diffusion operation is the way to damp this variations (Gerya 2010). To define this operation, the concentration changes computed in equation (B.19) are decompose into sub-grid part $\Delta c_{i,j}^{subgrid}$ and remaining part $\Delta c_{i,j}^{remaining}$ as shown in equation (B.20).

$$\Delta c_{i,j} = \Delta c_{i,j}^{subgrid} + \Delta c_{i,j}^{remaining} \quad (B.20)$$

In the sub-grid part, sub-grid diffusion is applied on the markers over a characteristic local concentration diffusion time scale Δt_{diff} (See equation (B.21)) and then interpolated the respective concentration changes back to nodes using equation (B.15).

$$\Delta c_{mrkId}^{subgrid} = c_{mrk(i,j)Id}^t - c_{mrkId}^t \left[1 - \exp \left(-d \frac{\Delta t}{\Delta t_{diff}} \right) \right] \quad (B.21)$$

$$\Delta t_{diff} = \frac{1}{(2D_{xmrk}/\Delta x IN_{Idx}^2 + 2D_{zmrk}/\Delta z IN_{Idz}^2)}$$

where Δt_{diff} is defined for the corresponding cell of the grid where the marker is located, d is a dimensionless numerical diffusion coefficient (values between $0 \leq d \leq 1$) (we choose $d = 0.75$). The $c_{mrk(i,j)}^t$, D_{xmrk} and D_{zmrk} are interpolated for a given marker, respectively from $c_{i,j}^t$ (See equation (B.18)), $D_{xx(i,i)}$, $D_{zz(j,j)}$ values for nodes using the equation (B.15).

After obtaining $\Delta c_{mrk}^{subgrid}$ for all markers, it is back interpolated to nodes as $\Delta c_{i,j}^{subgrid}$ using equation (B.16). Then the remaining $\Delta c_{i,j}^{remaining}$ is computed for the nodes from equation (B.20) in equation (B.22).

$$\Delta c_{i,j}^{remaining} = \Delta c_{i,j} - \Delta c_{i,j}^{subgrid} \quad (B.22)$$

The new corrected marker concentrations $c_{mrk(corrected)}^{t+\Delta t}$ is computed according to

equation (B.19) which removes the non-physical sub-grid oscillations as shown in equation (B.23).

$$c_{mrk(corrected)Id}^{t+\Delta t} = c_{mrkId}^t + \Delta c_{mrkId}^{subgrid} + \Delta c_{mrkId}^{remaining} \quad (B.23)$$

where $\Delta c_{mrk}^{subgrid}$ is given by equation (B.23) and $\Delta c_{mrk}^{remaining}$ is interpolated from nodal values of $c_{i,j}^{remaining}$ using equation (B.15).

For the advective process, the markers with $c_{mrk(corrected)}^{t+\Delta t}$ concentrations are advected using equation (B.24).

$$\begin{aligned} x_{mrkIdx}^{t+\Delta t} &= x_{mrkIdx}^t + v_{xmrkIdx} \cdot \Delta t \\ z_{mrkIdz}^{t+\Delta t} &= z_{mrkIdz}^t + v_{zmrkIdz} \cdot \Delta t \end{aligned} \quad (B.24)$$

where x_{mrk}^t and z_{mrk}^t are the location of the markers in x and z direction at time t , and $x_{mrk}^{t+\Delta t}$ and $z_{mrk}^{t+\Delta t}$ are the location of the markers in x and z direction at time $t + \Delta t$. The Δt is the time step for MIC simulation. The v_{xmrk} and v_{zmrk} are the linear velocities of the markers. The equation (B.24) is used for advecting the markers only situated inside the domain.

Whereas the advected markers coming out of the domain are re-inserted at the top inlet nodes at every time step of simulation. The total number of markers escaping from all the outlet edges located in right, left, top and bottom are collected. These markers are recycled by distributing them randomly along the top edge and advected with the velocities at top edge (See equation (B.25)).

$$\begin{aligned} x_{(recyc \subset mrkIdx)}^{t+\Delta t} &= xIN_{rand} + v_{(xIN_{rand} \subset xmrkIdx)} \cdot \Delta t_{recyc} \\ z_{(recyc \subset mrkIdz)}^{t+\Delta t} &= zIN_{top} + v_{(zIN_{top} \subset zmrkIdz)} \cdot \Delta t_{recyc} \end{aligned} \quad (B.25)$$

In which the *recyc* is index for markers recycled. The *rand* is index for random inter-node in x direction (xIN). The *top* is index for top inter-node in z direction (zIN). The left hand side of equation (B.25) includes the recycled markers whose location is changed randomly in x direction at top inter-node in z direction. The right hand side of equation (B.25) shows the marker velocities in x and z direction with random and top indexes for

xIN and zIN respectively. The Δt_{recyc} is calculated as shown in equation (B.26).

$$\Delta t_{recyc} = \Delta t - \left(\frac{\Delta xl(Ixl)/v_{x_{mrk}(Ixl)} + \Delta xr(Ixr)/v_{x_{mrk}(Ixr)}}{+\Delta zd(Izd)/v_{z_{mrk}(Izd)} + \Delta zu(Izu)/v_{z_{mrk}(Izu)}} \right) \quad (B.26)$$

In equation (B.26) the Δt_{recyc} is the recycled time, Ixl index for markers crossing left inter-node, Ixr index for markers crossing right inter-node, Izu index for markers crossing upper inter-node, Izd index for markers crossing lower inter-node and Δxl , Δxr , Δzu , Δzd , are the left, right, upper and lower distances between markers and edge of nodes.

The solute flux required to calculate the solute mass balance is obtained using equation (B.27) which is interpolated to nodes using equation (B.15).

$$u_{z_{mrk}} = v_{x_{mrk}} \cdot \theta_{mrk} \cdot c_{mrk} \quad (B.27)$$

$$u_{z_{mrk}} = v_{z_{mrk}} \cdot \theta_{mrk} \cdot c_{mrk}$$

Appendix C

C.1 DREAM_{ZS} algorithm settings

The algorithmic parameters required for DREAM_{ZS} algorithm (Laloy and Vrugt 2012) used for Chapter 4 is summarized in Table C.1.

Table C.1: DREAM_{ZS} algorithmic parameters for optimizing of unsaturated soil parameters used in Chapter 4.

Parameter	Values	Description
d	Problem dependent	Dimension (number of parameters to estimate)
N	3	Number of Markov chains
K	15	Thinning parameter for appending proposals to the archive Z
M_0	5d	Initial size of archive Z
p_{SK}	0.1	Probability snooker update
p_{jrl}	0.9	Probability of selecting a jump rate of 1 (jump between two modes)
γ	0	Jump rate
d'	Integer between 1 and d	Number of dimensions that will updated jointly
δ	1	Number of chain pairs to generate candidate points
b	0.05	Perturbation of ergodicity
n_{CR}	3	Number of crossover values

Appendix D

D.1 Multi-Section Scatter Function Model

Multi section S_{11} (reflection) scatter function along with reflection coefficient between different sections k of the transmission line is given in equation (D.1) and equation (D.2) (Feng et al. 1999).

$$S_{11}^k = \frac{\rho_s^k(f) + S_{11}^{k-1}(f)\exp[-2\gamma_k(f)L_{i,k}]}{1 + \rho_s^k(f)S_{11}^{k-1}(f)\exp[-2\gamma_k(f)L_{i,k}]} \quad (\text{D.1})$$

with

$$\rho_s^k(f) = \frac{Z_{k-1}(f) - Z_k(f)}{Z_{k-1}(f) + Z_k(f)} \quad (\text{D.2})$$

where $Z_k(f)$ is the impedance and $y_k(f)$ is the propagation coefficient and $L_{1,k}$ the length of each section k as shown in Figure 5.2. Starting from section 1 equation (D.1) is iterated throughout all sections. An assumption regarding the final reflection (reflection at line section 0). For open ended transmission line $S_{11}^0 = 1$, for short ended transmission line, $S_{11}^0 = -1$ and for a matched transmission line $S_{11}^0 = 0$. The characteristic impedance for last section in the transmission line is assumed to be of 50Ω .

D.2 Characteristic Impedance

The parameters $Z_k(f)$ and $y_k(f)$ can be calculated from the models derived for the transmission-line theory. Models are available for non-ideal twin-head and coaxial transmission lines, in which we can account for distributed resistance R_s along the conductors,

the inductance L , the shunt conductance G , and the capacitance C per unit length of transmission line. In general a characteristic impedance of a transmission line is given as

$$Z = \sqrt{\frac{R_s + i2\pi fL}{G + i2\pi fC}} \quad (D.3)$$

$$\gamma = \sqrt{(R_s + i2\pi fL)(G + i1\pi fC)} \quad (D.4)$$

The characteristic impedance of a parallel transmission line depends on its diameter a of the wires and the distance separating them b . We have used coaxial cable, which is connected with the twin-wire probe and the cable tester on its either ends. Thus primary line constants for twin-head transmission line are listed in equation ((D.5)-(D.7)) and for the coaxial transmission are listed in equation ((D.8)-(D.10)). In these equations the subscripts tw denotes the twin head and co denotes coaxial.

$$L_{tw} = \frac{\mu_0\mu_r}{\pi} \cdot arccosh\left(\frac{b}{a}\right) \quad (D.5)$$

$$G_{tw} = \frac{\pi\sigma_{DCC}}{arccosh\left(\frac{b}{a}\right)} \quad (D.6)$$

$$C_{tw} = \frac{\pi\epsilon_0\epsilon_r(f)}{arccosh\left(\frac{b}{a}\right)} \quad (D.7)$$

$$L_{co} = \frac{\mu_0\mu_r}{2\pi} \cdot In\left(\frac{b}{a}\right) \quad (D.8)$$

$$G_{co} = \frac{2\pi\sigma_{DC}}{In\left(\frac{b}{a}\right)} \quad (D.9)$$

$$C_{co} = \frac{2\pi\epsilon_0\epsilon_r(f)}{In\left(\frac{b}{a}\right)} \quad (D.10)$$

Where μ_0 is the magnetic permeability of free space $1.2566 \times 10^{-6} \text{ H m}^{-1}$. μ_r is the relative magnetic permeability of the material between the conductors that we assume to be equal to 1 for all materials used in this study. ϵ_0 is the dielectric permeability of free space $8.8542 \times 10^{-12} \text{ F m}^{-1}$ and $\epsilon_r(f)$ is the complex relative dielectric permittivity of the material between the conductors which is a function of frequency. The permittivity of free space and the magnetic permeability are related to the speed of light, c , via $c = 1/\sqrt{\epsilon_0\mu_0} = 2.9979 \times 10^8 \text{ m s}^{-1}$.

The parameter $R_s \Omega \text{ m}^{-1}$ is the average resistivity per unit length of surface for unit width for both conductors caused by the skin effect. It consist of a DC resistance term R_{DC}

$$R_S(f)(\text{m}^{-1}) = R_{DC} + R_{AC}\sqrt{f} \quad (\text{D.11})$$

The inductance will change with frequency for similar reasons as the resistance and a result the term $R_s + i2\pi fL$ can be written as

$$R_S + i2\pi fL = (R_{DC} + R_{AC}\sqrt{f}) + i2\pi f \left(L + \frac{R_{AC}}{2\pi\sqrt{f}} \right) \quad (\text{D.12})$$

The electrical conductivity losses through the dielectric material between the conductors of the coaxial transmission line are described with $\sigma_{DC} \text{ S m}^{-1}$.

For ideal coaxial transmission line ($R_s = 0$ and $\sigma_{DC} = 0$) in which air forms dielectric ($\epsilon_r = 1$) for equation (D.9).

$$Z_0 = 60 \ln \left(\frac{b}{a} \right) \quad (\text{D.13})$$

Once the optimal value for characteristic impedance Z_0 is known we can calculate the frequency dependent impedance of transmission line section, $Z(f)$.

$$Z(f)(\Omega) = \frac{Z_0}{[\epsilon_r^*(f)]^{1/2}} \quad (\text{D.14})$$

Dielectric permittivity including the DC resistance term, for two wire probe σ_{DC} would be replace by σ_{DCC} .

$$\epsilon_r^*(f) = \epsilon_r(f) - \frac{i\sigma_{DC}}{2\pi f\epsilon_0} \quad (\text{D.15})$$

The propagation coefficient is given by

$$\gamma = \frac{i2\pi f[\epsilon_r^*(f)]^{1/2}}{c} \quad (\text{D.16})$$

D.3 DREAM_{ZS} algorithm settings

The parameters required for DREAM_{ZS} algorithm (Laloy and Vrugt 2012) for Chapter 5 is summarized in Table D.1.

Table D.1: DREAM_{ZS} algorithmic parameters for optimization of TDR parameters and unsaturated parameters used in Chapter 5.

Parameter	Values	Description
d	Problem dependent	Dimension (number of parameters to estimate)
N	3	Number of Markov chains
K	10	Thining parameter for appending proposals to the archive Z
M_0	10d	Initial size of archive Z
p_{SK}	0.1	Probability snooker update
p_{jr}	0.9	Probability of selecting a jump rate of 1 (jump between two modes)
γ	0	Jump rate
d'	Integer between 1 and d	Number of dimensions that will updated jointly
δ	1	Number of chain pairs to generate candidate points
b	0.05	Perturbation of ergocity
n_{CR}	3	Number of crossover values

Bibliography

- Agdag, O.N., Sponza, D.T., 2004. Effect of aeration on the performance of a simulated landfilling reactor stabilizing municipal solid wastes. *Journal of Environmental Science and Health* 39, 11–12.
- Ahmed, S., Khanbilvardi, R.M., Fillos, J., Gleason, P.J., 1992. Two dimensional leachate estimation through landfills. *Journal of Hydraulic Engineering* 118, 306–322.
- Al-Ghazawi, Z.D., Abdulla, F., 2008. Mitigation of methane emissions from sanitary landfills and sewage treatment plants in Jordan. *Clean Technologies and Environmental Policy* 10, 341–350. doi:10.1007/s10098-008-0145-8.
- Al-Lawatia, M., 2012. An Eulerian-Lagrangian control volume scheme for two dimensional-unsteady advection-diffusion problems. *Numerical methods for partial differential equations* 28, 1481–1496.
- Ali, M., Cotton, A., Westlake, K., 2005. Waste disposal in developing countries. URL: <http://www.lboro.ac.uk/orgs/well/resources/fact-sheets/fact-sheets-htm/waste.htm>.
- Aravena, J.E., Dussaillant, A., 2009. Storm - Water Infiltration and Focused Recharge Modeling with Finite Volume Two-Dimensional Richards Equation: Application to an Experimental Rain Garden. *Journal of Hydraulic Engineering* 135, 1073–1080.
- Aref, H., 1983. Integrable, chaotic, and turbulent vortex motion in two-dimensional flows. *Annual Review of Fluid Mechanics* 15, 345–389.
- Arnold, D.N., 2015. Stability, consistency, and convergence of numerical discretizations. *Encyclopedia of Applied and Computational Mathematics* Springer-Verlag , 1–9.
- Augenstein, D., Morck, R., Pacey, J., Reinhart, D., Yazdani, R., 1998. White paper: The bioreactor landfill an innovation in solid waste management, in: *Proceedings from Swana's 3rd Annual Landfill Symposium*, pp. 173–180.
- Ayub, S., Khan, A.F., 2011. Landfill practice in india: A review. *Journal of Chemical and Pharmaceutical Research* 3, 270–279.

- Baba, A., Kavdir, Y., Deniz, O., 2004. The impact of an open waste disposal site on soil and groundwater pollution. *International Journal of Environment and Pollution* 22, 676–687.
- Bakis, R., Tuncan, A., 2010. An investigation of heavy metal and migration through groundwater from the landfill area of Eskisehir in Turkey. *Environmental Monitoring and Assessment* doi:<http://dx.doi.org/10.1007/s10661-010-1568-3>.
- Bandara, N.J.G.J., Hettiaratchi, J.P.A., Wirasinghe, S.C., Pilapiiya, S., 2007. Relation of waste generation and composition to socio-economic factors: a case study. *Environmental Monitoring and Assessment* 135, 31–39.
- Bareither, C.A., Benson, C.H., Barlaz, M.A., Edil, T.B., Tolaymat, T.M., 2010. Performance of North American Bioreactor Landfills. I: Leachate Hydrology and Waste Settlement. *Journal of Environmental Engineering-Asce* 136, 824–838.
- Barlaz, M.A., Bareither, C.A., Hossain, A., Saquing, J., Mezzari, I., Benson, C.H., Tolaymat, T.M., Yazdani, R., 2010. Performance of North American Bioreactor Landfills. II: Chemical and Biological Characteristics. *Journal of Environmental Engineering-Asce* 136, 839–853. doi:10.1061/(asce)ee.1943-7870.0000220.
- Barlaz, M.A., Rooker, A.P., Kjeldsen, P., Gabr, M.A., Borden, R.C., 2002. Critical evaluation of factors required to terminate the postclosure monitoring period at solid waste landfills. *Environmental Science and Technology* 36, 3457–3464.
- Baviskar, S.M., Heimovaara, T.J., 2011. Suitability of different conceptual models for assessing the hydrology of full scale pilot landfill, in: *Hydro-Physico-Mechanics of Landfills 4*, Santander, Spain, 27-28 April.
- Baviskar, S.M., Heimovaara, T.J., 2014. Addressing preferential flow in landfills by finite difference method and marker-in-cell method., in: *Heat Transfer and Fluid Flow. Proceedings published ISBN 978-1-927877-09-8*.
- Bear, J., 1988. *Dynamics of Fluids in Porous Media*. Dover.
- Bendz, D., Singh, V.P., Rosqvist, H., Bengtsson, L., 1998. Kinematic wave model for water movement in municipal solid waste. *Water resources research* 34, 2963–2970.
- Benson, C.H., Barlaz, M.A., Lane, D.T., Rawe, J.M., 2007. Practice review of five bioreactor/recirculation landfills. *Waste Management* 27, 13–29. doi:10.1016/j.wasman.2006.04.005.
- Berinnger, H., Kornhuber, R., Sanders, O., 2011. Fast and robust numerical solution of the richards equation in homogeneous soil. *SIAM J. Society for Industrial and Applied Mathematics* 49, 2576–2597.
- Betteli, M., Flury, M., 2009. Errors in water retention curves determined with pressure plates. *Soil Society of American Journal* 73, 1453–1460.

- Blight, G.E., Ball, J.M., Blight, J.J., 1992. Moisture and suction in sanitary landfills in semiarid areas. *Journal of Environmental Engineering* 118, 865–877.
- Borglin, S.E., Hazen, T.C., Oldenburg, C.M., Zawislanski, P.T., 2004. Comparison of aerobic and anaerobic treatment of municipal solid waste. *Journal of the Air and Waste Management Association* 54, 815–822.
- Brusseau, M.L., Rao, P.S.C., 1990. Modelling solute transport in structured soils: A review. *Geoderma* 46, 169–192.
- Buckingham, E., 1907. Water retention in soil. volume 38. *Soil Bulletin*, U.S. Department of Agriculture.
- Bun, A., Heimovaara, T., Baviskar, S., 2013. Inverse modelling of landfill processes: estimating emission potential. *Proceedings Sardinia 2013, Fourth International Waste management and Landfill Symposiu.*, S. Margherita di Pula, Cagliari, Italy. .
- Butcher, J.C., 2003. *Numerical Methods for Ordinary Differential Equations*. New York: John Wiley & Sons, ISBN 978-0-471-96758-3.
- Butt, T.E., Lockley, E., Oduyemi, K.O.K., 2008. Risk assessment of landfill disposal sites - State of the art. *Waste Management* 28, 954–964. doi:10.1016/j.wasman.2007.05.012.
- Calabro, P.S., Sbaffoni, S., Orsi, S., Gentili, E., Meoni, C., 2010. The landfill reinjection of concentrated leachate: Findings from a monitoring study at an Italian site. *Journal of Hazardous Materials* 181, 962–968. doi:10.1016/j.jhazmat.2010.05.107.
- Celia, M., Bouloutas, E.T., Zarba, R.L., 1990a. A general mass-conservative numerical solution for the unsaturated flow equation. *Water Resources Research* 26, 1483–1496.
- Celia, M.A., Russell, T.F., Herrera, I., Ewing, R.E., 1990b. An eulerian-lagrangian localized adjoint method for advection-diffusion equation. *Advance Water Resources* 13, 187–206.
- Charles, W., Walker, L., Cord-Ruwisch, R., 2009. Effect of pre-aeration and inoculum on the start-up of batch thermophilic anaerobic digestion of municipal solid waste. *Bioresour. Technol.* 100, 2329–2335. doi:10.1016/j.biortech.2008.11.051.
- Chesworth, W., 2007. *Encyclopedia of Soil Science*. Springer Science & Business Media.
- Cho E., Kazuo T., Masataka, H., Tatsuyoshi. Y., Sotaro H., 2009. Toxicological evaluation of the chemical oxidation methods for landfill stabilization. *Waste Manag* 29, 1006–1011. doi:10.1016/j.wasman.2008.08.003.
- COMSOL, 4.3b. <http://www.comsol.nl/>.
- Cossu, R., 2005. The sustainable landfilling concept, CISA, Environmental Sanitary Engineering Centre, Italy, S. Margherita di Pula, Cagliari, Italy; 3 - 7 October 2005.

- Cossu, R., 2007. The Mass Balance: a key issue for landfill sustainability, in: Cossu, R., van der Sloot, H.A. (Eds.), *Sustainable Land Filling*.
- Cossu, R., Raga, R., Rossetti, D., 2003. The PAF model: an integrated approach for landfill sustainability. *Waste Management* 23, 37–44.
- Cvetkovic, V., Dagan, G., 1994. Transport of kinetically sorbing solute by steady random velocity in heterogeneous porous formations. *Journal of Fluid Mechanics* 265, 189–215.
- Cvetkovic, V., Dagan, G., Cheng, H., 1998. Contaminant transport in aquifers with spatially variable hydraulic and sorption properties. *Proceedings of the Royal Society of London Series a-Mathematical Physical and Engineering Sciences* 454, 2173–2207.
- Cvetkovic, V., Shapiro, A.M., Dagan, G., 1992. A solute flux approach to transport in heterogeneous formations .2. Uncertainty analysis. *Water Resources Research* 28, 1377–1388.
- Das, D.B., Hassanizadeh, S.M., Rotter, B.E., Ataie-Ashtiani, B., 2004. A numerical study of micro-heterogeneity effects on upscaled properties of two phase flow in porous media. *Transport in Porous Media* 56, 329–350.
- Davis-Hoover, W.J., Carson, D.A., Slomczynski, D.J., Feldhake, D., Holder, E., Hater, G.R., Green, R.B., Martin, J.F., Kavanaugh, R.G., 2001. Microbial populations and moisture content in a conventionally operated municipal solid waste landfill, in: *Natural attenuation of environmental contaminants*, Battelle Press. pp. 247–252.
- Demetracopoulus, A.C., Sehayek, L., Erdogan, H., 1986. Modeling leachate production from municipal landfills. *Journal Environmental Engg* 112, 849–886.
- Demir, A., Ozkaya, B., Bilgili, M.S., 2004. The effects on waste stabilization of leachate recirculation in landfills. *Fresenius Environmental Bulletin* 13, 918–922.
- Desai, C., . *Elementary finite element method*. Prentice - Hall, Inc., Englewood Cliffs, New Jersey 07632.
- Dussaillant, A.R., Wu, C.H., Potter, K., 2004. Richards equation model of a rain garden. *Journal of Hydrologic Engineering* 9-3, 219–225.
- EC, 1999. The Council Directive 1999/31/EC of 26 April 1999 on the landfill of waste. *Official Journal of the European Communities L* 182, 1–19.
- EC, 2010. Being wise with waste: the eu’s approach to waste management. URL: <http://ec.europa.eu/environment/waste/pdf/WASTE%20BROCHURE.pdf>.
- EEA, 2009. Diverting waste from landfill: Effectiveness of waste-management policies in the european union. URL: <http://www.eea.europa.eu/publications>.
- El-Amrani, M., Seaid, M., 2012. A finite element semi-lagrangian method with L2 interpolation. *International Journal for numerical methods in engineering* 90, 1485–1507.

- El-Fadel, M., 1999. Leachate recirculation effects on settlement and biodegradation rates in MSW landfills. *Environmental Technology* 20, 121–133.
- El-Fadel, M., Findikakis, A.N., Leckie, J.O., 1997a. Modelling leachate generation and transport in solid waste landfills. *Environmental Technology* 18, 669–686.
- El-Fadel, M., Findikakis, A.N., O, L.J., 1997b. Modeling leachate generation and transport in solids waste landfills. *Environmental Technology* 18, 669–686. doi:10.1080/09593331808616586.
- Erses, A.S., Onay, T.T., 2003. In situ heavy metal attenuation in landfills under methanogenic conditions. *Journal of Hazardous Materials* 99, 159–175. doi:10.1016/s0304-3894(02)00354-0.
- EUTECH, EC91346S. <http://www.eutechinst.com/>.
- Ewing, R.E., Wang, H., 2001. A summary of numerical methods for time-dependent advection-dominated partial differential equations. *Journal of Computational and Applied Mathematics* 128, 423–445.
- Fellner, J., Brunner, P.H., 2010. Modeling of leachate generation from MSW landfills by a 2-dimensional 2-domain approach. *Waste management (New York, N.Y.)* 30, 2084–95. doi:10.1016/j.wasman.2010.03.020.
- Fellner, J., Döberl, G., Allgaier, G., Brunner, P.H., 2009. Comparing field investigations with laboratory models to predict landfill leachate emissions. *Waste management (New York, N.Y.)* 29, 1844–51. doi:10.1016/j.wasman.2008.12.022.
- Feng, W., Lin, C.P., Deschamps, R.J., Drenvich, V.P., 1999. Theoretical model of a multisection time domain reflectometry measurement system. *Water Resource Research* 35, 2321–2331.
- Fetter, C.W., 1993. *Contaminant Hydrogeology*. Prentice Hall, upper Saddle River, NJ 07458.
- Feyen, J., Jacques, D., Timmerman, A., Vanderborght, J., 1998. Modelling water flow and solute transport in heterogeneous soils: A review of recent approaches. *Journal of Agricultural Engineering Research* 70, 231–256.
- Frehner, M., Schmalholz, S.M., Steeb, H., 2008. Comparison of finite difference and finite element methods for simulating two-dimensional scattering of elastic waves. *Physics of the Earth and Planetary Interiors* 171.
- Freyberg, D.L., Reeder, J.W., Franzini, J.B., Remson, I., 1980. Application of the Green-Ampt model to infiltration under time-dependent surface water depths. *Water Resources Research* 16, 517–528.
- van Genuchten, M., 1980. A closed-form Equation for predicting the hydraulic conductivity of unsaturated soils. *Soil Science Society of America Journal* 44(5), 892–898.
- Gerya, T., Yuen, D., 2003. Characteristic-based marker-in-cell method with conservative finite differences schemes for modeling geological flows with strongly variable transport properties. *Physics of the Earth and Planetary Interiors* 140, 293–318.

- Gerya, T.V., 2010. Numerical geodynamic modelling. Cambridge University Press.
- Gholamifard, S., Eymard, R., Duquennoi, C., 2008. Modeling anaerobic bioreactor landfills in methanogenic phase: long term and short term behaviors. *Water Research* 42, 5061–5071. doi:10.1016/j.watres.2008.09.040.
- Green, W.H., Ampt, G.A., 1911. Studies on soil physics,1: The flow of air and water through soils. *J. Agr.Sci* 4, 1–24.
- Gribb, M.M., 1996. Parameter estimation for determining hydraulic properties of a fine sand from transient flow measurements. *Water Resources Research* 32, 1965–1974.
- Guo, H., 2011. A simple algorithm for fitting a gaussian function [dsp tips and tricks]. *Signal Processing Magazine, IEEE* 28, 134–137.
- Guyonnet, D., Didier-Guelorget, B., Provost, G., Feuillet, C., 1998. Accounting for water storage effects in landfill leachate modelling. *Waste Management and Research* 16, 285–295.
- Hamil, L., Bel, F.G., 1986. Groundwater resource department. Butterworths.
- Han, J.S., Kim, C.G., 2010. Characterization of molecular biological indicators to define stabilization of landfills. *Korean Journal of Chemical Engineering* 27, 868–873. doi:10.1007/s11814-010-0124-8.
- Haydar, M.M., Khire, M.V., 2005. Leachate recirculation using horizontal trenches in bioreactor landfills. *Journal of Geotechnical and Geoenvironmental Engineering* 131, 837–847.
- Haydar, M.M., Khire, M.V., 2007. Leachate recirculation using permeable blankets in engineered landfills. *Journal of Geotechnical and Geoenvironmental Engineering* 133, 360–371. doi:10.1061/(asce)1090-0241(2007)133:4(360).
- Haydar, M.M., Khire, M.V., Mb, 2006. Geotechnical sensor system to monitor injected liquids in landfills. *Geotechnical Testing Journal* 29, 37–44. URL: <http://www.astm.org>.
- Hayhoe, H.N., 1978. Study of the relative efficiency of finite difference and galerkin techniques for modeling soil-water transfer. *Water Resources Research* 14, 97–102.
- Heimovaara, T., Oonk, H., van der Sloot, H.A., van Zomeren, A., 2010. Reduction of the long term emission potential of existing landfills, FINAL REPORT PHASE 2. Technical Report. Stichting Duurzaam Storten.
- Heimovaara, T.J., 1992. Time domain reflectometry measurements of water-content and electrical-conductivity of layered soil columns - comment. *Soil Science Society of America Journal* 56, 1657–1658.
- Heimovaara, T.J., 2011. Quantification of long term emission potential from landfills, in: *Hydro-Physico-Mechanics of Landfills*, Santander, Spain, 27-28 April 2011.

- Heimovaara, T.J., Cossu, R., van der Sloot, H.A., 2007. State of the art and perspectives for sustainable landfilling, in: *Proceedings Sardinia 2007, Eleventh International Waste Management and Landfill Symposium S. Margherita di Pula, Cagliari, Italy*; 1 - 5 October 2007, CISA, Environmental Sanitary Engineering Centre, Italy.
- Heimovaara, T.J., Huisman, J.A., Vrugt, J.A., Bouten, W., 2004. Obtaining the spatial distribution of water content along a TDR probe using the SCEM-UA Bayesian inverse modeling scheme. *Vadose Zone Journal* 3, 1128–1145.
- Hendrickx, J.M.H., Flury, M., 2001. Uniform and preferential flow, mechanisms in the vadose zone, *Conceptual Models of Flow and Transport in the Fractured Vadose Zone*. National Research Council, National Academy Press, Washington, DC, pp. 149-187.
- Heyer, K.U., Hupe, K., Ritzkowski, M., Stegmann, R., 2005. Pollutant release and pollutant reduction - Impact of the of landfills. *Waste Management* 25, 353–359. doi:10.1016/j.wasman.2005.02.007.
- Homma, Y., Ishida, T., Shimotashiro, T., 2004. A Cone Permeameter for determining hydraulic conductivity in unsaturated soils. Toyo University, Saitama, Japan .
- Hoornweg, D., Bhada-Tata, P., 2012. What a Waste: A Global Review of Solid Waste Management. Technical Report. The World Bank. URL: <http://go.worldbank.org/BCQEPOTM00>.
- Hsu, S.M., C, N., Hung, P., 2002. Assessment of three infiltration formulas based on model fitting on richards equation. *Journal of Hydrologic Engineering* 7, 373–379.
- Hudgins, M.P., Bessette, B.J., March, J.C., McComb, S.T., 2000. Aerobic landfill bioreactor. American Technologies, Inc., U.S. Patent 6,024,513.
- HYPROP-S, UMS. <http://www.ums-muc.de/>.
- IGEL, 2014. Zero waste: "nil to landfill" is now a practical goal. URL: <http://knowledge.wharton.upenn.edu/article/zero-waste-nil-landfill-now-practical-goal/>.
- Inoue, Y., Asakura, H., Inanc, B., Endo, K., Ishigaki, T., Yamada, M., Ono, Y., 2005. A new approach for a sustainable landfill in japan, *CISA, Environmental Sanitary Engineering Centre, Italy, S. Margherita di Pula, Cagliari, Italy*; 3 - 7 October 2005.
- Jarvis, N.J., 1998. Modelling the impact of preferntial flow on nonpoint source pollution, In *Physical Non equilibrium in soils: Modeling and Apllication*. Ann, Arbor Press, Chelsea, MI.
- Jiang, J., Huang, Y., Zhang, Y., 2008. Technology method for accelerating landfill stabilization by leachate recirculation.
- Jury, W.A., 1982. Simulation of solute transport using a transfer function model. *Water resources research* 18, 363–368.

- Jury, W.A., Roth, K., 1990. Transfer Functions and Solute Movement through Soil. Theory and Applications. Birkhauser.
- Jury, W.A., Stolzy, L.H., 1982. A field test of the transfer function model for predicting solute transport. *Water Resources Research* 18, 369–375.
- Kattenberg, W., Heimovaara, T., 2011. Policy process of allowing research pilots for sustainable emission reduction at landfills in the netherlands, in: *Proc. Thirteenth International Waste Management and Landfill Symposium*,.
- Kaushal, N., 2012. Growth vs garbage: Can we have efficient disposal mechanism? URL: http://articles.economictimes.indiatimes.com/2012-04-26/news/31410327_1_recyclable-waste-garbage-waste-.
- Kazimoglu, Y.K., McDougall, J.R., Pyrah, I.C., 2006. Unsaturated hydraulic conductivity of landfill waste, in: *Proceeding. 4th Intl.Conference on Unsaturated Soils, Carefree, Arizona:1525-1534*.
- Kindlein, J., Dinkler, D., Ahrens, H., 2006. Numerical modelling of multiphase flow and transport processes in landfills. *Waste management and research* 24, 376–387.
- Kjeldsen, P., Barlaz, M.A., Rooker, A.P., Baun, A., Ledin, A., Christensen, T., 2002. Present and long-term composition of MSW landfill leachate: a review. *Crit. Rev. Environ. Sci.Technol.* 32, 297–336.
- Koerner, R.M., Soong, T.Y., 2000. Leachate in landfills: the stability issues. *Geotextiles and Geomembranes* 18, 293–309.
- Kohler, A., Abbaspour, K.C., Fritsch, M., van Genuchten, M.T., Schulin, R., 2001. Simulating unsaturated flow and transport in macroporous soil to tile drains subject to an entrance head: model development and preliminary evaluation. *Journal of Hydrology* 254, 67–81.
- Krysl, P., 2010. Thermal and Stress analysis with Finite Element Method, Accompanied by the MATLAB toolbox FAESOR. Pressure Cooker Press.
- KSAT, UMS. <http://www.ums-muc.de/>.
- Kumar, C.P., 2015. Modelling of groundwater flow and data requirements. *International Journal of Modern Sciences and Engineering Technology.* 2, 18–27.
- LaBolle, E.M., Zhang, Y., 2006. Reply to comment by d.h. lim on 'diffusion processes in composite porous media and their numerical integration by random walks: Generalized stochastic differential equations with discontinuous coefficients'. *Water Resource Research* 42, W02602.
- Laloy, E., Huisman, J.A., Jacques, D., 2014. High resolution moisture profiles from full-waveform probabilistic inversion of TDR signals. *Journal of Hydrology* 519, 2121–2135.
- Laloy, E., Vrugt, J.A., 2012. High dimensional posterior exploration of hydrologic models using multiple-try DREAMzs and high-performance computing. *Water resources research* 48, W01526.

- Ledieu, J., De Ridder, P., De Clerck, P., Dautrebande, S., 1986. A method of measuring soil moisture by time-domain reflectometry. *J. Hydrol* 88, 319–328.
- Lincoln, J., 2011. Swiss business hub south africa.
- Lourenco, S., Gallipoli, D., Toll, D., Evans, F Medero, G., 2007. Experimental unsaturated soil mechanics, in: *Springer Proceedings in Physics*, pp. 95–102.
- Lu, H.J., Luan, M.T., 2009. Numerical Modeling of Moisture Transport Through Evapotranspirative Landfill Cover System. 2009 International Conference on Modeling, Simulation and Optimization, Proceedings , 143–146.
- Lunati, I., Kinzelbach, W., Sorensen, I., 2003. Effects of pore volumn-transmissivity correlation on transport phenomena. *Journal of Contaminant Hydrology* 67.
- Ma, Y., Feng, S., Su, D., Gao, G., Huo, Z., 2010. Modeling water infiltration in a large layered soil column with a modified Green-Ampt model and HYDRUS- 1D. *Computers and Electronics in Agriculture* 71S, S40–S47.
- Malcolm, E., 1999. *Handbook of soil science*. Millers Publications.
- Matanga, G.B., 1996. Stream and pseudopotential functions in visualizing groundwater flow and transport processes. *Water Resources Research* 32, 953–957.
- MATLAB, 2014b. <http://www.mathworks.nl/>.
- McCreanor, P.T., Reinhart, D.R., 1999. Hydrodynamic modeling of leachete recirculating landfills. *Waste Management Research* 17, 465–469.
- McDougall, J., 2007. A hydro-bio-mechanical model for settlement and other behaviour in land-filled waste. *Computers and Geotechnics* 34, 229–246. doi:10.1016/j.compgeo.2007.02.004.
- McKay, M.D., Beckman, R.J., Conover, W.J., 1978. A comparsion of three methods for selecting values of input variables in the analysis of the output from a computer code. *Technometrics* 21(2), 239–245.
- Mesu, E., 1982. Einflussfaktoren auf den Wasserhaushalt von Hausmülldeponien (in German: Factors determining the water balance of MSW landfills), *Gas und Wasserhaushalt von Mülldeponien. Internationale Fachtagung. Institut für Stadtbauwesen, Braunschweig.* , 271–288.
- METTLER, PM 16. <http://nl.mt.com/>.
- METTLER, PM 30-K. <http://nl.mt.com/>.
- Mikac, N., Cosovic, B., Ahel, M., Andreis, S., Tonic, Z., 1998. Assessment of groundwater contamination in the vicinity of a municipal solid waste landfill (Zagreb, Croatia). *Water Science and Technology* 37, 37–44.

MOHR, CT Viewer. www.mohr-engineering.com.

Mualem, Y., 1976. A new model for predicting the hydraulic conductivity of unsaturated soil. *Water Resource Research* 12.

Netherlands, T., 2016. Stortbesluit bodembescherming URL: <http://wetten.overheid.nl/BWBR0005858/2016-07-01#SlotformulierEnOndertekening>.

Neto, R.O., Petter, C.O., Cortina, J.L., 2011. The current situation of sanitary landfills in brazil and the application of economic models. Mining technology course, Federal University of Pampa - UNIPAMPA .

Neuman, S., 1984. Adaptive Eulerian-Lagrangian finite element method for advection-dispersion. *International Journal for Numerical Methods in Engineering* 20, 321–337.

Nimmo, J.R., 2005. 150:Unsaturated flow zone processes;Encyclopedia of hydrological sciences:Part 13. Wiley.

OECD, UTC(GMT). Landfilled msw data. URL: www.oecd.stat.

Oman, C., Rosqvist, H., 1999. Transport fate of organic compounds with water through landfills. *Water Research* 33, 2247–2254.

Peiro, J., Sherwin, S., 2005. Handbook of Materials Modeling. Volume I: Methods and Models,1-32. Springer.

Peters, A., Durner, W., 2006. Improved estimation of soil water retention charactersites from hydrostatic column experiments. *Water Resources Research* 42.

Pinder, G.F., Celia, M.A., 2006. Subsurface Hydrology. Wiley.

Pohland, F.G., Alyousfi, B., 1994. Design and operation of landfills for optimum stabilization and biogas production. *Water Science and Technology* 30, 117–124.

Powrie, W., Beaven, R.P., 1999. Hydraulic properties of household waste and implications for landfills. *Proceedings of the Institution of Civil Engineers-Geotechnical Engineering* 137, 235–247.

Prantl, R., Tesar, M., Huber-Humer, M., 2005. Changes in organic matter during in-situ of old landfills, CISA, Environmental Sanitary Engineering Center, Italy, S. Margherita di Pula, Cagliari, Italy, 3-7 October 2005.

Radu, F.A., Suci, N., Hoffmann, J., Vogel, A., Kolditz, O., Park, C.H., Attinger, S., 2011. Accuracy of numerical simulations of contaminant transport in heterogeneous aquifers: A comparative Study. *Advances in Water Resources* 34, 47–61.

Read, A.D., Hudgins, M., Phillips, P., 2001. Perpetual landfilling through aeration of the waste mass; lessons from test cells in Georgia (USA). *Waste Management* 21, 617–629.

- Reinhart, D.R., 1996. Full-scale experiences with leachate recirculating landfills: Case studies. *Waste Management & Research* 14, 347–365.
- Reinhart, D.R., AlYousfi, A.B., 1996. The impact of leachate recirculation on municipal solid waste landfill operating characteristics. *Waste Management & Research* 14, 337–346.
- Rich, C., Gronow, J., Voulvoulis, N., 2008. The potential for aeration of MSW landfills to accelerate completion. *Waste Management* 28, 1039–1048.
- Richards, L.A., 1931. Capillary conduction of liquids through porous medium. *Physics* 1:318.
- Ritzkowski, M., Stegmann, R., Heyer, K.U., 2007. Parameters for the Assessment of Landfill Sustainability Based on the Results of Landfill Aeration, in: Cossu, R., van der Sloot, H. (Eds.), *Sustainable Land Filling*.
- Robinson, A., Sewell, G.C., Wu, S., Damodaran, N., Kalas-Adams, N., 2011. Landfill data from china: Addressing information needs for methane recovery .
- Rosqvist, H., Destouni, G., 2000. Solute transport through preferential pathways in municipal solid waste. *Journal of Contaminant Hydrology* 46, 39–60.
- Rosqvist, H., Dollar, L.H., Fourie, A.B., 2005a. Preferential flow in municipal solid waste and implications for long term leachate quality : bvaluation of laboratory-scale experiments. *Waste Management Research* 23, 367–380.
- Rosqvist, N.H., Dollar, L.H., Fourie, A.B., Rosqvist, H., 2005b. Preferential flow in municipal solid waste and implications for long-term leachate quality: valuation of laboratory-scale experiments. *Waste Management and Research* 23, 367–380.
- Rowe, R.K., Badv, K., 1996. Advective-diffusive contaminant migration in unsaturated sand and gravel. *Journal of Geotechnical Engineering-ASCE* 122, 965–975.
- Sanphoti, N., Towprayoon, S., Chaiprasert, P., Nopharatana, A., 2006. The effects of leachate recirculation with supplemental water addition on methane production and waste decomposition in a simulated tropical landfill. *Journal of Environmental Management* 81, 27–35. doi:10.1016/j.jenvman.2005.10.015.
- Schafer, W., 2001. Predicting natural attenuation of xylene in groundwater using a numerical model. *Journal of Contaminant Hydrology* 52, 57–83.
- Scharff, H., 2007. Sustainable Landfilling, in: Cossu, R., van der Sloot, H. (Eds.), *Sustainable Landfill*. CISA, Environmental Sanitary Engineering Centre, Italy.
- Scharff, H., 2014. Landfill reduction experience in The Netherlands. *Waste Management* 34, 2218–2224. doi:10.1016/j.wasman.2014.05.019.
- Schelle, H., Heise, L., Jänicke, K., Durner, W., 2013. Water retention characteristics of soils over the whole moisture range: a comparison of laboratory methods. *European Journal of Soil Science* 64, 814–821.

- Schiappacasse, M.C., Palma, J., Poirrier, P., Ruiz-Filippi, G., Chamy, R., 2010. Improved sanitary landfill design using recirculation of anaerobically treated leachates: generation of advanced design criteria. *Electronic Journal of Biotechnology* 13. doi:10.2225/vol13-issue3-fulltext-1.
- Schöberl, J., 2003. NETGEN-4.3.
- Shahraiyini, H.T., Ashtiani, B.A., 2012. Mathematical forms and numerical schemes for the solution of unsaturated flow equations. *Journal of irrigation and drainage engineering* 138(1), 63–72.
- Simpson, M.J., Clement, T.P., 2003. Comparison of finite difference and finite element solutions to the variably saturated flow equation. *Journal of Hydrology* 270, 49–64.
- Šimunek, J., 1999. Estimating unsaturated soil hydraulic properties from laboratory tension disc infiltrometer experiments. *Water Resource Research* 30, 2965–2979.
- Šimunek, J., Jarvis, N.J., van Genuchten, M.T., Gärdenäs, A., 2003. Review and Comparison of models for describing non-equilibrium and preferential flow and transport in the vadose zone. *Journal of hydrology* 272, 14–31.
- Skopp, J., 1981. Comment on 'Micro-meso and macroporosity of soil'. *Soil Science Society of America Journal* 45, 1246.
- Smith, I.M., Griffiths, D.V., 2004. Programming the finite element method. Wiley, Fourth Edition.
- Solone, R., Bittelli, M., Tomei, F., Morari, F., 2012. Errors in water retention curves determined with pressure plates: effects on the soil water balance. *Journal of Hydrology* 470-471, 65–74.
- Sormunen, K., Ettala, M., Rintala, J., 2008a. Detailed internal characterisation of two Finnish landfills by waste sampling. *Waste Management* 28, 151–163. doi:10.1016/j.wasman.2007.01.003.
- Sormunen, K., Ettala, M., Rintala, J., 2008b. Internal leachate quality in a municipal solid waste landfill: Vertical, horizontal and temporal variation and impacts of leachate recirculation. *Journal of Hazardous Materials* 160, 601–607. doi:10.1016/j.jhazmat.2008.03.081.
- Shrivastava, R., Yeh, T.C.J., 1991. Analytical solutions for one-dimensional transient infiltration toward the water table in homogeneous and layered soils. *Water Resources Research* 27(5), 753–762.
- Stromberg, J., 2013. Trashing the earth: We'll soon make 11 million tones of solid waste a day. *The Washington Post*. URL: Smithsonia.com.
- Sun, N., 1999. A finite cell method for simulating the mass transport process in porous media. *Water Resources Research* 35(12), 3649–3662.
- Tachobanoglous, G., Kreith, F., 2002. Handbook of solid waste management. McGraw-Hill Handbooks.

- Thiemann, M., Trosset, M., Gupta, H., Sorooshian, S., 2001. Bayesian recursive parameter estimation for hydrologic models. *Water Resource Research* 37, 2521–2535.
- Thoma, M.J., Barrash, W., Cardiff, M., Bradford, J., Mead, J., 2013. Estimating unsaturated hydraulic functions for coarse sediment from field-scale infiltration experiment. *Vadose Zone Journal* 13, 1–17.
- Transmitter, DO 9786T-RI. <http://www.deltaohmeurope.com/>.
- TRILTECHNIEK, TT-100. <http://www.stilettotriltechniek.nl>.
- Ugoccioni, M., Zeiss, C., 1997. Comparison of two approaches to modelling moisture movement through municipal solid waste. *J. Environ. Syst.* 25, 41–63.
- Ugoccioni, M., Zeiss, C., 1997. Improvement of leachate prediction through municipal solid waste layers. *Journal of the American Water Resources Association* 33, 1265–1278.
- Vehlow, J., Bergfeldt, B., Visser, R., Wilen, C., 2007. European Union waste management strategy and the importance of biogenic waste. *Journal of Material Cycles and Waste Management* 9, 130–139. doi:10.1007/s10163-007-0178-9.
- VERDERFLEX, R2550120 AU RS1. <http://www.verderflex.com/>.
- Vincent, F., Beaudoin, G., Colin, F., 1991. Waste behaviour modelling: a numerical model to describe the flow, transport and biodegradation processes. *Proceeding Sardinia 91, Third International Landfill Symposium*, 847–855.
- van Vossen, W.J., Heyer, K.U., 2009a. Feasibility study pilot project sustainable emission reduction at the existing landfills Kragge and Wieringermeer in the Netherlands. Preliminary design and cost-estimate of the technical measures infiltration and to enhance stabilization at the landfill. Technical Report. Royal Haskoning.
- van Vossen, W.J., Heyer, K.U., 2009b. Feasibility study sustainable emission reduction at the existing landfills Kragge and Wieringermeer in the Netherlands. Specific report: Current status of landfill Wieringermeer. Technical Report. Royal Haskoning.
- Vrugt, J.A., 2016. Markov chain monte carlo simulation using the dream software package: Theory, concepts and matlab implementation. *Environmental Modelling & Software* 75, 273–316.
- Vrugt, J.A., Stauffer, P.H., Wohling, T., Robinson, B.A., Vesselinov, V.V., 2008. Inverse modeling of subsurface flow and transport properties: A review with new developments. *Vadose Zone Journal* 7, 843–864.
- Šimunek, J., van Genuchten, M.T., 2008. Modeling nonequilibrium flow and transport processes using Hydrus. *Vadose zone journal* 7, 782–797.
- Šimunek, J., Wendroth, O., van Genuchten, M.T., 1998. Parameter Estimation analysis and of the Evaporation Method for Determination Soil Hydraulic Properties. *Soil Science* 62, 894–905.

- Warith, M.A., Takata, G.J., 2004. Effect of aeration on fresh and aged municipal solid waste in a simulated landfill bioreactor. *Water Quality Research Journal of Canada* 39, 223–229.
- Watson, D., 2013. Municipal waste management in the united kingdom. European Environmental Agency .
- Wildenschild, D., Jensen, K.H., 1999. Numerical modeling of observed effective flow behaviour in unsaturated heterogeneous sands. *Water Resources Research* 35, 29–42.
- Wilson, D.C., Rodic, L., Modak, P., Soos, R., Carpintero Rogero, A., Velis, C., Iyer, M., Simonett, O., 2015a. Global Waste Management Outlook. Technical Report. United Nations Environment Programme. URL: <http://www.unep.org/ietc/OurWork/WasteManagement/GWM0>. iSBN: 978-92-807-3479-9.
- Wilson, D.C., Rodic, L.L., Modak, P., Soos, R., A, C.R., Velis, C., Iyer, M., Simonett, O., 2015b. Global Waste Management Outlook Summary for Decision-Makers. Technical Report. United Nations Environment Programme. URL: <http://www.unep.org/ietc/Portals/136/Publications/Waste%20Management/GWM0%20report/GWM0%20Summary.pdf>.
- Woelders, J.A., Hermkes, H., Oonk, H., Luning, L., 2007. Dutch sustainable landfill research program, five years experience with the bioreactor test cell, in: Cossu, R., van der Sloot, H.A. (Eds.), *Sustainable Landfill*.
- Yenigula, N.B., Elfekia, A.M.M., Gehrelsa, J.C., Akkera, C., Hensbergen, A.T., Dekking, F.M., 2004. Reliability assessment of groundwater monitoring networks at landfill sites. *Journal of Hydrology* , 1–17doi:10.1016/j.jhydro1.2004.10.017.
- Younes, A., Ackerer, 2005. Solving the advection - diffusion equation with the Eulerian-Lagrangian localized adjoint method on unsaturated meshes and non uniform time stestep. *Journal of Computational Physics* 208, 384–402.
- Young, D.L., Wang, Y.F., Eldho, T.I., 2000. Solution of the advection-diffusion equation using rge Eulerian-Lagrangian boundary element method. *Engineering Analysis with Boundary Elements* 24, 449–457.
- Zacharof, A.I., Butler, A.P., 2004a. Stochastic modelling of landfill leachate and biogas production incorporating waste heterogeneity. model formulation and uncertainty analysis. *Waste Management* 24, 453–462. doi:10.1016/j.wasman.2003.09.010.
- Zacharof, A.I., Butler, A.P., 2004b. Stochastic modelling of landfill processes incorporating waste heterogeneity and data uncertainty. *Waste Management* 24, 241–250. doi:10.1016/j.wasman.2003.12.001.
- Zadeh, K.S., 2011. A mass-conservative switching algorithm for modeling fluid flow in variably saturated porous media. *Journal of computational physics* 3, 664–679.

- Zhang, D., Kang, Q., 2004. Pore scale simulation of solute transport in fractured porous media. *Geophysical American Letters*, American Geophysical Union 31.
- Zhang, Q.F., Lan, S.Q., Wang, Y.M., Xu, Y.F., 2008. A new numerical method for groundwater and solute transport using velocity field. *Journal of Hydrodynamics* 20, 356–364.
- Zhu, M., Lu, F., Hao, L.P., He, P.J., Shao, L.M., 2009. Regulating the hydrolysis of organic wastes by micro- and effluent recirculation. *Waste Management* 29, 2042–2050. doi:10.1016/j.wasman.2008.12.023.
- Ziyang, L., Bin, D., Xiaoli, C., Yu, S., Youcai, Z., Nanwen, Z., 2009. Characterization of refuse landfill leachates at three different stages in landfill stabilization process. *Journal of Environmental Sciences* 21, 1309–1314.
- van Zomeren, A., Meeussen, J.C.L., Oonk, H., Luning, L., van der Sloot, H.A., 2006. Database; Evaluation of Geochemical and Biochemical Processes and Release from Landfills. Technical Report. Dutch Sustainable Landfill Foundation.
- van Zomeren, A., van der Weij-Zuiver, E., van der Sloot, H.A., van den Berg, P., Bleijerveld, R., 2007. Environmental Behaviour of a Stabilised Waste Disposal in the Framework of Sustainable Landfilling, in: Cossu, R., van der Sloot, H.A. (Eds.), *Sustainable Land Filling*.
- Zyvoloski, G.A., A., R.B., S., V.H., Robinson, B.A., Viswanathan, H.S., A., R.B., S., V.H., 2008. Generalized dual porosity: A numerical method for representing spatially variable sub-grid scale processes. *Advances in Water Resources* 31, 535–544.

Summary

Because of the relatively low direct cost, landfilling is still preferred as the main option for disposal of municipal solid waste (MSW) (Hoornweg and Bhada-Tata 2012; Wilson et al. 2015a). The consequence is that current and future generations are facing a growing legacy of old landfills. The waste bodies in these landfills contain large amounts of biodegradable organic matter and other polluting compounds. Emissions of such compounds lead to serious threats to human health and the environment such as green house gas emissions and ground water pollution (Tachobanoglous and Kreith 2002; Bakis and Tuncan 2010). In order to prevent such threats, modern landfills in developed countries are engineered systems with geotechnical measures. Such engineered systems require eternal after-care and consequently landfilling is unsustainable and if after-care fails long term protection of the environment cannot be guaranteed.

Landfill operators and regulators in the Netherlands have taken the initiative to start-up three full-scale pilot projects where the aim is to reduce the emission potential of waste bodies in a relatively short period (Kattenberg and Heimovaara 2011).

Stabilization of waste bodies of landfill is achieved by treating the waste body using irrigation, recycling of leachate (Reinhart 1996; Sanphoti et al. 2006; Jiang et al. 2008; Zhu et al. 2009) combined with landfill gas extraction and/or aeration (Agdag and Sponza (2004); Ritzkowski et al. (2007)). These methods stimulate the biodegradation of organic matter present in the waste body. Under anaerobic conditions (stimulated by leachate recirculation) this leads to enhanced production of landfill gas which is captured and utilized. If anaerobic degradation is relatively slow, aeration leads to enhanced aerobic degradation. As the presence of organic matter in the waste body is an important driver of emissions via the gas phase and leachate, removing organic matter in a relatively short period reduces the emissions in the long term (Pohland and Alyousfi 1994; van Zomeren et al. 2007; Bun et al. 2013). In order for the regulators and landfill operators to agree on a required level of after care, a quantitative estimation of remaining long-term emission potential is required (Heimovaara et al. 2010; Kattenberg and Heimovaara 2011; Scharff 2014).

This thesis reports results of using numerical and lab experiments to obtain a deeper insight into the origin of preferential flow and the controlling factors of non-equilibrium transport in small scale unsaturated heterogeneous systems with similar properties as waste bodies. Our hypothesis is that, material heterogeneity in unsaturated systems is the origin of preferential flow and that infiltration patterns and rates are the controlling factors affecting non-equilibrium solute transport. For numerical analysis, a flow and transport simulator is required with accurate mass balances and which can handle steep concentration gradients without numerical dispersion or spurious oscillations. We developed a coupled flow and transport model using a finite difference method implemented as a MATLAB toolbox, which we named Variably Saturated Flow and Transport (VarSatFT). Flow is modelled using the mixed form of Richards' equation solved using the Picard iteration method (Celia et al. 1990a). The solute transport is approximated using an Eulerian-Lagrangian approach based on a modification of the Marker-in-Cell (MIC) method (Gerya 2010). The VarSatFT implementation was compared with two other implementations of the same flow and transport equations in COMSOL(tm) (COMSOL 4.3b) and FAESOR (Krysl 2010).

Using VarSatFT, we analysed water flow and solute transport in different unsaturated heterogeneous small scale systems. The origin of preferential flow and non-equilibrium solute transport lies in the funnelling of flow and advective transport through the high permeable zones. This leads to concentration gradients between the solutes in the mobile and immobile pore space due to the flushing of the mobile pore space with fresh (rain) water. The variation in infiltration rates and patterns are found to be the controlling factors for the magnitude non-equilibrium solute transport. The findings from the numerical analyses were verified in lab scale experiments. Infiltration and leachate recirculation can stimulate biodegradation if sufficient water is added to significantly increase water content. Our findings indicate the severe limitations associated with single continuum modelling methods of water flow and solute transport for full scale landfills, especially when leachate concentrations need to be predicted.

For the laboratory experiments we required data on the water retention parameters from well sorted sands near saturation. We developed an approach developed using the vertical distribution of water content along a TDR probe (Heimovaara et al. 2004). We performed these measurements in a multi-step drainage experiment at moments when flow had ceased so that hydrostatic conditions can be assumed. This gives a direct measurement of the water retention curve (van Genuchten 1980; Ledieu et al. 1986). Combining the water retention curve with the model for TDR waveforms and the pressure head distribution from the hydrostatic conditions allowed for the parameters in the unsaturated water retention curve to be optimized using the Bayesian inference scheme, using Differential Evolution Adaptive Metropolis (DREAM_{ZS}) algorithm (Laloy and Vrugt 2012). The ap-

proach we developed reduces the number of parameters compared with other TDR approaches which optimize water content at every node along TDR probe. This approach is suitable to quantify water retention parameters for samples with long heights and samples with uniform particle size distributions.

Samenvatting

Vanwege de relatief lage directe kosten is het storten van afval wereldwijd nog steeds de meest gebruikte methode voor het verwerken methode voor vast huishoudelijk afval (Hoornweg and Bhada-Tata (2012); Wilson et al. (2015a)). Het gevolg is dat de huidige en toekomstige generaties belast worden met een groeiende erfenis van oude stortplaatsen. Het afval in deze stortplaatsen bevat in veel gevallen een grote hoeveelheid biologisch afbreekbaar materiaal en andere vervuilende stoffen. Dit leidt tot emissie van broeikasgassen en vervuild percolaat wat een ernstige bedreiging is voor de gezondheid en het milieu (Tachobanoglous and Kreith 2002; Bakis and Tuncan 2010). Om deze emissies te voorkomen zijn moderne stortplaatsen voorzien van technische installaties waarin een groot aantal geotechnische maatregelen zijn geïmplementeerd. Deze installaties hebben echter oneindige nazorg nodig en het gevolg is dat er sprake is van een niet duurzame situatie omdat er geen garantie is voor lange termijn bescherming van het milieu als de technische locatie in de toekomst faalt.

Stortplaatsexploitanten en de Nederlandse overheid hebben de start van veld experimenten op praktijkschaal geïnitieerd op drie verschillende stortplaatsen. Het doel is om het emissie potentieel van het gestorte afval in deze stortplaatsen in een relatief korte periode om laag te brengen (Kattenberg and Heimovaara 2011).

Afval in deze stortplaatsen wordt gestabiliseerd door het toepassen van irrigatie van water en recirculatie van percolaat samen met stortgas extractie en/of beluchting (Agdag and Sponza 2004; Ritzkowski et al. 2007). Deze methoden stimuleren de biologische afbraak van het organisch materiaal in het afval. In een anaërobe omgeving (gestimuleerd door percolaat recirculatie) leidt dit tot toename van stortgas productie wat wordt afgevangen en nuttig gebruikt als groene brandstof. Als de anaërobe afbraak relatief langzaam verloopt, kan beluchting zorgen voor versnelde (aërobe) afbraak. Omdat het organisch materiaal in afval een belangrijke bron is van gas en percolaat emissies, zal het verwijderen van organisch materiaal in een relatief korte periode de lange termijn emissies verminderen (Pohland and Alyousfi 1994; van Zomeren et al. 2007; Bun et al. 2013). Voor overeenstemming tussen de overheid en de stortplaats exploitanten over de

benodigde nazorg is er een quantitative schatting van het resterende lange termijn emissie potentieel nodig (Heimovaara et al. 2010; Kattenberg and Heimovaara 2011; Scharff 2014).

De resultaten beschreven in dit proefschrift komen van numerieke en laboratorium experimenten die we hebben uitgevoerd om een dieper inzicht te krijgen in het ontstaan van preferentiële stroming en de factoren die dynamisch massa transport controleren in kleinschalige onverzadigde heterogene systemen met eigenschappen die vergelijkbaar zijn met afval. Onze hypothese is dat de aanwezigheid van heterogeniteit in het materiaal in onverzadigde systemen de bron is van preferentiële stroming en dat infiltratie patronen en snelheden de controlerende factoren zijn die de mate van preferentiële stroming en als gevolg de mate van dynamisch massa transport bepalen. Om de numerieke experimenten te kunnen uitvoeren is een stromings and transport computer model nodig met een nauwkeurige massa balans en die scherpe concentratie gradienten kan doorrekenen zonder numerieke dispersie of niet fysisch verklaarbare oscillaties. Hiervoor hebben we een model ontwikkeld dat de gekoppelde stromings en transport probleem oplost. Dit model is geïmplementeerd als een eindige-differentie toolbox in MATLAB, genaamd Variably Saturated Flow and Transport (VarSatFT). Stroming wordt gemodelleerd op basis van de gemengde vorm van de Richards' equation met behulp van de Picard iteratie methode (Celia et al. 1990a). Stoftransport is benaderd met een Eulerian-Lagrangian methode gebaseerd op een aanpassing van de Marker-in-Cell (MIC) methode (Gerya 2010). VarSatFT is getest door de resultaten van een aantal scenarios te vergeleken met de resultaten verkregen met twee andere implementaties van dezelfde stromings and transport vergelijkingen in COMSOL(tm) (COMSOL 4.3b) en FAESOR (Krysl 2010).

Met VarSatFT hebben we water stroming en stoftransport geanalyseerd in verschillende onverzadigde heterogene systemen op kleine schaal. Preferentiële stroming en dynamisch stofoverdracht ontstaan doordat in een heterogeen system, verticale stroming in toenemende mate in de diepte wordt getrechterd naar een relatief klein volume. Deze preferentiële stroming met advectief stof transport vindt plaats in de zones met een hoge doorlatendheid. Het gevolg is dat er concentratie gradienten ontstaan tussen de stoffen aanwezig in het mobiele porie volume en het stagnante porie volume doordat de mobiele porie volume wordt doorspoeld met schoon (regen) water. Variatie in infiltratie patronen en snelheden blijken controlerende factoren te zijn voor de orde van grootte van dynamisch massa transport. Resultaten uit de numerieke analyses zijn geverifieerd met laboratorium experimenten. Infiltratie en percolaat recirculatie kunnen biologische afbraak stimuleren wanneer door middel van het toegevoegde water de waterverzadiging in voldoende mate wordt verhoogd. Onze bevindingen geven de ernstige limitaties van het gebruiken van simulatie methodes gebaseerd op de Richards' vergelijking op basis van relatief grote representatieve elementaire volumes. Het adequaat verklaren van de geme-

ten dynamiek in het percolaat hoeveelheden en de percolaat concentraties vereisen model benaderingen met preferentiële stroming en dynamisch stof transport.

Voor de laboratorium experimenten was informatie nodig van de waterretentie parameters van bijna volledig verzadigd goed gesorteerd zand. Omdat deze metingen zeer moeilijk bleken te zijn, hebben we een methode ontwikkeld die gebruikt maakt van watergehalte metingen langs een TDR electrode (Heimovaara et al. 2004). Deze metingen werden uitgevoerd in een ontwateringsexperiment doe om stappen is uitgevoerd. Tijdens de momenten van hydrostatisch evenwicht geeft een meting van de watergehalte langs een TDR probe een directe meting van de waterretentie curve (van Genuchten 1980; Ledieu et al. 1986). Door van de waterretentie curve te integreren in het voorwaartse model om TDR golfvormen uit te rekenen, kan met de drukhoogte metingen afgeleid uit de hydrostatische condities de parameters in de onverzadigde waterretentie vergelijking worden geoptimaliseerd via een Bayesian inferentiemethode. Hiertoe hebben we gebruik gemaakt van het DiffereNTial Evolution Adaptive Metropolis (DREAM_{ZS}) algoritme (Laloy and Vrugt 2012). De methode die wij ontwikkeld hebben, verminderd het aantal parameters vergeleken met andere TDR methodes die de verzadiging optimaliseren voor elk knooppunt langs the TDR elektrode. Onze aanpak is geschikt voor het quantificeren van de waterretentie parameters voor monsters met grote hoogte en monsters met uniforme deeltjes distributie.

Acknowledgements

There are many people who have helped me throughout my years as a PhD-student. Firstly, I am very grateful to Prof. Timo Heimovaara, for providing me an opportunity to do research work in his supervision. Timo, your sharp criticism, enthusiastic discussions and generous guidance has helped me a lot in my research.

I am thankful for Prof. Chandan Mahanta my MTech supervisor at Indian Institute of Technology Guwahati, India for introducing me to several PhD programs, out of which I got selected to Eur-India, Lot-13 Scholarship program by Eurasmus Mundus, at Delft University of Technology. I am very thankful for Prof. Hans Bruining for selecting me for this PhD program. Hans I would like to thank you for teaching me COMSOL during my early days of PhD.

TU Delft is an ideal place for research because of its facilities and mainly because of its people. For this reason, I would like to thank all those who have helped me or inspired me during my stay over here. I would like to mention most of the names here. I would like to thank to Han de Visser and Kees van Beek for providing me their generous help for building the laboratorial set used to perform experiments which are presented in this thesis. I am very thankful to Arno Mulder for his help during our several visits to Landgraaf Landfill. I would like to thank to Guus Lohlefink, for helping me with my problems related to Geo-Engine cluster. I am thankful to Theda Olsder, Lianne Coelet and Marlijn Ammerlaan for their help and different arrangements they made for my stay in TU Delft. I am thankful to Leon van Paassen for giving me an opportunity to work on a project for Oldendorff carriers in Goa, India. This work provided me financial assistance during my PhD research.

I would like to thank Patrick Arnold and Jon Nuttall, for occasional after work parties and making my initial days in Delft more comfortable and I will always remember our trip during ROPARUN. I would like to thank Jiao Yuan for inviting me several times for soccer games. I would like to thank Andre van Turnhout for many fruitful discussions related to numerical modelling, music and global politics. I am thankful to my colleagues for having different entertaining and interesting discussions during coffee breaks, lunch and dinner

outings. These are in no particular sequence Andriy Bun, Laura Konstantaki, Michael Afanasyev, Luke Bergwerff, Vinh Pham, Amin Askarinejad, Cristina Jommi, Phil Vardon and Roderick Tollenaar and off course others whom I have forgotten to mention from our Geo-Engineering section.

I wish to thank my dear friends Tungky Subroto and Poly Bourghain, your encouraging nature made my PhD ending days much easier. I would also like to thank my dear friends Rajbeer Basera and Ajay Bhatt, you guys have always understood my doubts and worries. I would like to thank my dear friend Sagar Manchanda, your encouraging nature has always helped me. For different get together, dinner outings and parties, I will always remember time spent with my dear friends Caroline Bruens, Amarjeet Jaiswal, Divya Varkey, Gargi Kaushik, Rahul Thorat, Jeroen Heldens, Anna Trull, Jules Heldens, Helene Clogenson, Andrea Simonetto and Gabriele Garis.

I would like to thank my uncle Kishor Surwade, my aunt Ratana Sawardekar and my grandmother Shanta Surwade for their kind love. I would like to thank my sister Priyanka Baviskar for her love and support in everything. Finally, I would like to thank my parents Pratibha Baviskar and Madhukar Baviskar, for their love, endless support, encouragement, and always showing me positive in everything.

Shirishkumar M Baviskar

Curriculum Vitae

Shirishkumar M Baviskar was born on September 26, 1985, in Nasik, in Maharashtra state, India. In 2003, he started studying in Government College of Engineering Karad, Shivaji University, Maharashtra and obtained his bachelor of engineering degree in Civil Engineering in 2007. After that he worked as a lecturer in K.K. Wagh Polytechnic, Nasik for a year, simultaneously preparing for competitive exams organized by Indian Institutes of Technologies for their master programs. In 2008, based on all India, Graduate Aptitude Test Index score, he got selected for master program in Indian Institute of Technology Guwahati, India, situated in Assam state. In 2010 he obtained his master of technology degree in Environmental Engineering. In February 2010 he got a scholarship from Erasmus Mundus, Eur-India Program for his PhD research at Delft University of Technology. In August 2010 he started working as PhD-student in Geo-engineering section in supervision of Prof. Dr. Ir. Timo Heimovaara. The results of his work on "The origin of preferential flow and non-equilibrium transport in unsaturated heterogeneous porous systems" are described in this PhD thesis.

List of Publications

Journal Publications

1. Baviskar, S.M., Heimovaara, T.J., Numerical modelling of unsaturated flow and solute transport in waste bodies with steep concentration gradients. Chapter 2 from this thesis (ready to submit).
2. Baviskar, S.M., Heimovaara, T.J., Origin of preferential flow and its controlling factors on emission potential using numerical simulations and lab experiments in small scale systems. Chapter 3 and 4 from this thesis (ready to submit).
3. Baviskar, S.M., Heimovaara, T.J., Quantification of water retention parameters using spatial interpolations of TDR by unsaturated parametric relations at hydrostatic conditions. Chapter 5 from this thesis (ready to submit).

Conference Publications

1. Baviskar, S.M., Heimovaara, T.J., Suitability of different conceptual models for assessing the hydrology of a full scale pilot landfill. Fourth. International Workshop. Hydro-Physico-Mechanics of landfills. Santander, Spain, (27-28 April 2011).
2. Bun, A., Heimovaara, T.J., Baviskar, S.M., Turnhout, A.G., Konstantaki, L.A., Integrated modeling and up-scaling of landfill processes and heterogeneity using stochastic approach. Proceedings of the 7th Intercontinental Landfill Research Symposium (ICLRS), Sunderbyn, Sweden, (25-27 June 2012).
3. Heimovaara, T.J. Bun, A. van Turnhout, A.G. Konstantaki, L.A. Baviskar, S.M., Is it possible to quantify emission potential from high resolution monitoring of

- leachate dynamics?. Proceedings of the 7th Intercontinental Landfill Research Symposium (ICLRS), Sunderbyn, Sweden, (25-27 June 2012).
4. Bun, A., Heimovaara, T.J., Baviskar, S.M., Inverse modeling of landfill processes : estimating emission potential. Proceedings Sardinia, Italy, (30 September - 4 October 2013).
 5. Baviskar, S.M., Heimovaara, T.J., Addressing preferential flow in landfills by finite difference method and marker-in-cell method. Heat Transfer and Fluid Flow. Prague, Czech-Republic, (11-12 August 2014). Proceedings published ISBN 978-1-927877-09-8.
 6. Baviskar, S.M., Heimovaara, T.J., Comparing different numerical methods for two dimensional coupled water and solute transport in porous media. NM2PorousMedia. Dubrovnik, Croatia, (29-3 October 2014).
 7. Baviskar, S.M., Heimovaara, T.J., Origin of preferential flow and its controlling factors on emission potential using numerical simulations and lab experiments. Sixth. International Workshop. Hydro-Physico-Mechanics of landfills. Delft, Netherlands, (15-17 April 2015).